FASJS

Faculty of Arts and Science Journal of Science

SÜLEYMAN DEMİREL ÜNİVERSİTESİ

SÜLEYMAN DEMİREL
ÜNİVERSİTY

Süleyman Demirel University

Faculty of Arts and Sciences

Journal of Science

Volume

19

Issue

1

Year

2024

e-ISSN

1306-7575

Süleyman Demirel Üniversitesi Fen Edebiyat Fakültesi Fen Dergisi
https://dergipark.org.tr/sdufeffd
Süleyman Demirel University Faculty of Arts and Sciences Journal of Science e-ISSN: 1306-7575
Volume: 19, Issue: 1, Year: 2024

Journal Boards

Süleyman Demirel University Faculty of Arts and Sciences Journal of Science e-ISSN: 1306-7575

Volume: 19, Issue: 1, Year: 2024

Süleyman Demirel University Faculty of Arts and Science Journal of Science is a peer-reviewed scientific journal published semi-annually, in May and November.

Original scientific research articles submitted in English in the fields of Biology, Physics, Chemistry and Mathematics are continued in the scientific review process after the preliminary evaluation stage, where similarity and layout checks are made.

No fee is charged from the author or institution under any name.

Special numbers/issues can be published without changing the periodic publication frequency during the year.

Since 2017; technical notes, letters to the editor, discussions, case reports and reviews will not be accepted.

As of 01.01.2023, Süleyman Demirel University Faculty of Arts and Sciences Journal of Science only accepts studies submitted in English.

Süleyman Demirel University Faculty of Arts and Science Journal of Science (SDUFASJS) takes into account the principles published by the Higher Education Institutions Scientific Research and Publication Ethics Directive and "Committee on Publication Ethics" (COPE). In this context, the issues that are important for the authors, referees and editors are specified in the "Ethical Principles and Publication Policy" page of the journal website.

Süleyman Demirel University Faculty of Arts and Science Journal of Science is indexed in the following databases.

- ULAKBIM TR – Dizin
- Bielefeld Academic Search Engine (BASE)
- Centre for Agriculture and Bioscience International (CABI) - CAB Direct
- China National Knowledge Infrastructure (CNKI)
- Crossref
- Directory of Open Access Journals (DOAJ)
- Directory of Open Access Scholarly Resources (ROAD)
- EBSCO host
- Elektronische Zeitschriftenbibliothek (EZB)
- German Union Catalogue of Serials (ZDB)
- Google Academic
- Index Copernicus
- Information Matrix for the Analysis of Journals (MIAR)
- MathSciNet
- ResearchBib
- WorldCat

Süleyman Demirel Üniversitesi Fen Edebiyat Fakültesi Fen Dergisi

https://dergipark.org.tr/sdufeffd

Süleyman Demirel University Faculty of Arts and Sciences Journal of Science e-ISSN: 1306-7575

Volume: 19, Issue: 1, Year: 2024

CONTENTS

Süleyman Demirel Üniversitesi Fen Edebiyat Fakültesi Fen Dergisi https://dergipark.org.tr/sdufeffd
Süleyman Demirel University Faculty of Arts and Sciences Journal of Science e-ISSN: 1306-7575
Research Article, 2024, 19(1): 1-7, DOI: 10.29233/sdufeffd.1396580

L^{∞} Spaces of Vector-Valued Functions as Spaces of Continuous Functions

Banu Güntürk[1]

[1]Department of Mechanical Engineering, Faculty of Engineering, Baskent University, 06790, Ankara, TÜRKİYE
https://orcid.org/0000-0002-7728-7228

(Received: 27.11.2023, Accepted: 16.12.2023, Published: 27.05.2024)

Abstract: It is proved that for any decomposable perfect measure space $(Z, \mathcal{A}, \mu)$, the space $L^{\infty}_{\omega^*}(\mu, E^*)$ of essentially bounded weak* measurable functions on Z to E^* is linearly isometric to the space $C(Z, E^*_*)$ of continuous functions on Z to E^*_*, the latter space is being provided with the supremum norm $\|g\|_{\infty} = \sup_{z \in Z} \|g(z)\|$, where E^*_* stands for the space E^* endowed with its weak* topology.

Key words: L^{∞} Space, Vector-Valued Functions, Perfect Measure, Hyperstonean Space, Continuous Function Spaces

1. Introduction

If μ is a perfect measure on an extremally disconnected compact Hausdorff space X then the Banach space $L^{\infty}(\mu)$ of essentially bounded scalar measurable functions is linearly isometric to $C(X)$, the space of scalar continuous functions on X provided with the usual supremum norm [1] or [20]. For an arbitrary μ, we may employ the Gelfand-Naimark theorem to achieve the same result, that is, $L^{\infty}(\mu)$ is isometric to $C(Y)$ where Y denotes the maximal ideal space of $L^{\infty}(\mu)$, [3], [17] or [12]. In this article, we shall generalize this theorem to L^{∞}spaces of vector-valued functions. We shall restrict our study to perfect measures, and the range space will be a Banach dual E^* for continuous functions, where E^*_* stands for the dual space E^* provided with its weak* topology.

2. Material and Method

First, let us recall some (not entirely standard) terminology for integration of vector-valued functions. We will call two measure spaces $(X, \mathcal{A}, \mu)$ and $(Y, \mathcal{B}, \mu)$ *equivalent* if each number $1 \leq p < \infty$ and each Banach space E, the Bochner spaces $L^p(\mu, E)$ and $L^p(\nu, E)$ are linearly isometric. For basic information about these spaces, see references [8,9]. As pointed out in [6] equivalent measure spaces may have different L^{∞} spaces.

Following [1] we will call a measure space $(X, \mathcal{A}, \mu)$ *perfect* if X is an extremally disconnected locally compact Hausdorff space, $\mathcal{A}$ contains the Borel algebra and μ is a positive measure on $\mathcal{A}$ such that every nonempty open set contains a clopen set K, where $\mu(K) > 0$, and for every closed set C with empty interior, $\mu(C) = 0$.

In [6], Cengiz proves that an arbitrary measure space (X, Σ, μ) is equivalent to a perfect measure space $(\Omega, \mathcal{A}, \mu)$ with the following additional properties:

i. $\Omega = \sum_{i \in I} \bigoplus \Omega_i$, where $\{\Omega_i : i \in I\}$ of mutually disjoint extremally disconnected compact Hausdorff spaces Ω_i, $i \in I$,
ii. if a subset S of Ω is measurable then $S \cap \Omega_i$ is measurable for each $i \in I$, and the converse is also true,

iii. the restriction of μ to each Ω_i is a regular Borel measure on Ω_i,
iv. for each $A \in \mathcal{A}$, $\mu(A) = \sum_{i\in I} \mu(A \cap \Omega_i)$,
v. every σ –finite measurable set is contained a.e. (almost everywhere) in the union of a countable subfamily of $\{\Omega_i : i \in I\}$, and
vi. every measurable set A is equivalent to a clopen set C, that is, $\mu(A \Delta C) = 0$.

Note that the measure space $(\Omega, \mathcal{A}, \mu)$ is decomposable [14, p. 317]. Since μ is perfect, for every open set U, $\mu(\overline{U}) = \mu(U)$, and from (iv) it follows that every locally null set is actually null. (Recall that a measurable set is locally null if its intersection with every set of finite measure is null.)

Let Z denote the Stone-Čech compactification of Ω. Then, obviously, Z is extremally disconnected, and since Ω is locally compact, it is open in Z, [11, p.245] or [15, p. 90]. Using these facts, it is easily shown that the extension of μ to the Borel algebra $\mathcal{B}$ of Z, which we will continue to denote by μ, by defining the measure of any B in $\mathcal{B}$ to be the measure of $B \cap \Omega_i$ is indeed a perfect measure on Z. Since $Z \setminus \Omega$ is a null set, we will use Z and Ω interchangeably as the ground set. Hence, every measure is equivalent to a decomposable perfect measure on an extremally disconnected (locally) compact Hausdorff space.

Following [10] we call an exteremally disconnected compact Hausdorff space T *hyperstonean* if the union of the supports of the positive *normal* measures is dense in T, which is equivalent to having a perfect measure on T [1]. (We recall that a regular Borel measure ν on T is normal if $\nu(B) = 0$ for every Borel set of first category.) This condition ensures that $C(T)$ is a dual space [16]. Thus, each measure space is equivalent to a *hyperstonean measure space.*

L^∞ Spaces. Let (X, Σ, μ) be any measure space and E be a Banach space. Let us recall that a function $f: X \to E$ is *strongly measurable (or simply measurable)* if it is the almost everywhere limit in the norm topology of a sequence of measurable simple functions, and *locally measurable* if its restriction to each measurable set of finite measure is measurable. A locally measurable function $f: X \to E$ is *essentially bounded* if for some $\alpha > 0$, the set $\{x \in X : \|f(x)\| > \alpha\}$ is locally null, and the infimum of such numbers α is the essential supremum norm $\|f\|_\infty$ of f. $L^\infty(\nu, E)$ will stand for the Banach space of all essentially bounded locally measurable functions on X to E.

A function $g: X \to E^*$ is *weak* measurable* if for each $e \in E$, the composite function $\hat{e} \circ g$ is measurable, where $\hat{e}$ denotes the image of e in the second dual under the canonical embedding.

Throughout the rest of this paper we will be discussing the L^∞ space of E^*-valued functions rather than E-valued ones and $(\Omega, \mathcal{A}, \mu)$ will denote a fixed perfect measure space with additional properties (i) - (iv) mentioned earlier and Z will stand for the Stone-Čech compactification of Ω. The unique extension of μ to a perfect measure on the Borel algebra $\mathcal{B}$ of Z will still be denoted by μ.

For each $g \in L^\infty(\mu, E^*)$, the mapping ψ_g, defined on $L^1(\mu)$ by

$$\psi_g(f) = \int_\Omega \langle f, g \rangle d\mu$$

for all $f \in L^1(\mu)$, is a bounded linear functional with norm $\|\psi_g\| = \|g\|_\infty$, where $\langle f, g\rangle(\omega) = \langle f(\omega), g(\omega)\rangle = g(\omega)\big(f(\omega)\big)$, $\omega \in \Omega$. This is a well-known result for σ-finite measures [8, p.98], and has been generalized recently to perfect measures [7]. And the isometry $\psi: g \to \psi_g$ from $L^\infty(\mu, E^*)$ into $L^1(\mu, E)^*$ is surjective if and only if E^* has the Radon-Nikodým property (RNP) with respect to μ. It means that, each μ-continuous E^*-valued measure of bounded variation on $\mathcal{A}$ to E^* can be represented (via integral) by an E^*-valued integrable function. (This was first proved by Banach and Taylor [2] for Lebesgue measure on the unit interval $[0,1]$ and generalized to σ-finite measures by Gretsky and Uhl [13], and its generalization to arbitrary perfect measures is due to Cengiz [7]. A nice proof for the σ-finite case can be found in [8].) In particular, for each reflexive Banach space E we have $L^\infty(\mu, E) \backsimeq L^1(\mu, E)^*$, for such spaces are dual spaces and have the RNP with respect to finite measures [8], and this property can be generalized to perfect measures as the following proposition shows. (If the measure space is not perfect this result may not hold even in the scalar case, [14] or [19].)

3. Results

Proposition 3.1 If a Banach space E has the RNP with respect to any finite measure then it has this property with respect to any perfect measure. Consequently, reflexive spaces have the RNP with respect to perfect measures.

Proof. We will prove this proposition for our fixed perfect measure μ. Let $\lambda : \mathcal{A} \to E$ be a μ-continuous measure has bounded variation. Then for each $i \in I$, there is a μ-integrable function $g_i : \Omega_i \to E$ which vanishes outside Ω_i satisfies the integration

$$\lambda(A) = \int_A g_i d\mu, \qquad \text{for all } A \in \mathcal{A}_i,$$

where $\mathcal{A}_i = \{A \cap \Omega_i : A \in \mathcal{A}\}$. Now let $g = \sum_i g_i$. Then clearly g is locally measurable. We claim that it is actually measurable.

Since λ has bounded variation, $|\lambda|(\Omega) < \infty$. Then we have $|\lambda|(\Omega_i) = 0$ for all but countably many $i \in I$, where $|\lambda|$ states for the total variation of λ. Thus, there exist a countable subset J of I such that the set $N_i = \{x \in \Omega_i : g(x) \neq 0\}$ is null for each $i \in I \setminus J$, and since $\bigcup_{i \in I \setminus J} N_i$ is locally null, it is actually null. Thus, it follows that g is measurable as claimed.

Since

$$|\lambda|(\Omega) = \int_\Omega \|g(.)\| d\mu$$

we conclude that g is integrable, and since the support of g is contained a.e. in $\bigcup_{j \in J} \Omega_j$, more simply we may thus suppose that $I = \{1,2, \dots\}$. Now, we have

$$\lambda(A) = \int_A g d\mu \,,$$

for all $A \in \mathcal{A}$, proving our proposition.

The following proposition will be needed later.

Proposition 3.2 Every E^*-valued measurable function is weak* measurable.

Proof. Let $g : \Omega \to E^*$ be measurable. Then by the Pettis measurability theorem, [19] or [8], for each $i \in I$, the restriction g_i of g to Ω_i is weak* measurable. Thus for each $x \in E, \hat{x} \circ g_i$ is measurable, and therefore $\hat{x} \circ g$ is locally measurable, and hence (by Property (ii) of μ), it is measurable. This completes the proof.

Proposition 3.3 If $f : \Omega \to E$ is measurable and $g : \Omega \to E^*$ is weak* measurable then the scalar function $\langle f, g \rangle$ is measurable.

Proof. Let $g : \Omega \to E^*$ be a weak* measurable function, and let $s = x_1\chi_{A_1} + \cdots + x_n\chi_{A_n}$ be a measurable simple function from Ω to E, where for a set S, χ_S denotes the characteristic function of S. Then, since for each $k = 1,2, \ldots, n$, $\hat{x}_k \circ g$ and χ_{A_k} are measurable,

$$\langle s, g \rangle = \sum_{k=1}^{n} (\hat{x}_k \circ g)\, \chi_{A_k}$$

is measurable. Now let $f : \Omega \to E$ be a measurable function and $s_n : \Omega \to E$ be a sequence of measurable simple functions converging a.e. to f in the norm topology on E. Then,

$$\lim_n \langle s_n(\omega), g(\omega) \rangle = \langle f(\omega), g(\omega) \rangle \text{ a.e. on } \Omega,$$

which proves that $\langle f, g \rangle$ is measurable, is claimed.

$C(Z, E_*^*)$ will denote the space of all continuous functions f on Z to E_*^* provided with the supremum norm $\|f\|_\infty = \sup_{z \in Z} \|f(z)\|$.

Corollary 3.4 The elements of $C(Z, E_*^*)$ are weak* measurable.

It is tempting to call $g : \Omega \to E^*$ weak* measurable if $g^{-1}(B)$ is measurable for every weak* Borel subset B of E^*. The following proposition shows that this is true.

Proposition 3.5 Let $g : \Omega \to E^*$ be a function such that $g^{-1}(B)$ is measurable for each weak* measurable subset B of E^*. Then g is weak* measurable.

Proof. For each $x \in E$, the functional $\hat{x}$ is weak* continuous and so, it is measurable with respect to the weak* Borel algebra on E_*^*. Thus, for each Borel set S in the field of complex numbers $(\hat{x} \circ g)^{-1}(S) = (g)^{-1}(\hat{x}^{-1}(S))$ is measurable. Hence g is weak* measurable.

Theorem 3.6 For our perfect measure space, $L^\infty_{\omega^*}(\mu, E^*) \backsimeq C(Z, E_*^*) \backsimeq L^1(\mu, E)^*$.

Proof. Let $g \in C(Z, E_*^*)$. Then for each $f \in L^1(\mu, E)$, the function $\langle f, g \rangle$ is measurable and since $|\langle f(.), g(.) \rangle| \leq \|f(.)\| \|g\|_\infty$, it is also integrable, and the mapping ψ_g defined on $L^1(\mu, E)$ by

$$\psi_g(f) = \int_\Omega \langle f, g\rangle d\mu\,, \qquad f \in L^1(\mu, E)$$

is a bounded functional with norm $\leq \|g\|_\infty$. Actually, since $(Z, \mathcal{B}, \mu)$ is a perfect measure space, by a theorem of Cambern and Greim [5] the mapping $g \to \psi_g$ is a linear isometry from $C(Z, E_*^*)$ onto $L^1(\mu, E)^*$. (The known proof of mentioned theorem depends on the observation that $C(Z, E_*^*)$ is isometric to the space $\mathcal{L}(E; C(Z))$ of bounded operators on E to $C(Z)$ which is proved explicitly in [4], therefore a more direct proof of the inequality $\|g\|_\infty \leq \|\psi_g\|$, will be welcome.) So, the space $L^\infty(\mu, E^*)$ is isometric to a subspace of $C(Z, E_*^*)$ and, this isometry is surjective if and only if E^* has the RNP with respect to μ.

A weak* measurable function $g : \Omega \to E^*$ may not be essentially bounded in the usual sense, or better, the definition of essential boundedness may not apply to g, for the function $\|g(.)\|$ need not be measurable, and therefore, the definition of essential boundedness for weak* measurable functions should be different. But, in view of Proposition 3.2, Corollary 3.4, and the fact that $\|g\|_\infty$ is the same as the norm of the operator ψ_g when g is either in $L^\infty(\mu, E)$ or $C(Z, E_*^*)$, what can be more natural than calling a weak* measurable function g essentially bounded if

$$\psi_g(f) = \int_\Omega \langle f, g\rangle d\mu$$

defines a bounded functional on $L^1(\mu, E)$, that is, for each $f \in L^1(\mu, E)$, $\langle f, g\rangle$ is integrable and there is a constant $k > 0$ such that

$$\left| \int_\Omega \langle f, g\rangle d\mu \right| \leq k\|f\|_1 \text{ for all } f \in L^1(\mu, E),$$

in which case, we define the essential supremum norm $\|g\|_\infty$ of g as the norm of the functional ψ_g on $L^1(\mu, E)$.

$L_{\omega^*}^\infty(\mu, E^*)$ will denote the normed space of all essentialy bounded weak* measurable functions on Ω to E^*, provided with the essential supremum norm.

For two normed spaces E and F, the notation $E \backsimeq F$ will indicate that they are linearly isometric.

We can identify $C(Z, E_*^*)$ with a subspace of $L_{\omega^*}^\infty(\mu, E^*)$ in the most natural way, and since the mapping $g \to \psi_g$ maps $C(Z, E_*^*)$ onto, and $L_{\omega^*}^\infty(\mu, E^*)$ into $L^1(\mu, E)^*$ we conclude that $C(Z, E_*^*) \backsimeq L_{\omega^*}^\infty(\mu, E^*)$. Hence we have completed the proof of the theorem.

Corollary 3.7 $L^\infty(\mu, E)^* = L_{\omega^*}^\infty(\mu, E^*)$ if and only if E^* has the RNP.

Corollary 3.8 $L^\infty(\mu, E)$ isometric to a subspace of $C(Z, E_*^{**})$, where E_*^{**} denotes the second dual with its weak* topology.

Proof. We identify $L^{\infty}(\mu, E)$ with the subspace $L^{\infty}(\mu, \hat{E})$ of $L^{\infty}(\mu, E^{**}) \backsimeq C(Z, E_*^{**})$ where $\hat{E}$ denotes the image of E in E^{**} under the canonical embedding.

Corollary 3.9 Z is the maximal ideal space of $L^{\infty}(\mu)$.

Remark For a perfect measure space $(X, \mathcal{A}, \nu)$ with X compact, $L^{\infty}(\mu) \backsimeq C(X)$ was already known, [1] or [20].

4. Conclusion

In this paper, we prove an important isometry between the L^{∞} space of vector-valued functions and the space of continuous functions on Z to E_*^*, where Z is the Stone-Čech compactification of the hyperstonean space Ω. Hyperstonean spaces are very important spaces with several properties [21] and they are also huge indeed. So, this relation is very crucial between the functional analysis and measure theory. Hence, the results obtained will shed light on important studies to be conducted on this subject in the future.

Authorship contribution statement

B. Güntürk: Conceptualization, Methodology, Investigation, Software, Review and Editing.

Declaration of competing interest

As the author of this study, I declare that I do not have any conflict of interest statement.

Acknowledgment

I am grateful to my teacher, the late Prof. Bahaettin Cengiz, who made a valuable contribution to this article.

Ethics Committee Approval and/or Informed Consent Information

As the author of this study, I declare that I do not have any ethics committee approval and/or informed consent statement.

References

[1] E. Behrends, et al, L^p-structure in real Banach spaces, Lecture Notes in Mathematics, 613, Berlin-New-York, Springer-Verlag, 1977.

[2] S. Bochner and R.E. Taylor, "Linear functionals on certain spaces of abstractly-valued functions", *Annals of Mathematics*, 39(2), 913-944, 1938.

[3] F. Bonsall and J. Duncan, Complete Normed Algebras, Berlin-Heidelberg-New York, Springer-Verlag, 1973.

[4] M. Cambern and P. Greim, "The bidual of $C(X, E)$", *Proceedings of the American Mathematical Society*, 85, 53-58, 1982.

[5] M. Cambern and P. Greim, "The dual of a space of vector measures", *Mathematische Zeitschrift*, 180, 373-378, 1982.

[6] B. Cengiz, "On the duals of Lebesgue-Bochner L^p spaces", *Proceedings of the American Mathematical Society*, 114, 923-926, 1992.

[7] B. Cengiz, "The isometries of the Bochner space $L^p(\mu, H)$ ", *Turkish Journal of Mathematics*, 23(3), 1999.

[8] J. Diestel and J. J. Uhl Jr., Vector Measures, Mathematical Surveys and Monographs no.15, *American Mathematical Society*., Providence, Rhode Island, 1977.
[9] Dinculeanu N., Vector Measures, New-York, Pergamon Press, 1967.
[10] J. Dixmier, "Sur certains espaces considérés par M.H. Stone, *Summa Brasiliensis Math*ematicae, 2(11) , 151-182, 1951.
[11] J. Dugundji, Topology, Boston, Allyn and Bacon Inc., 1966.
[12] N. Dunford and J. T. Schwartz, Linear Operators, Part I, New York, Interscience, 1958.
[13] N. E. Gretsky and J. J. Uhl Jr., "Bounded linear operators on Banach function spaces of vector-valued functions", *Transactions American Mathematical Society*, 167, 263-277, 1972.
[14] E. Hewitt , K. Stromberg, Real and Abstract Analysis, New York, Springer-Verlag, 1965.
[15] L. Gilman and M. Jerison, Rings of Continuous Functions, Princeton-Toronto-London-Melbourne, D. Van Nostrand Company, 1960.
[16] H. E. Lacey, The Isometric Theory of Classical Banach Spaces, Berlin- Heidelberg-New York, Springer-Verlag, 1974.
[17] M. A. Naimark, Normed Algebras, The Netherlands, Wolters-Noordhoff Publishing, 1972.
[18] B. J. Pettis, "On integration in vector measures", *Transactions American Mathematical Society*, 44, 277-304, 1938.
[19] H. L. Royden, Real Analysis, 3rd ed., London-New York, Collier-Macmillan, 1988.
[20] H. H. Schaefer, Banach Lattices and Positive Operators, Berlin-Heidelberg-New York, Springer-Verlag, 1974.
[21] B. Güntürk, B. Cengiz, "On some properties of hyperstonean spaces", *Turkish Journal of Mathematics*, 5(42), 2288-2295, 2018.

Süleyman Demirel Üniversitesi Fen Edebiyat Fakültesi Fen Dergisi https://dergipark.org.tr/sdufeffd
Süleyman Demirel University Faculty of Arts and Sciences Journal of Science e-ISSN: 1306-7575
Research Article, 2024, 19(1): 8-17, DOI: 10.29233/sdufeffd.1407647

Moduli Space for Invariant Solutions of Seiberg-Witten Equations

Muhiddin Uğuz

Department of Mathematics, Faculty of Art and Science, Middle East Technical University, 06800, Ankara, TURKIYE
https://orcid.org/0000-0003-2344-503X

(Received: 20.12.2023, Accepted: 01.02.2024, Published: 27.05.2024)

Abstract: In this work we study the G-invariant solutions of the Seiberg-Witten equations when G is a cyclic group acting on a manifold M, preserving the metric and the orientation. G is assumed to have a lift to principle $Spin^c$ bundle which gives rise to Seiberg-Witten equations in question. In this work, we prove that when the dimension b_+^G of the G-fixed points of harmonic two forms is positive, for a generic choice of an element in this fixed point set, the moduli space of invariant solutions of Seiberg-Witten equations is a compact, smooth and oriented manifold of dimension $d^G = ind\ D_A^G - b_+^G - 1$.

Key words: Gauge Theory, Equivariant Seiberg-Witten theory, Equivariant Seiberg-Witten moduli space.

1. Introduction,

In 1949 Whitehead [1] classified simply connected, closed, oriented 4-manifolds up to orientation-preserving homotopy equivalence by their intersection form. A proof of this theorem is given in [4], page 103. Later on M. Freedman in 1982 gave a homeomorphism classification of closed, simply connected 4-manifolds [3]. His results were expressed in terms of intersection forms. However, the classical tools, like intersection forms, were not enough to detect differential structures. Differential topology of 4-manifolds is intensively studied by Simon Donaldson during the years of 1980's. Using moduli space of connections on an $SU(2)$ bundle, he introduced an invariant which detects differential structures. However, as the Yang-Mills equations are nonlinear, to make explicit computations was not easy and substantial analysis was necessary. Sometimes, instead of using this invariant, mere use of moduli space of Gauge equivalence classes of connections on a $SU(2)$ or $SO(3)$ bundle itself led to important results. One of these was a well-known theorem of Donaldson [2],[8], which states that the only negative definite, unimodular form, represented by a closed, smooth, simply connected four manifold, is the negative of the standard (diagonal) form.

In the year 1994, a set of equations, namely Seiberg-Witten equations, were introduced by Edward Witten, and with them, most of the main results of Donaldson Theory are obtained in a much shorted and simpler work.

These equations were associated to a $Spin^c(4)$ structure on the manifold in question and they were invariant under the group of bundle automorphisms of the determinant line bundle associated to this $Spin^c(4)$ structure. This group is called Gauge group. As in Donaldson theory gauge equivalence classes of solutions of Seiberg-Witten equations form a moduli space and give important information about the differential topology of

the manifold. In fact, a diffeomorphism invariant, called Seiberg-Witten invariant, was introduced using this moduli space (see [5], [7], [2]).

The moduli space of Gauge equivalence classes of the solutions of the perturbed Seiberg Witten equations is compact, and in some cases, for a generic perturbation, is a zero dimensional manifold and hence consists of finitely many points. In this case, Seiberg-Witten invariant is the algebraic sum of the points in the moduli space counted with the multiplicities according to the orientation.

In this work, we construct the moduli space of solutions of Seiberg-Witten equations that are invariant under certain cyclic group action. The manifold structure is stated and then proven. As a future work, we will concentrate on the special structure near singularities.

Let G be a cyclic group of order α. Suppose G acts to preserve orientation on a closed, oriented four dimensional manifold. Choose a G-invariant Riemannian metric and a characteristic G line bundle L. We denote the associated principal $U(1)$-bundle of L by P_L and the associated principal $SO(4)$-bundle of T^*M by $P_{\mathrm{SO}(4)}$. Let $P_{Spin^c(4)}$ be the associated principal $Spin^c(4)$-bundle whose determinant bundle is L. Assume G action on $P_{\mathrm{SO}(4)}$ x P_{L} lifts to a G action on $P_{Spin^c(4)}$. Let D_A denote the Dirac operator associated to this $Spin^c(4)$-structure. Since D_A is equivariant under the action of G, the map D^G which is the restriction to the G-fixed point set of the domain of Dirac operator D makes sense.

The main theorems of this work are following.

Main Theorem 1: If $\pi_1(M) = 0$, for every choice of G-invariant self dual form $\Phi \in \Omega_+^G$, the moduli space M_Φ^G is compact.

Main Theorem 2: If $b_+^G > 0$,then for a generic perturbation φ in Ω_+^G, the moduli space M_φ^G of Seiberg-Witten equations perturbed by φ is an oriented smooth manifold of dimension $d^G = ind\, D_A^G - b_+^G - 1$.

2. Material and Method

2.1. Bundle Theory

Definition 1: Let G be a Lie group. A principal G -bundle is a triple $P(M, G, \pi)$ where P is a smooth manifold on which G acts from the right freely, and around each point of the smooth manifold $M = P/G$ there exists a neighborhood U so that, for the projection $\pi: P \to P/G = M$, $P|_U = \pi^{-1}(U) \cong U \times G$ isomorphic as G-spaces. P is called the total space, M is called the base space and G is called the structure group.

Theorem 1: Isomorphism classes of principal G-bundles over M are in one-to-one correspondence with the elements of $H^1(M; G)$ and also with the elements of $[M, BG]$, that is, homotopy classes of the maps from M to the classifying space BG.

Definition 2: Let F be a smooth manifold on which G acts from left. Then given a principal G-bundle $P(M, G, \pi)$ over M, we define $P_F = (P \times F)/\sim$ where $(p, f) \sim (p \bullet g, g^{-1} \bullet f)$. The bundle $P_F \to M$ is called as a fiber bundle associated to P with fiber F.

Definition 3: As a special case of the fiber bundle, defined above, if we take F to be a vector space V and via a representation $\rho : G \to GL(V)$, define a left action of G by $(g, v) \to \rho(g)(v)$. Then the fiber bundle $(P \times V)/\sim$ we get is called a vector bundle modeled on V and denoted by $(P \times_\rho V)$.

Theorem 2: Again as a special case of fiber bundle, take $F = H$ another Lie group with a group homomorphism $\rho: G \to H$. Define a left action of G on H by : $g \bullet h = \rho(g)h$ Then $P_H = P \times_\rho H$ is a principal H-bundle over M.

Definition 4: Given two principal bundles $P_1(M_1, G_1, \pi_1)$, $P_2(M_2, G_2, \pi_2)$, and a Lie group homomorphism γ: $G_1 \to G_2$, a map φ: $P_1 \to P_2$ is called a bundle map if φ ($p \bullet g_1$)= φ (p) • γ(g_1). Note that φ induces a map on the base spaces φ˜: $M_1 \to M_2$, and we have φ(p_1) ∈ $\pi_2^{-1}(\varphi^{\sim}(\pi_1(p_1)))$ for all $p_1 \in P_1$.

Given γ: $G_1 \to G_2$ and a bundle map φ: $P_1 \to P_2$ consider the map $P_1 \times_\gamma G_2 \to P_2$ defined by $[p_1, g_2] \to \varphi(p_1) \bullet g_2$. Since $[p_1 \bullet h_1, \gamma(h_1)^{-1} g_2] \to \varphi(p_1 \bullet h_1) \bullet (\gamma(h_1)^{-1} \bullet g_2) = \varphi(p_1) \bullet \gamma(h_1) \bullet \gamma(h_1)^{-1} \bullet g_2 = \varphi(p_1) \bullet g_2$, the above bundle map is well defined and hence we have P_2 is isomorphic to $P_2 \times_\gamma G_2$.

Notation: Γ(E) denotes the space of smooth sections of the bundle: $p : E \to M$. That is, a smooth map ψ∈Γ(E) if ψ:M → E satisfies $\rho \circ \psi(x) = x$ for all $x \in M$. We usually write Γ(M) for Γ(TM).

2.2. Connection and Curvature

Definition 5: A connection on a vector bundle $p : E \to M$ is a map

$$\nabla : \Gamma(M) \times \Gamma(E) \to \Gamma(E)$$

$$(X, \sigma) \to \nabla_X \sigma = \nabla (X, \sigma)$$

which satisfies the following properties:

- $\nabla_X (f\sigma + \tau) = (Xf)(\sigma) + f \nabla_X \sigma + \nabla_X \tau$
- $\nabla_{fX+Y} (\sigma) = f \nabla_X (\sigma) + \nabla_Y (\sigma)$

where $(Xf)(p) = X(p)f$ is the directional derivative.

An equivalent way of defining a connection on a vector bundle $p : E \to M$ is using the isomorphism

$$\Gamma(T^*M \otimes E) \cong \Gamma(Hom(TM, E)) \cong Hom_{C^\infty_M}\big(\Gamma(TM), \Gamma(E)\big);$$

It is a map

$$d^E : \Gamma(E) \to \Gamma(T^*M \otimes E) \text{ such that}$$

$$d^E\left(f|_{U_\alpha}+\tau\right)=(df)\otimes\sigma+fd^E\sigma+d^E\tau.$$

Note that, after choosing a local trivialization $(U_\alpha, g_{\alpha\beta})$ such that over U_α the bundle is trivial, i.e. $E|_{U_\alpha}=U_\alpha\times R^m$, any connection restricted to U_α is of the form $d^E|_{U_\alpha}(\sigma_\alpha)$=d$\sigma_\alpha+w_\alpha\sigma_\alpha$ where σ_α is a section over U_α and w_α is a $m\times m$ matrix of one forms on M. That is

$$d^E\begin{pmatrix}\sigma_1\\ \sigma_2\\ \vdots\\ \sigma_m\end{pmatrix}=\begin{pmatrix}d\sigma_1\\ d\sigma_2\\ \vdots\\ d\sigma_m\end{pmatrix}+\begin{pmatrix}w_1^1 & w_2^1 & \cdots & w_m^1\\ w_1^2 & w_2^2 & \cdots & w_m^2\\ \vdots & \vdots & \ddots & \vdots\\ w_1^m & w_2^m & \cdots & w_m^m\end{pmatrix}\begin{pmatrix}\sigma_1\\ \sigma_2\\ \vdots\\ \sigma_m\end{pmatrix}$$

Notation: $\Omega^k(E)=\Gamma(\Lambda^k(T^*\mathrm{M})\otimes\mathrm{E})$

Above definition of connection d^E can be extended to a R-linear map

$$d^E\colon\Omega^k(E)\to\Omega^{k+1}(E)$$

by tensoring with deRham complex as in [6]. For, define

$$d^E(\sigma_1\wedge\sigma_2)=d\sigma_1\otimes\sigma_2+(-1)^k\sigma_1\wedge d^E\sigma_2$$

where $\sigma_1\in\Omega^k, \sigma_2\in\Omega^0(E)$.

Definition 6: Curvature of a connection $d^E\colon\Omega^0(E)\to\Omega^1(E)$ on E is defined to be the $C^\infty(M)$-linear tensor $d^E\circ d^E\colon\Omega^0(E)\to\Omega^2(E)$.

Again, over U_α we have $d^E\circ d^E(\sigma_\alpha)=(dw_\propto+w_\propto\wedge w_\propto)(\sigma_\alpha)=\Omega_\alpha\sigma_\alpha$ where Ω_α is a matrix of two forms.

One final remark about connection and its curvature is about how they transform from U_α to U_β. In order these locally defined connections and their curvature to be well defined globally, on $U_\alpha\cap U_\beta$ we must have:

$$w_\propto=g_{\alpha\beta}dg_{\alpha\beta}{}^{-1}+g_{\alpha\beta}w_{\alpha\beta}g_{\alpha\beta}{}^{-1}\text{and}$$
$$\Omega_\alpha=g_{\alpha\beta}\Omega_\beta g_{\alpha\beta}{}^{-1}$$

Theorem 3: (Hodge's Theorem): Every deRham cohomology class on a compact oriented Riemannian manifold M possesses a unique harmonic representative. Thus

$$H^p(M;R)\cong H^p(M)$$

Moreover, $H^p(M;R)$ is finite dimensional and $\Omega^p(M)$ possesses direct sum decompositions

$$\Omega^p(M) = H^p(M) \oplus d(\Omega^{p-1}(M)) \oplus \delta(\Omega^p(M)).$$

2.3. The Groups $SO(4)$, $Spin(4)$ and $Spin^c(4)$

Following [7], we shall consider the quaternions H as 2×2 complex matrices of the form $= \begin{pmatrix} t+iz & -x+iy \\ x+iy & t-iz \end{pmatrix} = \begin{pmatrix} w & -\bar{v} \\ w & \bar{w} \end{pmatrix}$. With this identification, we have

$$\tilde{1} = \begin{pmatrix} 1 & 0 \\ 0 & 1 \end{pmatrix};\ \tilde{\imath} = \begin{pmatrix} i & 0 \\ 0 & -i \end{pmatrix};\ \tilde{\jmath} = \begin{pmatrix} 0 & -1 \\ 1 & 0 \end{pmatrix};\ \tilde{k} = \begin{pmatrix} 0 & -i \\ -i & 0 \end{pmatrix},$$
$$Q = \begin{pmatrix} t+iz & -x+iy \\ x+iy & t-iz \end{pmatrix} = t\tilde{1} + z\tilde{\imath} + x\tilde{\jmath} - y\tilde{k}$$

and the matrix multiplication agrees with the quaternion multiplication.

Since $\det(Q) = t^2 + x^2 + y^2 + z^2 = \langle Q, Q \rangle$ −Euclidean dot product, regarding $(t, z, x, y) \in R^4$as $t + iz + jx - ky \in H$, we can identify the unit sphere in $R^4$with the special unitary group

$$SU(2) = \{Q \in H; \langle Q, Q \rangle = 1\} = \left\{Q = \begin{pmatrix} w & -\bar{v} \\ w & \bar{w} \end{pmatrix}; \det(Q) = 1\right\}.$$

Definition 7: $Spin(4) = SU_+(2) \times SU_-(2)$, where $SU_+(2)$ and $SU_-(2)$ are copies of $SU(2)$.

Definition 8: $SO(4) = (SU_+(2) \times SU_-(2))/Z_2$.

A typical element of $Spin(4)$ will be represented by (A_+, A_-). We have special orthogonal representation

$$\rho: Spin(4) \to SO(4) = \frac{SU_+(2) \times SU_-(2)}{Z_2},$$
$$\rho(A_+, A_-)(Q) = [A_+, A_-](Q) = A_- Q A_+^{-1}.$$

In fact ρ is surjective and since both $SO(4)$ and $Spin(4)$ are compact Lie groups, it induces an isomorphism in the level of Lie algebras and hence $Spin(4) \to SO(4)$ is a covering space (double cover).

Elements of $Spin(4)$ can also be represented by the 4×4 matrices $\begin{pmatrix} A_+ & 0 \\ 0 & A_- \end{pmatrix}$. This representation suggests that we can also consider $Spin(4)$ as a subgroup of $Spin^c(4)$where;

Definition 9: $Spin^c(4) = \left\{\begin{pmatrix} \lambda A_+ & 0 \\ 0 & \lambda A_- \end{pmatrix};\ \lambda \in \mathrm{U}(1) = S^1\right\}$, which also can be defined as $Spin^c(4) = (\ Spin(4) \times \mathrm{U}(1)\ ) / Z_2$ where Z_2acts diagonally.

We have representation

$$\rho^{\,c}: Spin^c(4) \to GL(H)$$

$$\rho\left(\begin{pmatrix}\lambda A_+ & 0\\ 0 & \lambda A_-\end{pmatrix}\right)(Q) = (\lambda A_-)Q(\lambda A_+)^{-1}.$$

We also have a group homomorphism:

$$\pi: Spin^c(4) \to U(1), \text{ given by}$$
$$\pi\begin{pmatrix}\lambda A_+ & 0\\ 0 & \lambda A_-\end{pmatrix}=\lambda^2.$$

2.4. $SO(4)$, $Spin(4)$ and $Spin^c(4)$ Structures on a Manifold M

Definition 10: $SO(4)$ structure is a collection $\{(U_\alpha, g_{\alpha\beta});\ \alpha,\beta \in \Lambda\}$ where U_α is an open cover of orientable 4 manifold M, $g_{\alpha\beta}: U_\alpha \cap U_\beta \to SO(4)$satisfying the cocycle condition $g_{\alpha\beta}g_{\beta\gamma} = g_{\alpha\gamma}$. An alternative way of defining S$O(4)$ structure is specifying a map $f_0: M \to BSO(4)$.

Definition 11: An associated $Spin(4)$ structure to $SO(4)$ structure is a collection $\{(U_\alpha, \bar{g}_{\alpha\beta})\}$; where $\bar{g}_{\alpha\beta}: U_\alpha \cap U_\beta \to Spin(4)$ satisfying cocycle condition and $\rho \circ \bar{g}_{\alpha\beta} = g_{\alpha\beta}$, where $\rho: Spin(4) \to SO(4)$. Alternatively, an associated $Spin(4)$ structure to $SO(4)$ structure is a lifting of $f_0: M \to BSO(4)$ to $\bar{f}_0: M \to BSpin(4)$.

From the obstruction theory, it is known that the only obstruction for the existence of this lifting, that is, for the existence of $Spin(4)$ structure, i.e. a bundle with structure group

$Spin(4)$, associated to the given $SO(4)$ structure on the tangent bundle $T(M)$, is $w_2(TM) \in H^2(M, Z_2)$.

Let $W_+$and W_- be two copies of C^2. Consider the representations $\rho_+$and ρ_- given by

$$\rho_\mp\begin{pmatrix}A_+ & 0\\ 0 & A_-\end{pmatrix}(w_\mp)= A_\mp w_\mp.$$

Definition 12: Given a $Spin(4)$ structure, using the above representations ρ_+ and ρ_-, we can define new transition functions $\rho_\mp \circ \bar{g}_{\alpha\beta}: U_\alpha \cap U_\beta \to SU_\mp(2)$, to get two new complex bundles also denoted by $W_+$and W_-, called Spinor bundles and the relation between these bundles and TM is $TM \otimes \mathbb{C} \cong \mathrm{Hom}(W_+, W_-)$.

Therefore a $Spin$ structure determines $TM \otimes \mathbb{C} \cong \mathrm{Hom}(W_+, W_-)$. Moreover if we also have a line bundle L, $TM \otimes \mathbb{C} \cong \mathrm{Hom}(W_+ \otimes \mathrm{L}, W_- \otimes \mathrm{L})$, since $L \otimes L^*$ is the trivial bundle.

Given a $Spin(4)$ structure $\{(U_\alpha, \bar{g}_{\alpha\beta})\}$, if we have a line bundle L with transition functions $h_{\alpha\beta}: U_\alpha \cap U_\beta \to U(1)$ then we can define a $Spin^c(4)$ structure with the transition functions $h_{\alpha\beta} * \bar{g}_{\alpha\beta}: U_\alpha \cap U_\beta \to Spin^c(4)$, where for $x \in U_\alpha \cap U_\beta$ if $\bar{g}_{\alpha\beta}(x) = \begin{pmatrix}A_+ & 0\\ 0 & A_-\end{pmatrix}$ and if $h_{\alpha\beta}(x) = \lambda$ then $h_{\alpha\beta} * \bar{g}_{\alpha\beta}(x) = \begin{pmatrix}\lambda A_+ & 0\\ 0 & \lambda A_-\end{pmatrix}$. Note that these maps also satisfy the cocycle condition.

More generally, a $Spin^c(4)$ structure can be defined as $\bar{g}_{\alpha\beta}: U_\alpha \cap U_\beta \to Spin^c(4)$ with cocycle condition. That is one doesn't need to have a $Spin(4)$ structure or a line bundle in the first place. Combining this with π we get a complex line bundle, denoted by L^2. Finally, given a $Spin^c(4)$ structure, associated to it we can define two bundles $W^+ \otimes L$

and $W^- \otimes L$ although L may not exist. $W^{\mp} \otimes$L is the bundle whose transition data is $\rho_{\mp}^{c} \circ \bar{g}_{\mp}$ where $\rho_{\mp}^{c}\begin{pmatrix} \lambda A_+ & 0 \\ 0 & \lambda A_- \end{pmatrix}(w_{\mp}) = \lambda A_{\mp} w_{\mp}$. Note that $TM \otimes \mathbb{C} \cong \mathrm{Hom}(W_+ \otimes L, W_- \otimes L)$.

Definition 13: Given an $SO(4)$ structure on $T(M)$ and $U(1)$ structure, that is, a complex structure, on line bundle L over M, an associated $Spin^c(4)$ structure is a principal $Spin^c(4)$ bundle $P \to M$ such that the associated frame bundles satisfy $P_{SO(4)}(TM) = P \times_{\rho^c} SO(4)$ and $P_{S^1}(L) = P \times_{\pi} S^1$, where $\rho^c\,[A_+, A_-, \lambda](Q) = [A_+, A_-](Q) = A_- Q {A_+}^{-1}$ and $\pi\,[A_+, A_-, \lambda] = \lambda^2$.

From the obstruction theory, we know that these liftings exist when L is a characteristic line bundle, in other words, when the first chern class of L is equivalent to the second Steifel Withney class of the tangent bundle (i.e, $c_1(L) \equiv w_2(TM)\ mod 2$), as the only obstruction for these liftings to exist is $w_2(TM \otimes L) \equiv c_1(L) + w_2(TM) \in H^2(M, Z_2)$.

Note that the assumption M is compact oriented smooth 4-manifold guarantees the existence of $Spin^c(4)$ structure. Moreover, the assumption that M is simply connected ensures that the liftings considered above are unique.

2.5. Gauge Group

Definition 14: A gauge transformation on a line bundle L is a bundle homomorphism $h: L \to L$ commuting with the action of the structure group $U(1)$. That is $h(g \bullet a) = g \bullet h(a)$ for all $g \in U(1)$.

The set of all gauge transformations of L forms a group, denoted by $\mathcal{G}(L)$, under composition. This group can be considered as maps $f: M \to S^1$, see Section 1.7 of [5] for details. Hence we have $\mathcal{G}(L) \cong$ Map(M, S^1).

We define an action of the gauge group $\mathcal{G}(L)$ on $A(L)$ by $g \bullet d_A = d_A + g d g^{-1}$ which can also be expressed as $g \circ d_A \circ g^{-1}$. Action of $\mathcal{G}(L)$ on $\Gamma(W^+)$ is just complex multiplication.

Note that if we regard $\mathcal{G}(L)$ as Map(M, S^1) then, since M is simply connected, any $g \in \mathcal{G} \cong Map(M, S^1)$ can be written as $g = e^{iu}$ for some $u: M \to R$. According to this representation, $g \bullet (d_A - ia, \psi) = (d_{A_0} - i(a + du), e^{iu}\psi)$.

Fix a base point $P_0 \in M$ and define $\mathcal{G}_\circ(L) = \{g \in \mathcal{G}(L); g(P_0) = 1\}$

We have the isomorphism $\mathcal{G}(L) \to \mathcal{G}_\circ(L) \times S^1$ defined by $h \to (s^{-1}h, s)$ where $s = h(P_0) \in S^1; h \in Map(M, S^1) = \mathcal{G}(L)$.

Note that $\mathcal{G}(L)$acts freely on $A(L)$ since $d_A + g d g^{-1} = d_A$ means $g d g^{-1} = 0$ that $d g^{-1} = 0$ which holds if and only if g=constant. Elements of S^1 are constant functions $M \to S^1$. Hence S^1 acts trivially on $A(L)$, whereas it acts freely on $\Gamma(W^+ - 0)$ as complex multiplication.

Definition 15: The Dirac operator D_A: $\Gamma(W^+ \otimes L) \to \Gamma(W^+ \otimes L)$, is defined by $D_A(\psi) = \sum_{i=1}^{4} e_i \bullet d_A \psi(e_i) = \sum_{i=1}^{4} \rho(e_i) \nabla_A \psi(e_i)$, where $d_A: \Gamma(W \otimes L) \to \Gamma\big(T^*\mathrm{M} \otimes$

$(\mathrm{W} \otimes L)\big) \cong Hom_{C^\infty(M)}(\mathrm{TM}, \mathrm{W} \otimes L)$, $e_i \in \mathrm{TM} \otimes \mathrm{C} \subseteq \mathrm{End}(W \otimes L)$ and $e^i \in T^*\mathrm{M} \otimes \mathrm{C}$ are orthonormal basis, ∇_{e_i} is the covariant derivative along e_i.

2.6. Seiberg − Witten Equations

Let M be oriented, Riemannian 4-manifold with a $Spin^c(4)$ structure. We consider the pairs (d_A,ψ) where d_A is a connection on L^2 and $\psi \in \Gamma(W^+ \otimes L)$. Let $\{(d_{A_0} - ia, \psi)\}$ denote the configuration space. Seiberg-Witten equations are defined as

$$D_A^+ \psi = 0$$

$$F_A^+ = i\sigma(\psi)$$

where $F_A^+ \in \Gamma\big(\Omega^2(T^*\mathrm{M} \otimes \mathrm{iR})\big) = \Omega^2(M)$.

Notation: $M^{\sim}(L)$ denotes the moduli space of $\mathcal{G}_\circ$ (L) equivalence classes of the solutions of the Seiberg-Witten equations, $M(L)$ denotes the moduli space of gauge equivalence classes of the solutions of the Seiberg-Witten equations. That is

$$M(L) = \{(A,\psi) \in A(L) \times \Gamma(W^+ \otimes \mathrm{L});\ D_A^+ \psi = 0\ and F_A^+ = i\sigma(\psi)\}/\mathcal{G}$$

$$= M^{\sim}(L)/S^1$$

In a similar manner, one can define the perturbed Seiberg-Witten equations:

$$D_A^+ \psi = 0$$

$$F_A^+ = i\sigma(\psi) - \Phi$$

and the corresponding perturbed moduli space $M_\Phi(L)$.

3. Results

Topology of Moduli Space of Invariant Solutions of Seiberg-Witten Equations

In this section, using the fact that Seiberg Witten equations are invariant under G-action, compactness and the manifold structure on the moduli space, whenever this structure exists, will be discussed.

Given a smooth closed 4-manifold M with a Riemannian metric on it and a characteristic line bundle L over M. Let G be a compact Lie group acting on the base manifold M to preserve the inner product and orientation, also acting on the characteristic line bundle L, commuting with the base projection and mapping fibers directly to fibers as a complex linear map. That is, let L be a G-line bundle. We will also assume that the G-action on L lifts to the associated $Spin^c(4)$ bundle whose determinant line bundle is L. Furthermore, we will take G a cyclic group of order α we will also assume that M/G has a positive

definite intersection form, and that $H^1(M/G;R)=0$. Note that since G is finite and preserves the orientation, M/G is a real homology manifold, that is M/Gsatisfies Poincare duality with coefficients in R. Hence $\frac{M}{G}$ has a well defined intersection form over R. Moreover Seiberg-Witten equations are invariant under the action of G.

Main Theorem 1: If M is simply connected, then for every choice of G-invariant self dual form $\Phi \in \Omega_+^G$, the moduli space $\tilde{M}_\Phi^G$ is compact.

It is known that every sequence of $\mathcal{G}_\infty(L)$ classes of solutions to the perturbed Seiberg Witten equations has a convergent subsequence. A detailed proof is given in section 3.3 of [5]. Using the continuity of the G-action, $\tilde{M}_\Phi^G$ can be identified with a closed subspace of $\tilde{M}_\Phi(L)$. Being a closed subspace of a compact space, $\tilde{M}_\Phi^G$ is also compact.

Main Theorem 2: Let M be a closed, simply connected smooth 4-manifold with a $Spin^c(4)$-structure. If dimension of G-fixed self dual two forms, that is $b_+^G > 0$ then, $M(L)_\Phi^G$ is, for a generic choice of G-invariant self-dual two form Φ, an oriented smooth manifold of dimension $d^G = ind_R\, D_A^G - b_+^G - 1$, where $ind_R\, D_A^G$denotes the index of the dirac operator D_A^G.

The existence of a reducible solution in $\tilde{M}(L)_\Phi^G$, which causes singularity in $M(L)_\Phi^G$ depends on the condition that $c_1(L)$ contains a connection with $F_A^+ = 0$, in turn which occurs only if $\Phi \in \Pi^G$- a subspace of Ω_+^G of codimension b_+^G. Since, by the assumption $b_+^G > 0$, these singularities are avoidable. Hence $S^1 \subseteq G$ acts freely on $\tilde{M}(L)_\Phi^G$. Therefore $M(L)_\Phi^G$ is an oriented smooth manifold with $dim(M(L)_\Phi^G) = dim(\tilde{M}(L)_\Phi^G) - 1 = ind_R\, D_A^G - b_+^G - 1$. The orientation of $M(L)_\Phi^G$ is induced from the orientation of $\tilde{M}(L)_\Phi^G$.

4. Conclusion

In this work we prove that, under certain conditions on the given group action on the base manifold, the compactness of the moduli space and give manifold structure and compute the dimension of it. As a future work we will concentrate on the case where $b_+^G = 0$ and try to understand special structures near singularities

Authorship contribution statement

M. Uğuz: All work done in preparation of this paper.

Declaration of competing interest

The author declares that he has no known competing financial interests or personal relationships that could have appeared to influence the work reported in this paper.

Ethics Committee Approval and/or Informed Consent Information

As the author of this study, I declare that I do not have any ethics committee approval and/or informed consent statement.

References

[1] J. H. C. Whitehead, "On simply-connected 4-dimensional polyhedral",*Comment. Math.Helv.*, 22:48–92, 1949.

[2] S.K. Donaldson and P.B. Kronheimer, The Geometry of Four-Manifolds, Clarendon Press- Oxford, 1990.

[3] M.Freedman, “The topology of four dimensional manifolds”, *J. Diff. Geo.*, 17:357–454, 1982.
[4] J.W. Milnor and D. Husemoller, “Symmetric Bilinear Forms”, Ergebnisse der Mathematik und ihrer Grezgebiete, Volume 73. Springer Verlag, New York-Heidelberg-Berlin, 1973.
[5] John D. Moore, Lectures on Seiberg-Witten Invariants. Springer Verlag, 1996.
[6] Ted Petrie and John Randall. Connections,Definite Forms, and Four-Manifolds. Clarendon Press Oxford, 1990.
[7] John W. Morgan. The Seiberg-Witten Equations and Application to the Topology of Smooth four-Manifolds. Princeton University Press, 1996.
[8] Daniel S. Freed, Karen K. Uhlenbeck Instantons and 4-Manifolds. Springer-Verlag, 1984.

Süleyman Demirel Üniversitesi Fen Edebiyat Fakültesi Fen Dergisi https://dergipark.org.tr/sdufeffd
Süleyman Demirel University Faculty of Arts and Sciences Journal of Science e-ISSN: 1306-7575
Research Article, 2024, 19(1): 18-28, DOI: 10.29233/sdufeffd.1375580

Increasing the biomethane yield of hazelnut by-products by low temperature thermal pretreatment

Halil ŞENOL[1], Muhammed OYAN[2], Emre GÖRGÜN*[3]

[1]Giresun University, Faculty of Engineering, Department of Energy Systems Engineering, 28200, Giresun, Türkiye
https://orcid.org/0000-0003-3056-5013
halil.senol@giresun.edu.tr

[2]Kahta Hydrolic Power Plant, 02400, Kahta, Adıyaman, Türkiye
https://orcid.org/0000-0003-1431-1902
muhammed1oyan@gmail.com

[3]Sivas Cumhuriyet University, Department of Railway Systems, Sivas Vocational School of Technical Sciences, 58104, Sivas, Türkiye
https://orcid.org/my-orcid?orcid=0000-0002-1971-456X
*corresponding author: emregorgun@cumhuriyet.edu.tr

(Received: 13.10.2023, Accepted: 12.02.2024, Published: 27.05.2024)

Abstract: Biomethane energy, which has the status of renewable energies, has the potential to be produced from all kinds of organic wastes, as well as from lignocellulosic materials, which are the most common in nature. In this study, hazelnut shells (HS), one of the hazelnut by-products, were used for biomethane production. In order to obtain higher yields from HS, thermal pre-treatments were applied at temperatures of 60°C, 80°C and 100°C. Pretreatment effects were controlled by lignocellulosic substance amount determinations. As a result of thermal pretreatment at 100°C for 2 h, cellulose and lignin removals occurred approximately 15% and 30%, respectively. While the cumulative biomethane yield of raw HS was 32.3 mL•g total solids $(TS)^{-1}$, the cumulative biomethane yields of 100°C pretreated HS were measured as 132.3 $mL•gTS^{-1}$. As a result of different pretreatment temperatures, different cumulative biomethane yield curves were successfully simulated with the Modified Gompertz equation and R^2 values were found to be between 0.9962 - 0.9985.

Key words: Renewable energy, sigmoidal models, hazelnut shells, biogas

1. Introduction

As countries grow rapidly in terms of industry and population, the energy needs of industrially developed and developing countries are increasing day by day. Energy need has become an important problem in the world today. The demand for energy leads to the decrease of fossil fuels (natural gas, coal, lignite, etc.) [1]. Depleting natural energy resources have led the world to search for new energy. One of the renewable energies is biogas/biomethane energy, which replaces depleting natural gas [2].

Biogas can be produced from organic materials by the anaerobic digestion (AD) method. AS treatment of wastes with high water content has been a generally preferred

method in recent years due to its advantages such as high performance, low cost and energy production. Especially, AD applications are common in the treatment of domestic and industrial wastewater, animal manure and solid waste. AD method requires less energy and nutrient resources compared to other commonly used purification techniques [3]. Biogas content contains approximately 50 - 80% CH_4, 20-50% CO_2, 0.1-1% N_2, 0.01 - 0.2% O_2 and 10-4000 ppm H_2S is present [4-6, 8].

Biogas can be produced from different organic substances as well as lignocellulosic components [5]. Lignocellulosic organic matter refers to structures containing cellulose, hemicellulose and lignin in its structure and forms the structure of plant-derived biomass. Biogas production from lignocellulosic biomass without pretreatment is quite inefficient [6]. For this purpose, several innovative pretreatment technologies have been developed [7]. One of these is thermal pre-treatment methods, which were developed both for the environment and for their ease of applicability [8]. Thermal pretreatment is a type of physical pretreatment in which lignocellulosic biomass is subjected to heating at a certain temperature and pressure, and accordingly, the temperature range for thermal pretreatment can be 50–240°C [9].

One of the most underrated lignocellulosic components in AD is hazelnut by-products. In previous studies, hydrothermal and ultrasonic pretreatment of hazelnut shells (HS), one of the hazelnut by-products, was applied before AD [10]. In another study, thermal pretreatment optimization was performed on HS at high temperatures (50, 100 and 150°C) [11]. Apart from these studies, the biomethane yield of HS without pretreatment was investigated and the biomethane yield was obtained as 40.03 ± 4.30 mL/g volatile solids (VS) [12]. Apart from these studies, to the best of the authors' knowledge, there is no study that increases the biomethane/biogas yield of HS, one of the hazelnut by-products. Thus, there is a need to apply thermal pre-treatments to HS at lower temperatures (especially below 100°C) and longer application times and to conduct more in-depth research.

In this context, the aim of this study was to examine the lignocellulosic change in the structure of the HS and the differences in biomethane potential by applying thermal pre-treatment to raw HS at temperatures below 100°C for 2 hours. In this context, total solids (TS), VS, cellulose, hemicellulose and lignin analyzes of HS were performed before pre-treatment. Similar analyzes were performed after thermal pretreatment and the results were compared.

2. Material and Method

2.1. Substrate and inoculum

HS, one of the hazelnut by-products, was chosen as the substrate for AD. Sewage sludge from the wastewater treatment plant was used as inoculum. Raw materials were stored at 4°C before use.

2.2. Thermal pre-treatments

Thermal pretreatments were applied to HS at 60, 80 and 100°C [10]. Pre-treatments were applied in the oven. Thermal pretreatment time for each sample was kept constant as 2 hours. For each reactor, 2 g of dry reactor residue was added to the autoclave flask. 5 g of distilled water was added to prevent dry biomass from burning during thermal pretreatment. As a result of the pre-treatment, solubility was determined by filtering the slurry with glass cotton [11].

2.3. Anaerobic digestion tests

AD experiments were carried out in 500 mL conical flasks. 400 mL of these AD bottles was used as the effective volume and 100 mL was set as the head space. The TS ratio was chosen as 10% for all anaerobic bottles [13]. The inoculum/substrate ratio was taken as 1.0 on the basis of organic matter in the effective volume of 400 mL [14]. After the inoculum-substrate ratio was completed, N_2 gas was purged for 5 minutes to eliminate oxygen in the head space [15]. In the established setup, 5 types of reactors were prepared: 60°C, 80°C and 100°C pre-treatment reactor, control reactor and the reactor containing only the inoculum. A total of 10 reactors were prepared, each with two floors. In order to ensure AD conditions, the top was closed with a cork stopper and a mechanism containing gas bags was installed. The outer surface temperature (AD temperature) in the water bath was set at 37 ± 1.5°C. After AD conditions were achieved, the system was left to produce biogas, and during this process, each reactor was manually stirred every 24 hours. During the anaerobic process, gas volume was measured every 3 days and CH_4 content analyzes were performed. The AD test lasted approximately 39 days, and as a result of this period, the gases accumulated in the reactors were collected. Then, the net biomethane yield of the HS was calculated by subtracting the biomethane yield of the inoculum from the biomethane efficiency of the reactor containing the inoculum and HS. These gases were then saved for content analysis [15].

2.4 Analytical methods

TS and VS values of HS were analyzed according to APHA standards [16]. Cellulose, hemicellulose and lignin contents were measured using fiber analyzer (ANKOM A2000i, USA) [17]. Content analysis of the biogas obtained from AD experiments was performed with a portable biogas measuring device called IRCD4 Multi-Gas Detecting Alarm Manual Instruction. For this purpose, an average of 10-50 mL was taken from each biogas sample and the CH_4, CO_2, H_2S and O_2 values were determined with an average sensitivity of 1%. Scanning electron microscopy (SEM) images were acquired at x350 magnification values using a SU–1510 SEM (Hitachi, Japan), after preparing the raw and pretreated HS samples [14].

2.5 Kinetic study

In AD, the proliferation rate of microorganisms and the CH_4 gas production rate are directly proportional [14]. For this reason, the gas volumes determined cumulatively in the AD process were simulated with the modified Gompertz equation. MATLAB® (R2021a) program was used to obtain kinetic parameters in cumulative measurements. Then, the estimated values of the modified Gomperz equation were found. The modified Gompertz equation is given in Eq. (1) [8].

$$y = Ae^{\left(-e^{\left[\frac{\mu_m e(\lambda - t)}{A} + 1\right]}\right)} \quad (1)$$

Where, A: Maximum biogas production amount (mL/g VS), e: 2.71828, λ: Delay time (days), t: Time and μ_m: Defined as specific biogas production rate (mL/g VS. day).

3. Results

3.1. Physicochemical properties of substrate and inoculum

The physicochemical properties of HS, which are hazelnut by-products, and wastewater treatment sludge used as inoculum are given in Table 1. In Table 1, the TS value of the

HS was reported as 92.4%, while the TS value of the inoculum was reported as 14.06%. While there is a significant potential in the VS rate of HS (90.87%), the VS rate of the inoculum is quite low (66.12%). In one study, the TS and VS values of HS were determined as 85.45 and 76.96, respectively [18]. In another study, TS and VS values were found to be 91.58 and 89.94, respectively [19]. As a result, previous studies support the values in Table 1.

Table 1. Physicochemical properties of raw hazelnut shell and inoculum used in the study

Parameters	Raw hazelnut shell	Inoculum
(TS) (%w/w)	92.40	14.06
(VS) (%TS)	90.87	66.12
pH	-	7.29
Cellulose (%w/w)	19.51	-
Hemicellulose (%w/w)	18.48	-
Lignin (%w/w)	36.07	-

Note: O content was found by subtracting the sum of C, H, N and S content from 100%

3.2. Effect of pretreatments on lignosulosic structure

In addition to the elemental content of HS, the lignocellulosic content in HS was determined. Accordingly, the cellulose, hemicellulose and lignin contents in raw HS were determined as 19.51%, 18.48% and 36.07% by weight, respectively. A literature search was conducted to test the consistency of the results of the analyses, and the results of lignocellulosic analyzes in HS were compared with the results reported by Bianco et al. [10]. Cellulose, hemicellulose and lignin values were found to be 26.11%, 29.8%, 42.48% by weight, respectively. The reason for this difference may be due to measurement error or sample difference. In another study, the cellulose, hemicellulose and lignin values of HS were 27.55%, 28.92%, 39.91% by weight, respectively, showing similar results with the amount of lignocellulosic substance declared in this study [11].

Table 2. Physicochemical properties of pre-treated hazelnut shells.

		Thermal pre-treatments conditions		
Parameters	**Control**	**60°C and 2 h**	**80°C and 2 h**	**100°C and 2 h**
Cellulose (%w/w)	19.51	18.5	16.8	15.39
Hemicellulose (%w/w)	18.48	17.8	16.5	15.0
Lignin (%w/w)	36.07	35.0	33.3	29.9

Cellulose is considered the main lignocellulosic component for biogas production. The amount of cellulose plays a vital role in any biochemical process. In one study was stated that the maximum degradation of glucan was only 2.8% at 160°C and increased to 14.7% after pretreatment at 200°C for 120 min [20]. In this study, looking at the values in Table 2., the cellulose value of raw HS is 19.51%; As a result of pre-treatment at 60°C and 2 hours, 1.1% cellulose was dissolved and reached 18.5% by weight. As a result of pre-treatment at 80°C and 2 hours, 2.7% cellulose was dissolved and reached 16.8% by weight. As a result of pre-treatment at 100°C and 2 hours, 4.1% cellulose was

dissolved and reached 15.39% by weight. Cellulose removal as a result of pretreatment at 80°C increased by 1.7% compared to the pretreatment result at 60°C; Cellulose removal as a result of pretreatment at 100°C increased by 1.41% compared to the pretreatment result at 80°C. When the results are compared, the highest cellulose removal occurred as a result of the pre-treatment at 100°C.

Hemicellulose is a type of heterogeneous polysaccharide and contains hexoses, pentoses, uronic acid sugars. In the hemicellulose structure, the hydroxyl group of the sugars is partially replaced by the acetyl group [21]. While the hemicellulose value of raw HS in this study was 18.48%; As a result of pre-treatment at 60°C and 2 hours, 0.6% hemicellulose dissolved and reached 17.8% by weight. As a result of pre-treatment at 80°C and 2 hours, 1.9% hemicellulose dissolved and reached 16.5% by weight. As a result of pre-treatment at 100°C and two hours, 3.4% hemicellulose was dissolved and reached 15.0% by weight. Hemicellulose removal as a result of pretreatment at 80°C increased by 1.3% compared to the pretreatment result at 60°C; Hemicellulose removal as a result of pretreatment at 100°C increased by 1.5% compared to the pretreatment result at 80°C. When the results are compared, the highest hemicellulose removal occurred as a result of pre-treatment at 100°C.

The presence of lignin is a vital factor that limits the extent and rate of hydrolysis by enzymes during the biochemical reaction of lignocellulosic biomass. Studies have shown that lignin removal from lignocellulosic biomass increases cellulose digestibility [22]. In this study, the degradability of lignin was tested after thermal pretreatment in order to test the high yield of HS in the AD process. While the control value of lignin was 36.07%; As a result of 60°C and 2 hours of pre-treatment, 1% lignin was dissolved and reached 35% by weight. As a result of 80°C and 2 hours of pre-treatment, 2.7% lignin was dissolved and reached 33.3% by weight. At 100°C and As a result of 2 hours of pre-treatment, 6.1% lignin was dissolved and reached 29.9% by weight. Lignin removal as a result of pretreatment at 80°C increased by 1.7% compared to the pretreatment result at 60°C; Lignin removal as a result of pretreatment at 100°C increased by 3.4% compared to the pretreatment result at 80°C. When the results are compared, the highest lignin removal occurred as a result of pre-treatment at 100°C.

3.3. Effect of pretreatments on biomethane yields

The cumulative biomethane yields obtained in the AD process as a result of thermal pre-treatments applied to HS are calculated in ($mL \bullet gTS^{-1}$) and are given in Table 3. Accordingly, the biomethane yield of raw HS was found to be 32.3 mL gTS^{-1}. This very low value shows us that biomethane production from lignocellulosic material is very low. In order to increase this value, a thermal pre-treatment was applied at temperatures of 60°C, 80°C and 100°C and application times of 2 hours. As a result of these pre-treatments at 60°C, the biomethane yield reached from 32.3 $mL \bullet gTS^{-1}$ to 88.3 $mL \bullet gTS^{-1}$. Biomethane yield; 1.73 times as a result of pretreatment at 60°C compared to the control reactor; 2.53 times as a result of pre-treatment at 80°C; It increased 3.09 times as a result of pre-treatment at 100°C. The biogas production amount of the pretreated reactor at 80°C increased by 29.3% compared to the biogas production amount of the pretreated reactor at 60°C. The biogas production amount of the pre-treated reactor at 100°C increased by 15.8% compared to the biogas production amount of the pre-treated reactor at 80°C. According to these results, it is clear that the highest biomethane yield occurs in the reactor with 100°C and 2 hours pretreatment.

Table 3. Cumulative biomethane yields of inoculum, control and thermally pretreated hazelnut shells

Pretreatments conditions	Cumulative biomethane yields (mL·gTS^{-1})
Inoculum	15.5
Control	32.3
Thermal (60°C)	88.3
Thermal (80°C)	114.2
Thermal (100°C)	132.3

Biomethane measurements were made every 3 days in AD and the anaerobic process was completed in 39 days (Figure 1). Since biomethane yield could not be obtained in the last 3 consecutive days, the AD process was stopped and gas volumes were calculated.

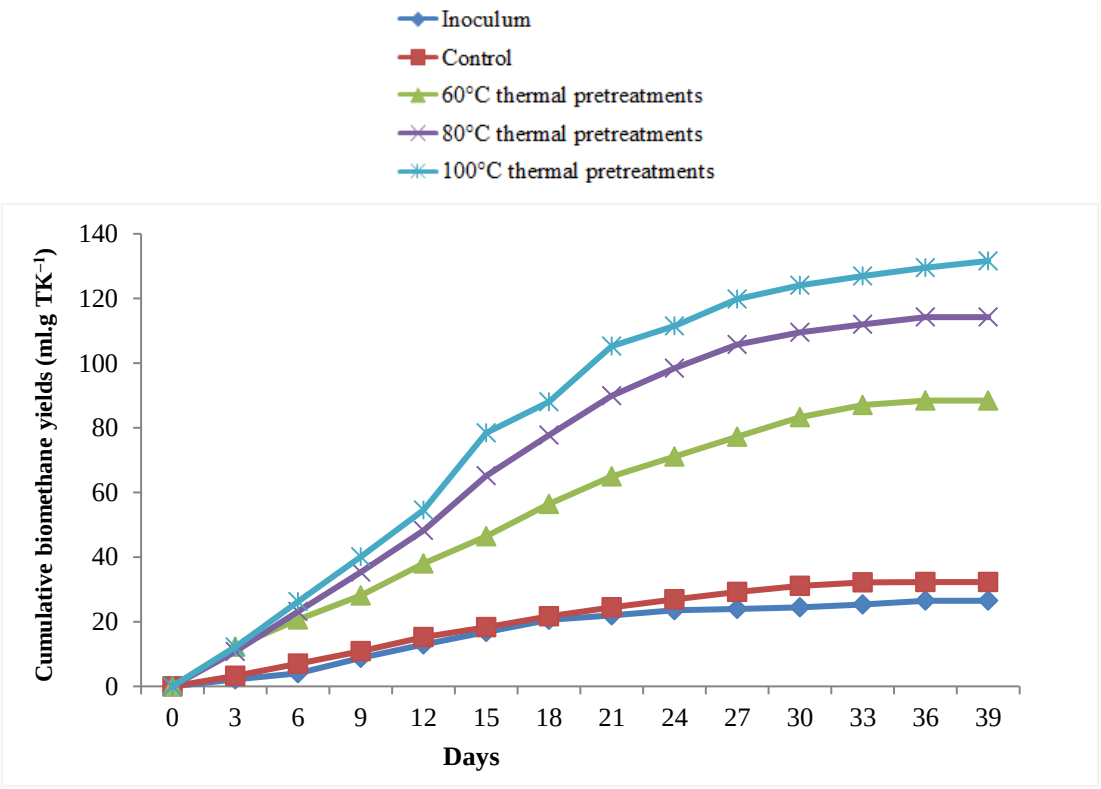

Figure 1. Cumulative biomethane yields of inoculated, control and thermally pretreated hazelnut shells

3.4. Effects of pretreatments on surface morphology

SEM images were taken to evaluate the effects of thermal pretreatments on HS. Surface images of unpretreated and pretreated HS are given in Figure 2. It is observed that the sample without pretreatment has surface hardness and crystallinity and does not contain pores (Figure 2 (a)). When the pretreatment temperature is 60°C (Figure 2 (b)), a slightly porous structure is observed. After 80°C pre-treatment (Figure 2 (c)), it appears that the surface crystallinity is broken and cracks are formed. In the SEM images of 100°C pre-treated HS, the cracks on the surface appear to increase and become extremely wide. It is clearly seen that the cracks increase and widen as the pre-treatment

temperature increases. Therefore, it can be said that the reactor with a higher pretreatment temperature is more suitable for anaerobic microorganisms in AD.

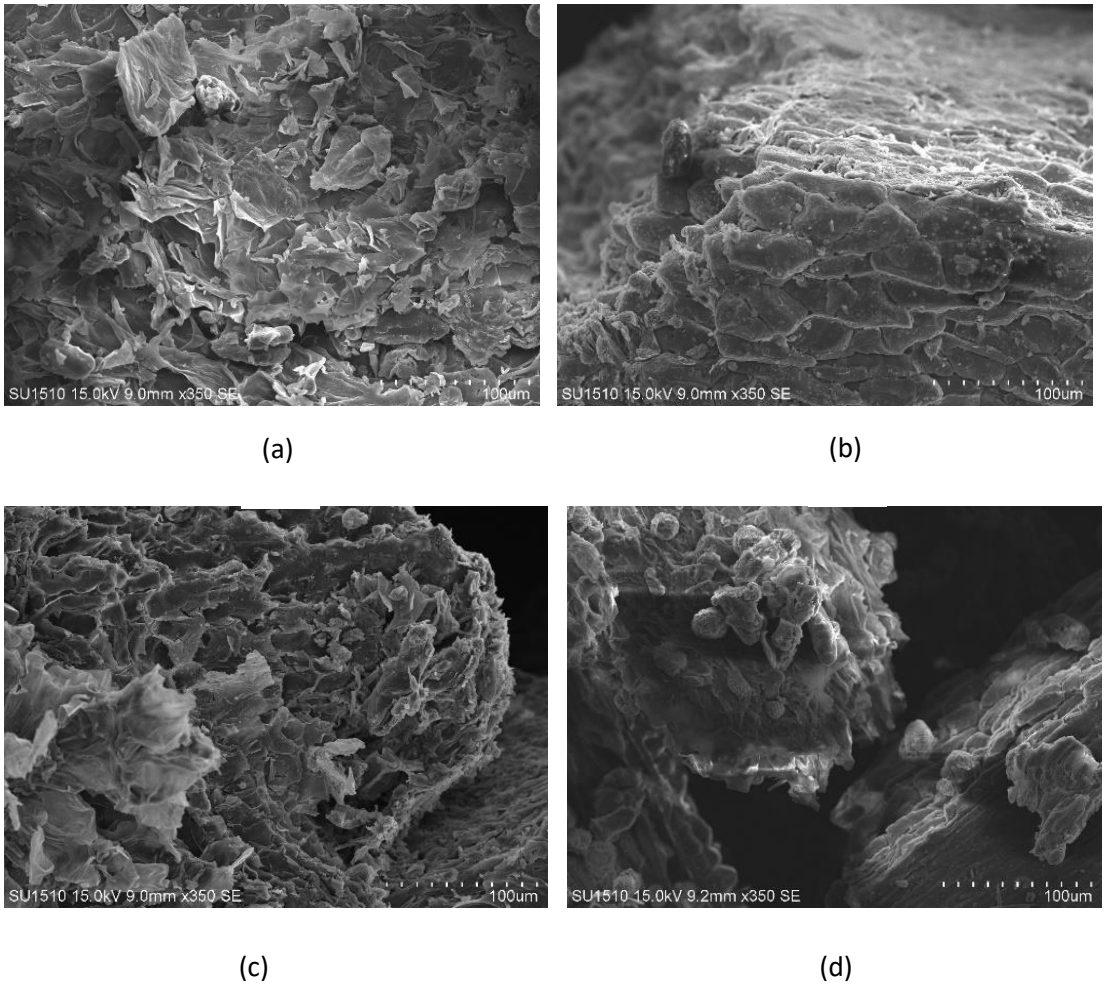

Figure 2. SEM images of hazelnut shells after thermal pre-treatment (a; no pre-treatment, b: 60°C pre-treated, c: 80°C pre-treated and d; 100°C pre-treated hazelnut shells).

3.5 Kinetic study results

Mathematical models describe the interactions of operating parameters of anaerobic microorganisms and the improvement of technical properties; It is a tool used to explain the impact on biogas production and to predict system performance [23]. In AD, the biogas production rate and proliferation rate of microorganisms are directly proportional. Thus, MATLAB® (R2019b) program was used to calculate the kinetic parameters of sigmoidal curves. Estimated biomethane values were found for the modified Gompertz model by entering the cumulative biogas production rate measured every three days into the program.

Table 4. Kinetic Parameters of the Modified Gompertz Model

Kinetic parameters	Unit	Inoculum	Control	60°C	80°C	100°C
λ	(day)	3.163	1.51	0.8901	2.371	2.424
μ_m	($mL \cdot gTS^{-1}$.gün)	1.481	1.393	3.405	5.258	6.11
A	($mL \cdot gTS^{-1}$)	26.3	34.25	96.88	120.2	136

R^2	-	0.9977	0.9973	0.9962	0.9985	0.9979

Delay time: λ ; Specific biomethane yields: μm ; Max. biogas production amount: A; coefficient of determination: R^2

According to Table 4, A value indicates maximum biomethane yields [18]. According to the modified Gompertz model, the maximum biomethane yield is 136 mL gTS^{-1} in the 100ºC pre-treated reactor. The experimental biomethane yield of the reactor with 100ºC thermal pretreatment is 132.3 mL·gTS^{-1}. The estimated maximum biomethane yield and experimental biomethane yield are consistent. Specific biomethane yields (μm) vary between 1.393 mL•g TS^{-1} and 6.11 mL•gTS^{-1}. Experimental biomethane yields and specific biomethane yields appear to be linearly consistent.

Lag times (λ) express the time required for anaerobic bacteria to start multiplying (reproducing) [24]. Since statistically significant biomethane/biogas is produced after the delay period in biogas reactors, it is desirable that the delay times be minimum in terms of cost [13]. In this study, the delay times of the vaccine, control and pre-treatment reactors obtained according to the modified Gompertz model were calculated and given in Table 4. The lowest λ value is 0.8901 days in the reactor with 60°C thermal pretreatment. When the delay times of all reactors are evaluated, the reactor with 60°C thermal pretreatment is the most suitable reactor since the delay time is desired to be minimum. If other pre-treated reactors are taken into consideration (for 80°C and 100°C pre-treated reactors, respectively), λ values were obtained as 2.371 and 2.424 days, and the closeness of the values to each other is remarkable. However, the delay period of the vaccine was found to be 3,163 days. In a study, the cumulative biomethane curves obtained as a result of AD treatment of HS, a lignocellulosic waste, were modeled with the modified Gompertz equation. As a result of the thermal pretreatment (100°C) they found in their study, the λ values (0.8956 days) are close to the values in this study [25].

Model compatibility (model performance) for reactors is determined by R^2 values [11]. R^2 value is desired to be closest to 1; The closer it is to 1, the higher the model compatibility [26]. The R^2 value closest to 1 is 0.9985 in the reactor with 80°C thermal pretreatment. Considering the highest biomethane yield, the most compatible reactor is the reactor with 80°C thermal pretreatment. According to Table 4, the R^2 value varies between 0.9962 and 0.9985. According to the results of the modified Gompertz model in a study, R^2 values vary between 0.975 and 0.993 [27]. Therefore, it can be seen that the kinetic constants obtained here are compatible with those previously given in the literature. In a study conducted to increase biomethane yield as a result of co-fermentation of cattle manure and canola waste, the R^2 value was calculated as 0.9983 in the curves obtained with the Modified Gompertz model [28]. The values of the kinetic parameters found in this study are compatible with the literature.

4. Conclusion

In this study, HS, one of the hazelnut by-products, were used as raw material for biomethane production. Since HS is a lignocellulosic substance, thermal pre-treatments have been applied so that anaerobic microorganisms can better benefit from organic substances. Biomethane measurements were made every 3 days in AD and this process was completed in 39 days.

Raw HS samples were subjected to thermal pretreatment separately at temperatures of 60°C, 80°C and 100°C for 2 hours. While the biomethane yield of raw HS is 32.3

mL•gTS^{-1}, after thermal pre-treatment, the biomethane yields for temperatures of 60°C, 80°C and 100°C are 88.3 mL•gTS^{-1}, 114.2 mL•gTS^{-1}, respectively. It was measured as 1 and 132.3 mL•gTS^{-1}. The effects of pretreatments on HS were checked by cellulose, hemicellulose and lignin analyses. Cellulose, hemicellulose and lignin values in raw HS were found to be 19.51%, 18.48% and 36.07%, respectively.

In this study, for the first time, low-temperature thermal pretreatments were applied to hazelnut by-products and successful biomethane production was achieved. The fact that biomethane yields are higher in pre-treated reactors compared to the control shows that the pre-treatment method used is appropriate. It is recommended that future experimental studies apply biomethane yields with alkaline, acid and thermochemical pretreatments of HS. Moreover, it is recommended to use raw HS in full-scale anaerobic reactors in future studies.

Authorship contribution statement

H. Şenol: Conceptualization, Original Draft Writing Methodology, Supervision;
M. Oyan: Data Curation, Original Draft Writing; Visualization,
E. Görgün: Data Curation, Original Draft Writing; Visualization,

Declaration of competing interest

The authors declare that they have no known competing financial interests or personal relationships that could have appeared to influence the work reported in this paper.

Ethics Committee Approval and/or Informed Consent Information

As the authors of this study, we declare that we do not have any ethics committee approval and/or informed consent statement.

References

[1] A. Kara and H. Şenol, ‘’Study on Accelerating Energy Conversion for Industrial Anaerobic Reactors’’*, Süleyman Demirel University Faculty of Arts and Science Journal of Science*, 17(2), 349-358, 2022.

[2] H. Şenol, A. Kara, S. Atasoy, and M. Erşan, ‘’Optimization of Nanoparticle Concentration in Anaerobic Digestion by Response Surface Method’’, *Süleyman Demirel University Faculty of Arts and Science Journal of Science, 17*(1), 209-219, 2022.

[3] C. Cavinato, F. Fatone, D. Bolzonella, and P. Pavan, ‘’Thermophilic anaerobic co-digestion of cattle manure with agro-wastes and energy crops: comparison of pilot and full scale experiences’’, *Bioresource Technology*, 101(2), 545-550, 2010.

[4] C. Font-Palma, ‘’Methods for the treatment of cattle manure a review’’, *Journal of Carbon Research*, 5(2), 27, 2019.

[5] H. Şenol, ‘’Alkaline-thermal and mild ultrasonic pretreatments for improving biomethane yields: Impact on structural properties of chestnut shells’’, *Fuel*, *354*, 129373, 2023.

[6] Z.M.A. Bundhoo and R. Mohee, ‘’Ultrasound-assisted biological conversion of biomass and waste materials to biofuels: a review’’, *Ultrason. Sonochemistry,* 40 (2018) 298–313, 2018.

[7] G. Mancini, S. Papirio, P.N.L. Lens, G. Esposito, ‘’Anaerobic digestion of lignocellulosic materials using ethanol-organosolv pretreatment’’, *Environmental Engineering Science,* 35, 953–960, 2018.

[8] İ. T. Çakır, H. Şenol, and E. Kaygusuz, ‘’Increasing the Biomethane Production of Cattle Manure in Anaerobic Bioreactor by Thermal Pretreatments’’, *The Black Sea Journal of Sciences,* 13(2), 652-664, 2023.

[9] Sohail Toor, S., L. Rosendahl, J. Hoffmann, J. B. Holm-Nielsen, and E. Augustine Ehimen, ‘’Lignocellulosic Biomass—Thermal Pre-Treatment With Steam’’, *Pretreatment Techniques For Biofuels And Biorefineries,* 59-75, 2013.

[10] F. Bianco, H. Şenol, S. Papirio, H. Zenk, A. Kara, and S. Atasoy, ‘’Combined ultrasonic–hydrothermal pretreatment to improve the biomethane potential of hazelnut shell’’, *Biomass and Bioenergy, 165*, 106554, 2022.

[11] H. Şenol, M. Erşan, and E. Görgün, ‘’Optimization of temperature and pretreatments for methane yield of hazelnut shells using the response surface methodology’’, *Fuel*, 271, 117585, 2020.

[12] J. Shen, H. Yan, R. Zhang, G. Liu, and C. Chen, ‘’Characterization and methane production of different nut residue wastes in anaerobic digestion’’, *Renewable Energy*, 116, 835-841, 2018.

[13] H. Şenol, S. Demir, and E. A. Elibol, ‘’Investigation of Biogas Production By Applying Thermal Pre-Treatment From Mixtures of Different Fruit Wastes And Organic Raw Chicken Manure Wastes*’’, Journal of the Faculty of Engineering and Architecture of Gazi University*, 35(2), 979-990, 2020.

[14] H. Şenol, ‘’Effects of Naoh, Thermal, and Combined NaOH-Thermal Pretreatments on The Biomethane Yields From The Anaerobic Digestion of Walnut Shells’’, *Environmental Science and Pollution Research*, 28(17), 21661-21673, 2021.

[15] F. Bianco, H. Şenol, and S. Papirio, ‘’Enhanced Lignocellulosic Component Removal And Biomethane Potential from Chestnut Shell by a Combined Hydrothermal–Alkaline Pretreatment’’, *Science of The Total Environment*, 762, 144178, 2021.

[16] E. W. Rice, L. Bridgewater, and American Public Health Association (Eds.), ‘’Standard Methods for the Examination of Water And Wastewater’’ (Vol. 10). Washington, DC: American public health association, 2012.

[17] Van Soest, P. V., J. B. Robertson, and B. A. Lewis, ‘’Methods for Dietary Fiber, Neutral Detergent Fiber, and Nonstarch Polysaccharides in Relation to Animal Nutrition’’, *Journal of dairy science*, *74*(10), 3583-3597, 1991.

[18] H. Şenol, ‘’Anaerobic Digestion of Hazelnut (Corylus Colurna) Husks after Alkaline Pretreatment and Determination of New İmportant Points İn Logistic Model Curves’’, *Bioresource Technology*, 300, 122660, 2020.

[19] G. Mancini, S. Papirio, P. N. Lens, and G. Esposito, ‘’Enhancement of Biogas Production from Lignocellulosic Materials by NMMO and Organosolv Pretreatments’’, *ABWET*, 70, 2017.

[20] S. Fan, P. Zhang, F. Li, S. Jin, S. Wang, and S. Zhou, ‘’A Review of Lignocellulose Change During Hydrothermal Pretreatment for Bioenergy Production’’, *Current Organic Chemistry*, 20(26), 2799-2809, 2016.

[21] S. L. Sun, S. N. Sun, J. L. Wen, X. M. Zhang, F. Peng, and R. C. Sun, ‘’Assessment of İntegrated Process Based on Hydrothermal and Alkaline Treatments for Enzymatic Saccharification Of Sweet Sorghum Stems’’, *Bioresource Technology*, 175, 473-479, 2015.

[22] Q. SYA, W. Wei, G. P. Kingori, and J. Sun, ‘’Cell Wall Disruption İn Low Temperature NaOH/Urea Solution And Its Potential Application in Lignocellulose Pretreatment’’, *Cellulose*, 22(6), 3559-3568, 2015.

[23] I. Syaichurrozi, P. K. Villta, N. Nabilah, and R. Rusdi, ‘’Effect of Sulfuric Acid Pretreatment on Biogas Production From Salvinia Molesta’’, *Journal of Environmental Chemical Engineering,* 7(1), 102857, 2019.

[24] I. Syaichurrozi, R. Rusdi, S. Dwicahyanto, and Y. S. Toron, ‘’Biogas Production From Co-Digestion Vinasse Waste and Tofu-Prosessing Waste Water and Knetics’’, *International Journal of Renewable Energy Research (IJRER),* 6(3), 1057-1070, 2016.

[25] M. D. Ibrahim and G. Imrana, ‘’Biogas Production from Lignocellulosic Materials: Co-Digestion of Corn Cobs, Groundnut Shell and Sheep Dung’’, *Imperial Journal of Interdisciplinary Research*, 2(6), 5-11, 2016.

[26] Ü. Açıkel, M. Erşan, and Y. S. Açıkel, ‘’Optimization of Critical Medium Components Using Response Surface Methodology for Lipase Production by Rhizopus Delemar’’, *Food And Bioproducts Processing*, 88(1), 31-39, 2010.

[27] H. Şenol, ‘’Methane Yield Prediction of Ultrasonic Pretreated Sewage Sludge by Means of an Artificial Neural Network’’, *Energy*, 215, 119173, 2021.

[28] M. Safari, R. Abdi, M. Adl, and J. Kafashan, ‘’Optimization of Biogas Productivity İn Lab-Scale By Response Surface Methodology’’, *Renewable Energy*, 118, 368-375, 2018.

Süleyman Demirel Üniversitesi Fen Edebiyat Fakültesi Fen Dergisi https://dergipark.org.tr/sdufeffd
Süleyman Demirel University Faculty of Arts and Sciences Journal of Science e-ISSN: 1306-7575
Research Article, 2024, 19(1): 29-39, DOI: 10.29233/sdufeffd.1418644

Examination of the Effects of Level Density Models in Cross-Section Calculations of Some (p,x) Reactions on Natural Palladium

Özlem Y. TOYKAN CIFTLIKLI[*1], Abdullah KAPLAN[1]

[1]Department of Physics, Faculty of Engineering and Natural Sciences, Süleyman Demirel University, 32260, Isparta, Turkey
https://orcid.org/0000-0002-2339-9822
ozlemtoykan@gmail.com
[1]Department of Physics, Faculty of Engineering and Natural Sciences, Süleyman Demirel University, 32260, Isparta, Turkey
https://orcid.org/0000-0003-2990-0187
abdullahkaplan@sdu.edu.tr

(Received: 12.01.2024, Accepted: 27.02.2024, Published: 27.05.2024)

Abstract:

In this study, reaction cross-section calculations of some proton-induced reactions on ^{nat}Pd have been investigated under the effects of level density models. All calculations involving level density models have been done employing the TALYS code's 1.95 version. TALYS is an open-source software. It gives foresight to the researchers about many parameters of a desired nuclear reaction, one of which is known as cross-section, when it is not possible to perform it due to specific reasons. The TALYS 1.95 code consists of six different level density models, which have all been included in this study. All obtained cross-section results gathered from the utilization of level density models have been compared with available experimental data. The mentioned available experimental data used in this study have been obtained from the International Experimental Nuclear Reaction Data Library (EXFOR) database. A graphical representation of generated calculation results, and available experimental data have been displayed for these comparisons. These graphical representations are also used to point out the most consistent level density model with respect to the experimental data for each reaction investigated in this study. The use of level density models was found to affect the results of cross-sectional calculations.

Keywords: Palladium, Cross-section, Level density, EXFOR

1. Introduction

Palladium (Pd), a platinum group metal element, is widely used in many industrial fields such as many industries of electronics and petroleum, manufacturing of electrode and ceramic capacitors, surgical instruments, jewelries, composite dental alloys, and wastewater treatment. This widespread use makes palladium one of the most valuable members of the platinum group metals. The importance of platinum group metals, and their isotopes has increased in recent years as the industrial, and technological needs have increased. From a different perspective, the fact that many precious metals, including platinum group elements, are waiting as nuclear waste has led researchers to study these materials. Ongoing studies on the recovery of nuclear waste, and alternative production techniques for valuable isotopes are of universal importance [1-3].

Natural palladium consists of six stable isotopes, which are; ^{102}Pd, ^{104}Pd, ^{105}Pd, ^{106}Pd, ^{108}Pd, and ^{110}Pd. The relative abundances of these palladium isotopes are; 1.02 %, 11.1 %, 22.3 %, 27.3 %, 26.5 %, and 11.7 %, respectively. The half-lives ($t_{1/2}$) of some unstable isotopes of palladium are 6.5 million years for ^{107}Pd, 17 days for ^{103}Pd, 3.63 days for ^{100}Pd, 8.47 for hours ^{101}Pd, 13.7 hours for ^{109}Pd, and 21 hours for ^{112}Pd [4].

In this study, natural isotope of palladium has been used as target, and the effects of level density models on the cross-section calculations for (p,x) reactions on ^{nat}Pd-targeted reactions have been investigated. The term cross-section can be defined simply, and succinctly as the probability of a nuclear reaction taking place. It is very important in determining the atomic structure in atomic, and molecular physics in addition to the understanding of the mechanisms of a nuclear reaction in nuclear physics. There are many parameters that is known to affect the theoretical cross-section calculations where one of them is the level density models. The term level density can be defined as the number of excited energy levels in an infinite energy range [5].

In many cases, the cross-section values can be obtained by performing specific reactions. However, there may be cases where many reasons create obstructions to achieving the desired typical reaction. In these circumstances, theoretically obtained cross-section values may give researchers a foresight. To avoid from any mistake, fault, error or any other human origin negative outcome, that may arise while performing the hand-made calculations, computer aided software have been used to obtain the cross-section results for a specific reaction. For this purpose, many codes have been developed such as CEM95 [6], EMPIRE [7], GEANT [8], ALICE/ASH [9], PCROSS [10], and TALYS [11]. In this study, the code TALYS with the version of 1.95 has been utilized to perform the level density model included calculations. The motivation for selecting the TALYS code in this study is directly related to the existing literature in which the performance, reliability, compatibility, and wide usage possibilities are shown in many studies [12-21].

As of gathering the calculation results obtained via utilizing the level density models of the TALYS code, the need of their comparison has arisen. To perform a logic, and equitable comparison of the obtained cross-section results, experimental data for each investigated reaction have been used. These mentioned experimental are taken from a database, known as the EXFOR [22, 23], which is a freely accessible online platform. All calculation results, and experimental data have been graphed together for each reaction to perform a visual representation, and comparison. As a result of these graphical representations, the level density model that gives the most consistent outcomes with the experimental data have been able to point out.

2. Material and Method

As mentioned earlier this paper aims to investigate the effects of level density models on the cross-section calculations of (p,x) reactions on ^{nat}Pd. To this end, six different level density models which are available in the version 1.95 of the TALYS code have been employed. TALYS is a computer software, which is developed to provide various calculations in accordance with the users' wishes, and directions given in an input file. This input file must contains four fundamental, and mandatory parameters, such as the name of the projectile, the energy range of the incident particle, symbol or name of the target, and the atomic mass number of the target. In addition to all these, users may change other parameters which allows them to manipulate various models, and parameters. The power of the TALYS code and one of its common preferring reasons lies along in its strong ability to change models, and their parameters. Each model and/or parameter is defined by a keyword in TALYS, and there are more than 600 keywords. Some examples

of these parameters are related to masses, and deformations, discrete levels, level densities, gamma emissions, optical models, astrophysics, medical isotope production, and etc. [11]. Many studies in the literature can be shown where some of these parameters' effects on different calculations have been examined [13-16].

In simple terms, level density can be defined as the number of excited energy levels in an infinite energy range, or the function used to determine these energy ranges. This model neglects the interaction of nucleons with each other and assumes that the particles in the single-particle system are placed in equal energy levels, and do not contain collective levels [5]. The code TALYS includes six level density models, of which the default one is based on the Fermi Gas Model (FGM) [24]. The TALYS code contains six different six-level density models. Three of these models can be grouped as phenomenological models hypothetically based on the FGM [24]. Among the phenomenological models, the so-called Constant Temperature Fermi Gas Model (CT+FGM) was developed to correct the failure of the FGM in the high energy region by assuming that constant temperature laws are valid in the zero-match energy range, and the FGM is valid in the higher energy region [25, 26]. In addition to this model, many modifications, and developments have been done over the years with respect to the improvements in the theoretical models. Herewith, TALYS contains two more phenomenological level density models, which are named as Back Shifted Fermi Gas Model (BSFGM) [27, 28], and Generalized Superfluid Model (GSM) [29, 30].

In addition to these phenomenological level density models, TALYS offers three microscopic level density models to the users. These models are named after the scientists who came up with the idea of the development of these models and provide indisputable contributions to the literature. The microscopic level density models are implemented into the TALYS code from the study of Goriely et al., [31], Hilaire, and Goriely [32], Hilaire et al., [33]. In the rest of this study, all level density models are shown with abbreviations. In this direction, abbreviations for phenomenological level density models are used as given above. On the other hand, for microscopic level density models, names of the models, and abbreviations are used as given below; Skyrme Force-Goriely level densities from numerical tables (SFG) [31], Skyrme Force-Hilaire level densities from numerical tables (SFH) [32], and Temperature-dependent Gogny-Hartree-Fock-Bogoluybov level densities from numerical tables (GFD) [33]. In this study, ^{nat}Pd(p,x)^{97}Ru, ^{nat}Pd(p,x)^{100}Pd, ^{nat}Pd(p,x)^{101}Pd, ^{nat}Pd(p,x)^{103}Ag, ^{nat}Pd(p,x)^{103}Ru, ^{nat}Pd(p,x)^{105}Ag reactions have been selected where all include ^{nat}Pd as target, and proton as incident particle. In each reaction, all mentioned level density models have been utilized, and reaction cross-section calculations have been done with the TALYS code's 1.95 version. Obtained results have been compared with each other, and available experimental data for each reaction, and the findings are given as graphical representations.

3. Results

In this study, seven proton-induced reactions for the ^{nat}Pd isotope have been investigated. The reactions investigated in this study are ^{nat}Pd(p,x)^{97}Ru, ^{nat}Pd(p,x)^{100}Pd, ^{nat}Pd(p,x)^{101}Pd, ^{nat}Pd(p,x)^{103}Ag, ^{nat}Pd(p,x)^{103}Ru, ^{nat}Pd(p,x)^{105}Ag, and ^{nat}Pd(p,x)^{105}Rh. Figures 1-7 show the comparisons between the computational results, and available experimental data of six different level density models for each reaction.

The cross-section values of the ^{nat}Pd(p,x)^{97}Ru reaction, which takes place around the energy range of 30-80 MeV. The experimental data for this reaction are taken from the studies of Tarkanyi et al. [34], and Ditrio et al. [35]. The compatibility of these data with the calculation results have been shown in Figure 1. As can be clearly seen from this

figure, between the energy range of around 30 MeV to 55 MeV almost all theoretical calculation results are obtained below the experimental data. Other than this energy region, which falls between the energy range of around 55 MeV to 80 MeV, the model results became closer to each other, and some of them approached the experimental data more than the others. It is seen that the closest fit with the experimental results is achieved with the GFD model, while the GSM is lower than the data obtained with other models, and the experimental results.

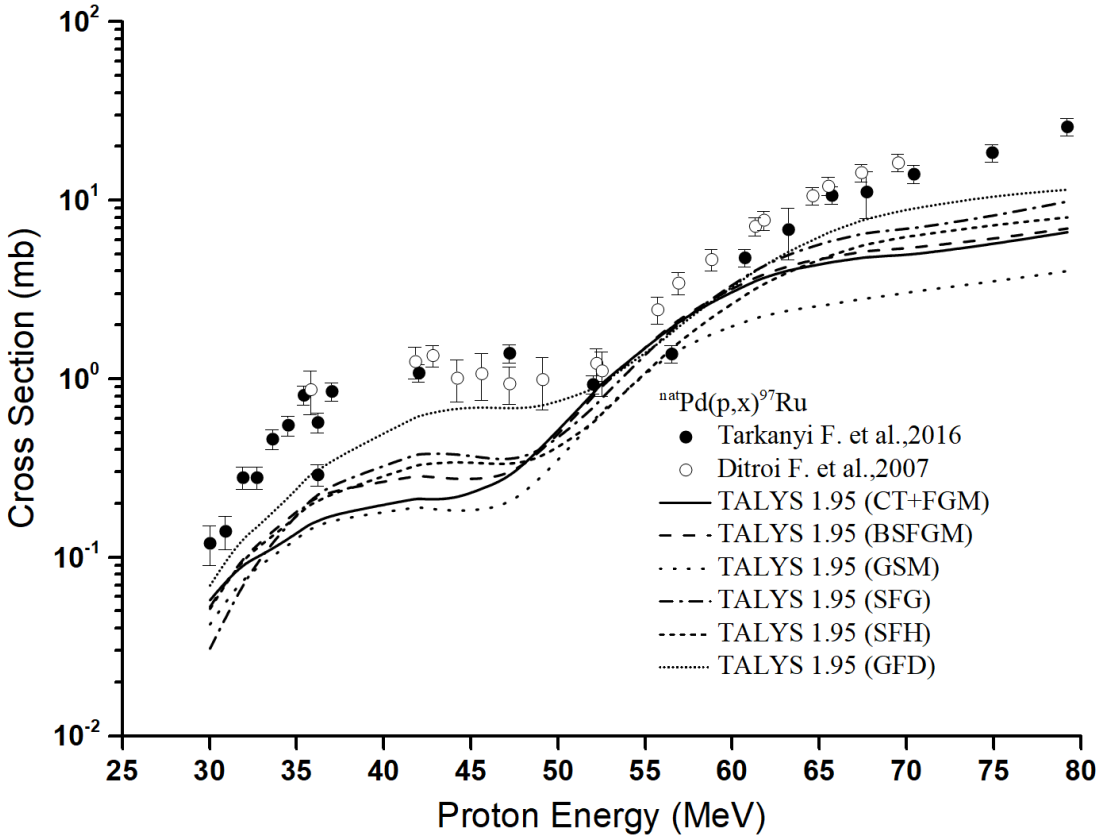

Figure 1. Graphical representation comparing level density model calculations with the Ref [34,35] for the ^{nat}Pd(p,x)^{97}Ru reaction

For the ^{nat}Pd(p,x)^{100}Pd reaction in almost 25-80 MeV proton incident energy range all computation results, and available experimental data [34-37] have been shown together in Figure 2. Among the experimental data given in Figure 2, the data of Tarkanyi et al. [34] are seen as clustered between the energy range of almost 25-40 MeV. Also, it is observable that data taken from both Nguyen et al. [36], and Khandaker et al. [37] are located below the other experimental data in adding to the calculation results. After this energy range, available experimental data of Tarkanyi et al. [34], and Ditrio et al. [35] are shown as in agreement with each other. In all the energy ranges examined for this reaction, all level density model calculations are obtained to show general geometrically compatibility with the experimental values. After 60 MeV energy reaction cross-section data from GSM, GFD, and SFG models are obtained lower than the experimental values.

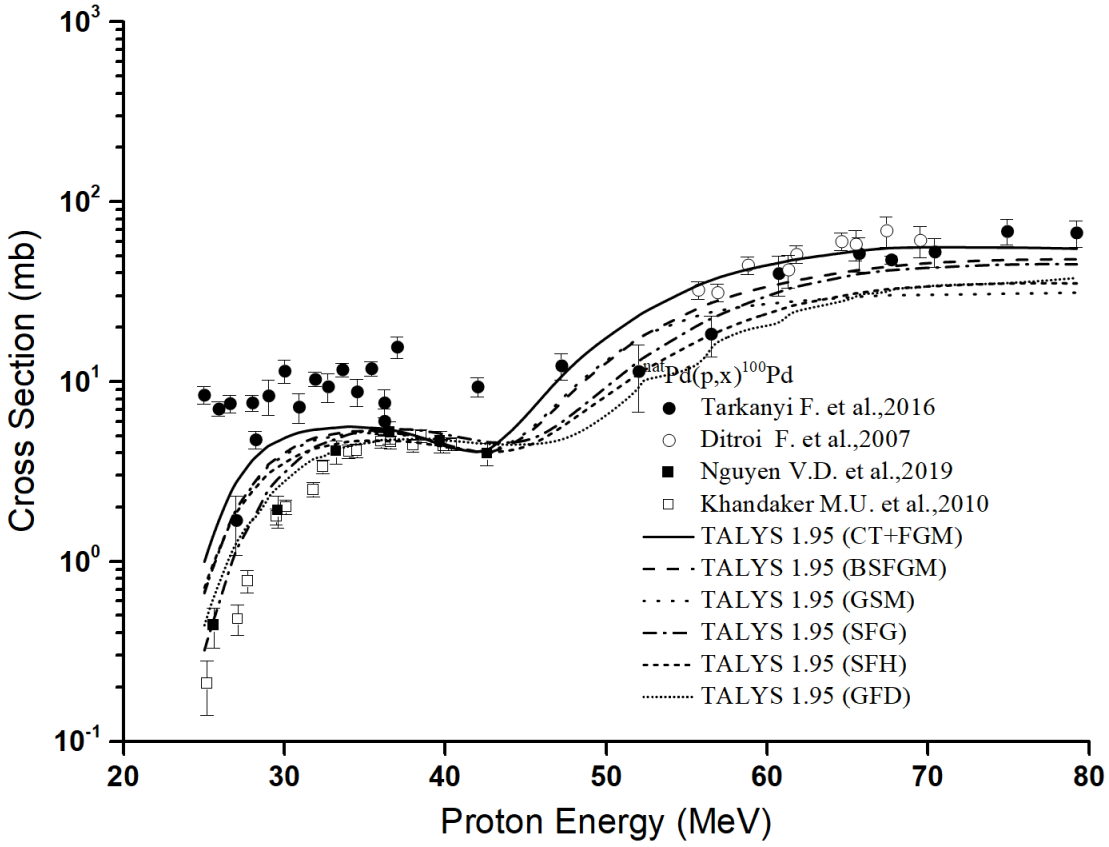

Figure 2. Graphical representation comparing level density model calculations with the Ref [34-37] for the $^{nat}Pd(p,x)^{100}Pd$ reaction

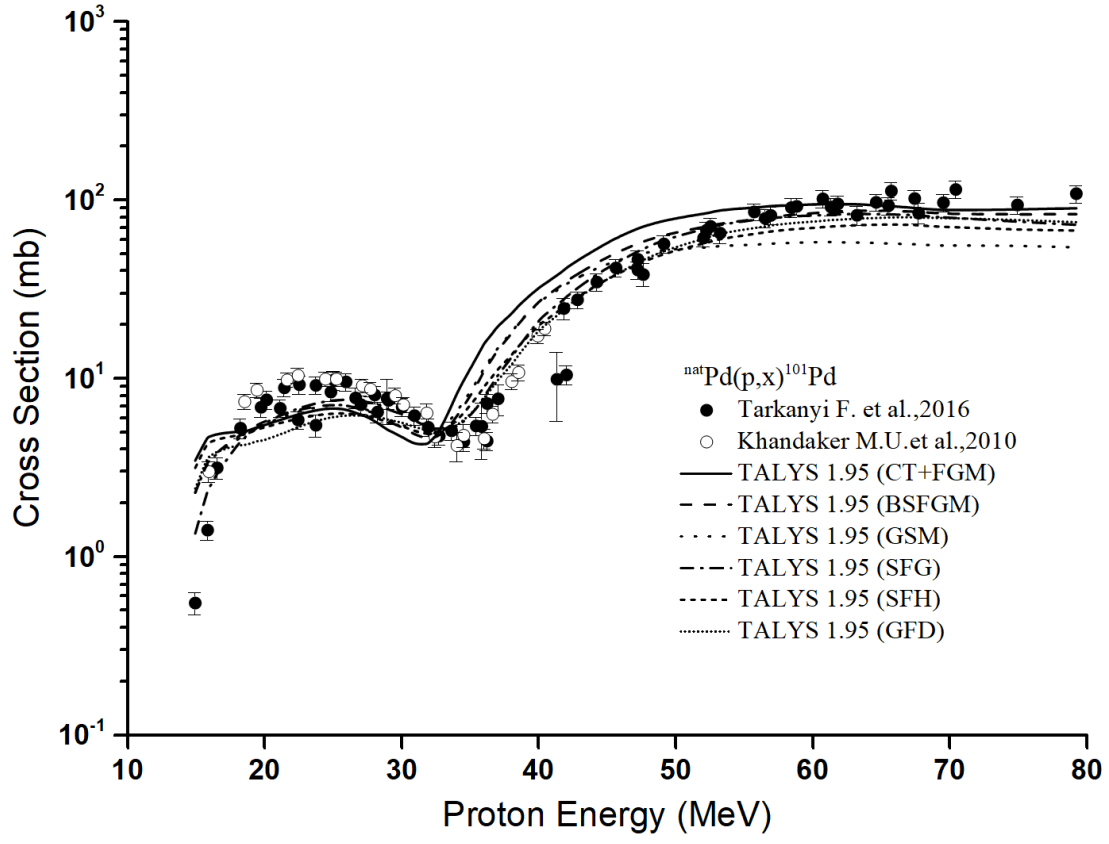

Figure 3. Graphical representation comparing level density model calculations with the Ref [34,37] for the $^{nat}Pd(p,x)^{101}Pd$ reaction

In Figure 3, available experimental data [34,37], and calculation results for $^{nat}Pd(p,x)^{101}Pd$ reaction are plotted together. The representation of the experimental data, and calculation results exhibit a similar geometrical distribution to the $^{nat}Pd(p,x)^{100}Pd$ reaction, which is given in Figure 2. However, for the $^{nat}Pd(p,x)^{101}Pd$ calculation, cross-section results obtained the use of utilizing level density models have been obtained close to each other with respect to the outputs given in Figure 2. On the other hand, if closer attention is given to the energy region greater than 50 MeV, it is seen that the results form GSM are obtained as slightly lower than the experimental values. Apart from all these, after around 35 MeV to around 55 MeV energy region, it is also seen that the results from CT+FGM, and FGM are obtained slightly higher than the experimental values.

$^{nat}Pd(p,x)^{103}Ag$ reaction is one other investigated reaction in this study. The graphical representation comparing level density model calculations with the experimental measurements [34, 37-38] for these reactions are given in Figure 4. Unlike the previously given three reaction results shown in Figures 1-3, outcomes for $^{nat}Pd(p,x)^{103}Ag$ reaction do not exhibit a similar manner to provide an increase in the cross-section data as the energy of the incident particle increases. Even this, in all examined energy ranges for this reaction, all model results, except for GSM, show similar, and compatible distribution with the general trend of the experimental data. In GSM detail, it can be interpreted that, the outcomes via utilizing this model have achieved lower than both the experimental data, and the results of other models.

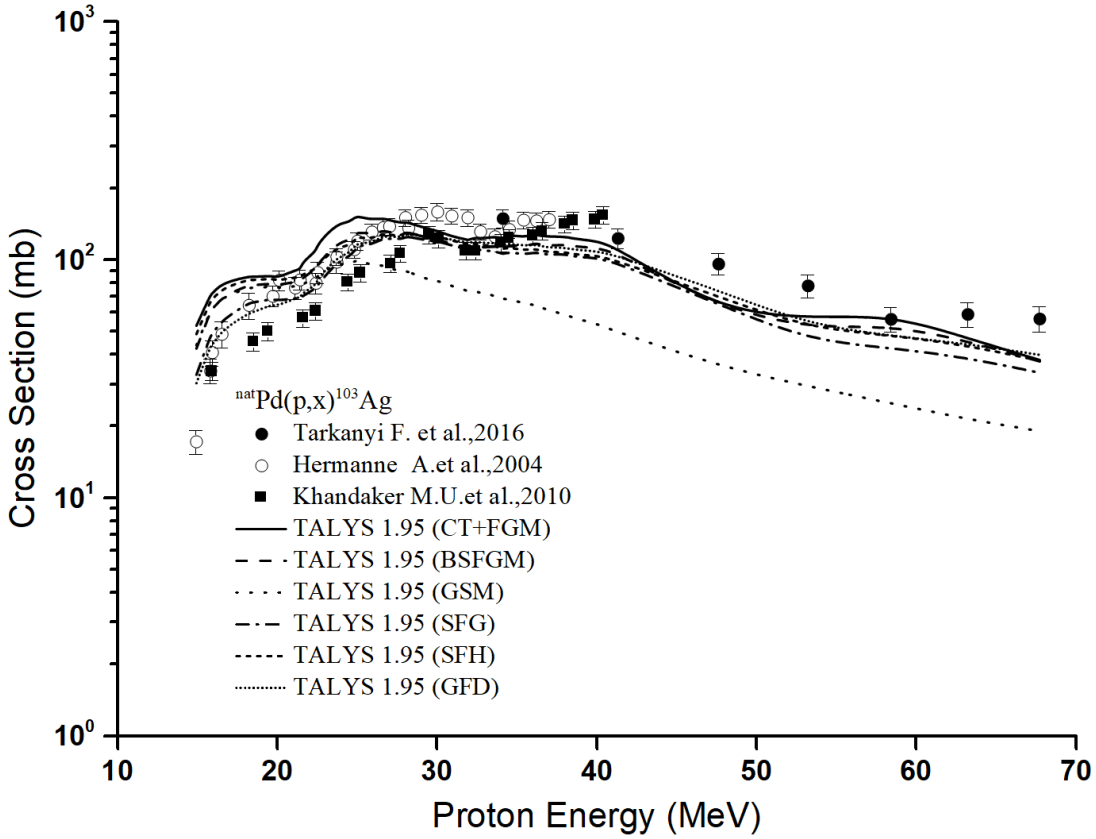

Figure 4. Graphical representation comparing level density model calculations with the Ref [34, 37-38] for the $^{nat}Pd(p,x)^{103}Ag$ reaction

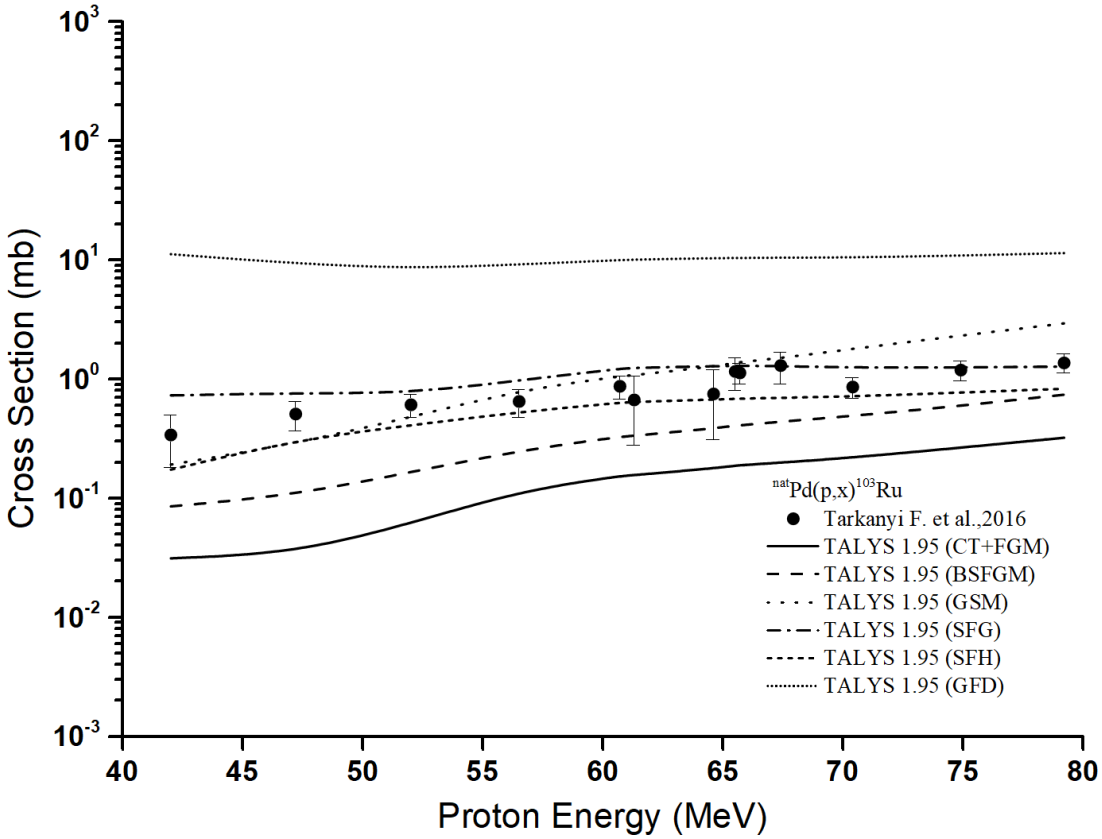

Figure 5. Graphical representation comparing level density model calculations with the Ref [34] for the $^{nat}Pd(p,x)^{103}Ru$ reaction

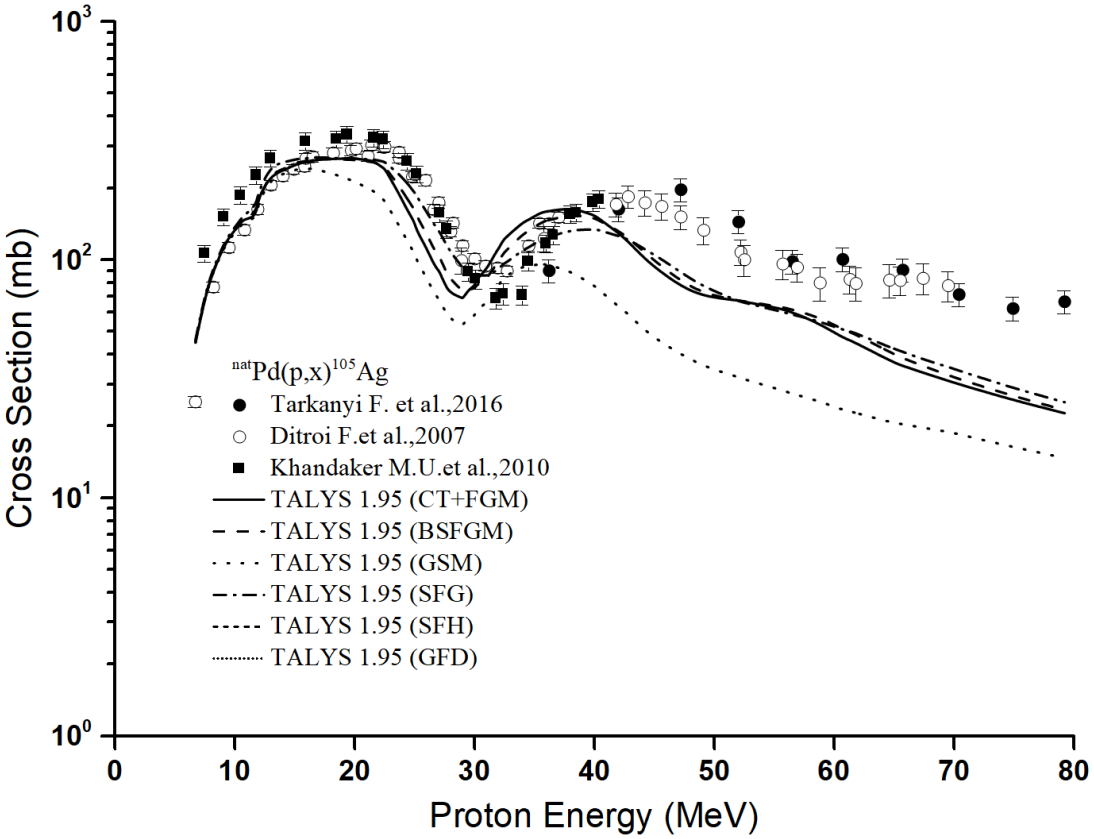

Figure 6. Graphical representation comparing level density model calculations with the Ref [34-35,37] for the $^{nat}Pd(p,x)^{105}Ag$ reaction

For the $^{nat}Pd(p,x)^{103}Pd$ reaction, in which the available experimental data [34] are in the range of almost 40-80 MeV, Figure 5 is given to compare the calculation results, and experimental data. Among all examined reactions in this study, $^{nat}Pd(p,x)^{100}Pd$ reaction is the one where the difference between the model calculation results, in addition to the experimental data, can be seen effortlessly. Between the calculation results obtained, values higher than the experimental data are obtained via utilizing GSM, while values lower than the experimental data are obtained using CT+FGM.

In Figure 6, the cross-section data of the $^{nat}Pd(p,x)^{105}Ag$ reaction in the energy range of almost 5-80 MeV incident proton particle are compared with the experimental data of Tarkanyi et al. [34], Ditrio et al. [35], and Khandaker et al. [37]. When the graphical representation is examined it is seen that all models, except for the GSM, are compatible with the experimental values up to 40 MeV. After 40 MeV, the results obtained with the models are compatible with each other but lower than the experimental values.

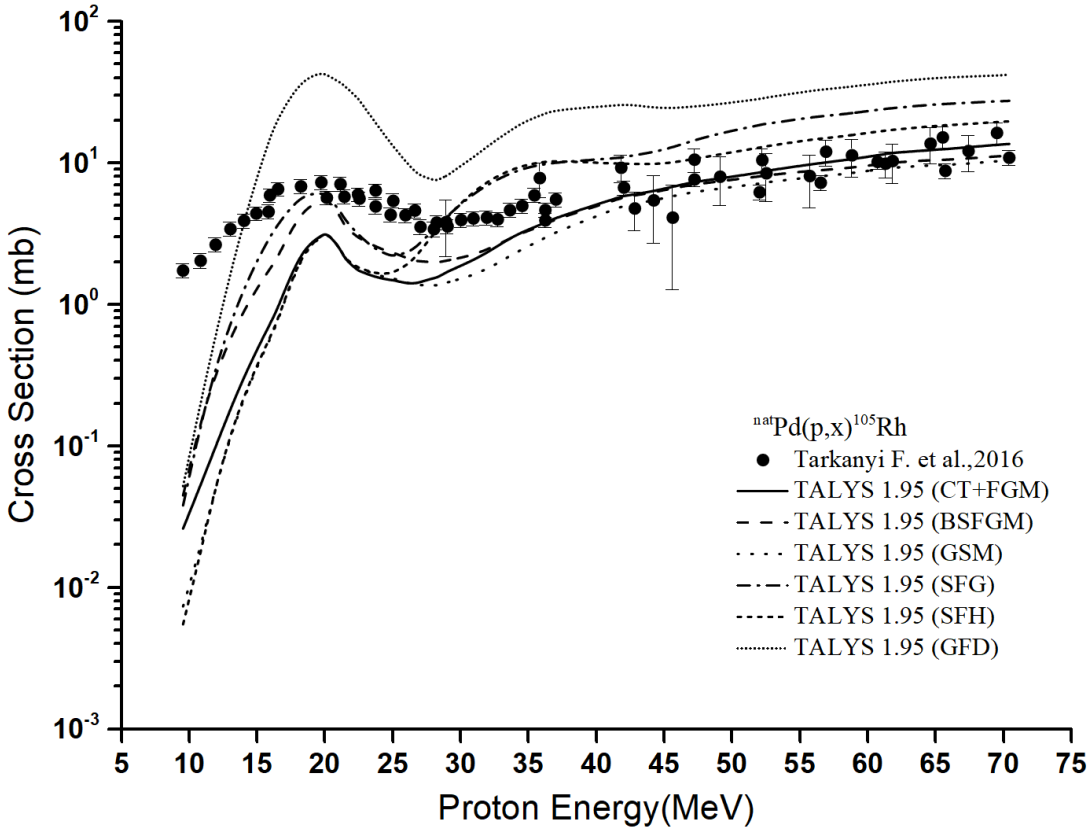

Figure 7. Graphical representation comparing level density model calculations with the Ref [34] for the $^{nat}Pd(p,x)^{105}Rh$ reaction

The comparison of the cross-sectional data for the $^{nat}Pd(p,x)^{105}Rh$ reaction with the experimental data of Tarkanyi et al. [34] are shown in Figure 7. Up to almost18 MeV incident particle energy, it is observed that the models deliver lower calculation results than the experimental data. After almost 40 MeV energy, it is observed that GFD, and SFG models give results that are higher than the experimental data, while the other model results are in agree with the experimental measurements taken for this reaction.

4. Conclusion

In this study, cross-section calculations for $^{nat}Pd(p,x)^{97}Ru$, $^{nat}Pd(p,x)^{100}Pd$, $^{nat}Pd(p,x)^{101}Pd$, $^{nat}Pd(p,x)^{103}Ag$, $^{nat}Pd(p,x)^{103}Ru$, $^{nat}Pd(p,x)^{105}Ag$, and $^{nat}Pd(p,x)^{105}Rh$ reactions have been calculated using macroscopic, and microscopic level density models which are available in the TALYS 1.95 code. Upon the completing of the cross-section calculations, obtained results are compared with the available experimental data taken from the literature, and all output are summarized below.

For some of the investigated reactions in this study, calculation results obtained by using some particular level density models have been given higher values than the experimental measurements while some particular level density models generate lower values than the experimental data. Accordingly, it is possible to interpret the outcomes of all investigated reactions in this study by taking them into account as a whole. The utilization of level density models clearly affects the results of cross-section calculations.

In cases where it may be impossible to perform a desired experimental measurement, obtaining the cross-section values for a specific reaction under specific conditions, and using the desired theoretical parameter set by using confirmed computer-aided calculation tools, like TALYS, which is the one employed in this study, could be more beneficial, and lead researchers to perform further studies concerning the model, and parameter development in addition to the more detailed comprehension of the nature of a nuclear reaction mechanism.

Authorship contribution statement

Ö. Y. TOYKAN CIFTLIKLI: Conceptualization, Methodology, Software, Investigation, Data Curation, Original Draft Writing, Review and Editing, Visualization; A. KAPLAN: Supervision/Observation/Advice

Declaration of competing interest

The authors declare that they have no known competing financial interests or personal relationships that could have appeared to influence the work reported in this paper.

Acknowledgment

There is no acknowledgment.

Ethics Committee Approval and/or Informed Consent Information

As the authors of this study, we declare that we do not have any ethics committee approval and/or informed consent statement.

References

[1] C. G. Anderson, L. C. Newman and G. K. Roset, “Platinum Group Metal Bullion Production and Refining”, *Mineral Processing Plant Design*, Practice and Control Proceedings, Eds. A Mular, D. Halbe, and D. Barrett, Vancouver, British Columbia, October 2002, 1760.

[2] R. J. Newman and F. J. Smith. “Platinum metals from nuclear fission”, *Platinum Metals Review*, 14, 88-92, 1970.

[3] Z. Kolarik and V. R. Edouard, “Potential applications of fission platinoids in industry”, *Platinum Metals Review*, 49, 79-90, 2005.

[4] J. R. De Laeter, J. K. Böhlke, P. De Bievre, H. Hidaka, H. S. Peiser, K. J. R. Rosman and P. D. P. Taylor, “Atomic weights of the elements: review 2000, *Pure and Applied Chemistry*, 75, 683-800, 2003.

[5] B. R. Martin, Nuclear and Particle Physics Department of Physics and Astronomy University College London John Wiley and Sons, Ltd. England 23, 129-136, 2006.

[6] S. G. Mashnik, CODE CEM95, Joint Institute for Nuclear Research. Dubna, Moskow, Russia, 1995.

[7] M. Herman, R. Capote, M. Sin, A. Trkov, B. V. Carlson, P. Oblozinsky, C. M. Mattoon, H. Wienkey, S. Hoblit, Young–Sik Cho, G. P. A. Nobre, V. Plujko, and V. Zerkin, EMPIRE-3.2 Malta, Modular System for Nuclear Reaction Calculations and Nuclear Data Evaluation, 2013.

[8] S. Agostinelli, J. Allison, K. Amako, J. Apostolakis, H. Araujo, P. Arce, M. Asai, D. Axen, S. Banerjee, G. Barrand, F. Behner, L. Bellagamba, J. Boudreau, L. Broglia, A. Brunengo, H. Burkhardt, S. Chauvie, J. Chuma, R. Chytracek, G. Cooperman, G. Cosmo, P. Degtyarenko, A. Dell'Acqua, G. Depaola, D. Dietrich, R. Enami, A. Feliciello, C. Ferguson, H. Fesefeldt, G. Folger, F. Foppiano, A. Forti, S. Garelli, S. Giani, R. Giannitrapani, D. Gibin, J. J. Gómez Cadenas, I. González, G. Gracia Abril, G. Greeniaus, W. Greiner, V. Grichine, A. Grossheim, S. Guatelli, P. Gumplinger, R. Hamatsu, K. Hashimoto, H. Hasui, A. Heikkinen, A. Howard, V. Ivanchenko, A. Johnson, F. W. Jones, J. Kallenbach, N. Kanaya, M. Kawabata, Y. Kawabata, M. Kawaguti, S. Kelner, P. Kent, A. Kimura, T. Kodama, R. Kokoulin, M. Kossov, H. Kurashige, E. Lamanna, T. Lampén, V. Lara, V. Lefebure, F. Lei, M. Liendl, W. Lockman, F. Longo, S. Magni, M. Maire, E. Medernach, K. Minamimoto, P. Mora de Freitas, Y. Morita, K. Murakami, M. Nagamatu, R. Nartallo, P. Nieminen, T. Nishimura, K. Ohtsubo, M. Okamura, S. O'Neale, Y. Oohata, K. Paech, J. Perl, A. Pfeiffer, M. G. Pia, F. Ranjard, A. Rybin, S. Sadilov, E. Di Salvo, G. Santin, T. Sasaki, N. Savvas, Y. Sawada, S. Scherer, S. Sei, V. Sirotenko, D. Smith, N. Starkov, H. Stoecker, J. Sulkimo, M. Takahata, S. Tanaka, E. Tcherniaev, E. Safai Tehrani, M. Tropeano, P. Truscott, H. Uno, L. Urban, P. Urban, M. Verderi, A. Walkden, W. Wander, H. Weber, J. P. Wellisch, T. Wenaus, D. C. Williams, D. Wright, T. Yamada, H. Yoshida, and D. Zschiesche, "Geant4-A simulation toolkit", *Nuclear Instruments and Methods in Physics Research Section A: Accelerators, Spectrometers, Detectors and Associated Equipment*, 506(3), 250-303, 2003.

[9] C. H. M. Broeders, Yu. A. Korovin, A. Yu. Konobeyev, Yu. A. Korovin, M. Blann, Yu. A. Korovin, and V. P. Lunev, "ALICE/ASH - Pre-compound and evaporation model code system for calculation of excitation functions, energy and angular distributions of emitted particles in nuclear reactions at intermediate energies", Forschungszentrum Karlsruhe in der Helmholtz-Gemeinschaft Wissenschaftliche Berichte, 2006.

[10] R. Capote, V. Osorio, R. Lopez, E. Herrera, and M. Piris, "Analysis of Experimental Data on Neutron-Induced Reactions and development of code Pcross for the Calculation of Differential Pre-equilibrium Emission Spectra with Modelling of Level Density Function", Final Report on Research Contract 5472/RB, INDC (CUB)-004, Distr, L., 1991.

[11] A. Koning, S. Hilaire, and S. Goriely, "TALYS-1.95, A nuclear reaction program", NRG-1755 ZG Petten, The Netherlands, 2019.

[12] M. Şekerci, H. Özdoğan and A. Kaplan, "Astrophysical s-factor calculations under the effects of gamma-ray strength functions for some alpha capture reactions", *Moscow University Physics Bulletin*, 75, 585–589, 2020.

[13] M. Şekerci, H. Özdoğan and A. Kaplan, "Effects of combining some theoretical models in the cross-section calculations of some alpha-induced reactions for ^{nat}Sb", *Applied Radiation and Isotopes*, 186, 110255, 2022.

[14] M. Şekerci, H. Özdoğan and A. Kaplan, "Effects of deuteron optical models on the cross-section calculations of deuteron induced reactions on natural germanium", *Applied Radiation and Isotopes*, 176, 109875, 2021.

[15] H. Özdoğan, M. Şekerci and A. Kaplan, "Production cross–section and reaction yield calculations for $^{123\text{-}126}$I isotopes on ^{123}Sb(α,xn) reactions", *Kuwait Journal of Science*, 48(2), 1-11, 2021.

[16] H. Özdoğan, M. Şekerci and A. Kaplan, "An investigation on the effects of some theoretical models in the cross-section calculations of ^{50,52,53,54}Cr(α,x) reactions", *Physics of Atomic Nuclei*, 83, 820-827, 2020.

[17] M. Şekerci, H. Özdoğan and A. Kaplan, "An investigation of effects of level density models and gamma-ray strength functions on cross-section calculations for the production of ^{90}Y, ^{153}Sm, ^{169}Er, ^{177}Lu and ^{186}Re therapeutic radioisotopes via (n,γ) reactions", *Radiochimica Acta*, 108(1), 11-17, 2020.

[18] H. Özdoğan, M. Şekerci and A. Kaplan, "Investigation of gamma strength functions and level density models effects on photon-induced reaction cross–section calculations for the fusion structural materials $^{46, 50}$Ti, ^{51}V, ^{58}Ni and ^{63}Cu", *Applied Radiation and Isotopes*, 143, 6-10, 2019.

[19] M. Şekerci, H. Özdoğan and A. Kaplan, "Level density model effects on the production cross-section calculations of some medical isotopes via (α, xn) reactions where x = 1–3", *Modern Physics Letters*, 35(24), 2050202, 2020.

[20] H. Özdoğan, M. Şekerci and A. Kaplan, "Photo-neutron cross-section calculations of ^{54,56}Fe, ^{90,91,92,94}Zr, ^{93}Nb and ^{107}Ag Isotopes with newly obtained giant dipole resonance parameters", *Applied Radiation and Isotopes*,165, 109356, 2020.

[21] H. Özdoğan, M. Şekerci and A. Kaplan, "S-factor analysis of proton capture reactions on ^{112,114,116,119}Sn and ^{113,115}In isotopes", *Physics of Atomic Nuclei*, 82, 324-329, 2019.

[22] N. Otuka, E. Dupont, V. Semkova, B. Pritychenko, A. I. Blokhin, M. Aikawa, S. Babykina, M. Bossant, G. Chen, S. Dunaeva, R. A. Forrest, T. Fukahori, N. Furutachi, S. Ganesan, Z. Ge, O. O. Gritzay, M. Herman, S. Hlavač, K. Katō, B. Lalremruata, Y. O. Lee, A. Makinaga, K. Matsumoto, M. Mikhaylyukova, G. Pikulina, V. G. Pronyaev, A. Saxena, O. Schwerer, S. P. Simakov, N. Soppera, R. Suzuki, S. Takács, X. Tao, S. Taova, F. Tárkányi, V. V. Varlamov, J. Wang, S. C. Yang, V. Zerkin and Y. Zhuang, "Towards a more complete and accurate experimental nuclear reaction data library (EXFOR): International collaboration between nuclear reaction data centres (NRDC)", *Nuclear Data Sheets*, 120, 272-276, 2014.

[23] V. V. Zerkin and B. Pritychenko, "The experimental nuclear reaction data (EXFOR): extended computer database and web retrieval system", *Nuclear Instruments and Methods in Physics Research Section A: Accelerators, Spectrometers, Detectors and Associated Equipment*, 888, 31-43, 2018.

[24] E. Fermi, "Zur Quantelung des idealen einatomigen Gases", *Zeitschrift für Physik*, 36, 902-912, 1926.

[25] A. Gilbert and A. G. W. Cameron, "A composite nuclear-level density formula with shell corrections", Canadian Journal of Physics, 43(8), 1446-1496, 1965.

[26] A. V. Ignatyuk, K. K. Istekov, G. N. Smirenkin, "Role of the collective effects in a systematics of nuclear level density", *Soviet Journal of Nuclear Physics*, 29, 450, 1979.

[27] H. Baba, "A shell-model nuclear level density", Nuclear Physics, 159, 625-641, 1970

[28] W. Dilg, W. Schantl, H. Vonach and M. Uhl, "Level density parameters for the back-shifted fermi gas model in the mass range $40 < A < 250$", Nuclear Physics A, 217(2), 269-298, 1973.

[29] A. V. Ignatyuk, G. N. Smirenkin and A. S. Tishin, "Phenomenological description of energy dependence of the level density parameter", *Yadernaya Fizika*, 21, 485–490, 1975.

[30] A. J. Koning, S. Hilaire and S. Goriely, "Global and local level density models", *Nuclear Physics A*, 810(1-4), 13-76, 2008.

[31] S. Goriely, S. Hilaire, and A. J. Koning, "Improved microscopic nuclear level densities within the Hartree-Fock-Bogoliubov plus combinatorial method", *Physical Review C*, 78, 064307, 2008.

[32] S. Hilaire, and S. Goriely, "Global microscopic nuclear level densities within the HFB plus combinatorial method for practical applications", *Nuclear Physics A*, 779, 63-81, 2006.

[33] S. Hilaire, M. Girod, S. Goriely, and A. J. Koning, "Temperature-dependent combinatorial level densities with the D1M Gogny force", *Physical Review C*, 86, 064317, 2012.

[34] F. Tárkányi, F. Ditrói, S. Takács, J. Csikai, A. Hermanne, M. S. Uddin and, M. Baba, "Activation cross sections of proton induced nuclear reactions on palladium up to 80 MeV", *Applied Radiation and Isotopes*, 114, 128-144, 2016.

[35] F. Ditroi, F. Tarkanyi, S. Takacs, I. Mahunka, J. Csikai, A. Hermanne, M. S. Uddin, M. Hagiwara, M. Baba, T. Ido, Yu. Shubin and A.I. Dityuk, "Measurement of activation cross sections of the proton induced nuclear reactions on palladium", *Journal of Radioanalytical and Nuclear Chemistry*, 272, 231-235, 2007.

[36] V. D. Nguyen, T. L. Nguyen, T. X. Nguyen, T. H. Nguyen, G. N. Kim and K. Kim, "Measurement of cross sections for the formation of ^{100g}Rh in ^{nat}Pd(p,x)^{100m,g}Rh reactions up to 42.61 MeV", *Journal of Radioanalytical and Nuclear Chemistry*, 321, 117-123, 2019.

[37] M. U. Khandaker, K. S. Kim, G. N. Kim and N. Otuka, "Cyclotron production of the ^{105,106m}Ag, ^{100,101}Pd, ^{100,101m,105}Rh radionuclides by ^{nat}Pd(p,x) nuclear processes", *Nuclear Instruments and Methods in Physics Research Section B: Beam Interactions with Materials and Atoms*, 268, 2303-2311, 2010.

[38] A. Hermanne, S. Takács, F. Tárkányi, and R. Bolbos, "Cross section measurements of proton and deuteron induced formation of ^{103}Ag in natural palladium", *Radiochimica Acta*, 92(4-6), 215-218, 2004.

Süleyman Demirel Üniversitesi Fen Edebiyat Fakültesi Fen Dergisi https://dergipark.org.tr/sdufeffd
Süleyman Demirel University Faculty of Arts and Sciences Journal of Science e-ISSN: 1306-7575
Research Article, 2024, 19(1): 40-52, DOI: 10.29233/sdufeffd.1383363

Prediction of The Ultraviolet Protection Provided by Woven Fabric Construction Using Fuzzy Logic

Murat Kodaloğlu[1], Feyza Akarslan Kodaloğlu[2]

[1]Occupational Health and Safety Program, Vocational School of Technical Sciences, Isparta University of Applied Sciences, 32200, Isparta-TÜRKİYE
https://orcid.org/0000-0001-6644-8068
[2]Textile Enginering Department, Engineering Faculty, Suleyman Demirel University, 32200, Isparta-TÜRKİYE
https://orcid.org/0000-0002-7855-8616
*corresponding author: muratkodaloglul@isparta.edu.tr

(Received: 30.10.2023, Accepted: 06.03.2024, Published: 27.05.2024)

Abstract: The negative impact of UltraViolet (UV) radiation on human health is an issue that is gaining importance gradually, and the demand for the production of fabrics with UV protective properties is increasing progressively. Textile materials provide simple and useful protection against UV radiation. The degree of this protection is determined by the Ultraviolet Protection Factor (UPF).

The effects of the yarn fineness and the woven fabric tightness, both used in the main representative woven fabric weave-types/constructions (plain, satin, twill), on UPF and bifunctional UV protection were examined and are presented in this article.

A prediction model determined by fuzzy logic programming was derived to describe these effects of the aforementioned parameters. The results show very good agreement between experimental and predicted values.

Keywords: Human health, Ultraviolet protection, Satin, Twill, Plain, Fuzzy logic

1. Introduction

Due to the climate change that is experienced today and is felt very closely, taking precautions against the negative effects of the sun has become a necessity. To ensure this, exposure to too much sunlight should be avoided, protective equipment should be used or clothing that will protect against the harmful effects of sunlight should be preferred.

Dubrovski *et al* observed that the UPF value of woven fabrics heavily relies on various construction parameters [1-2]. Stankovic *et al* in their research, delved into the impact of yarn twist on UPF in cotton woven fabric, alongside the influence of fabric surface properties [3]. Gies *et al* noted that UV light penetrates through the fabric's open areas, and numerous studies on different construction parameters have highlighted their significant effect on UV protection [4]. Among these parameters, Dimitrovski *et al* focused on fabric cover factor [6-7], while Gabrijelčič *et al* investigated fabric open porosity, mass, and thickness, among others. Dubrovski and Golob found that varying weave types (such as twill and satin) exhibit higher UPF in gray-colored 100% cotton woven fabrics of the same yarn fineness, with plain weave showing a lower UPF due to

its increased thread passes. In their analysis, satin ranked highest in UPF, followed by twill, and then plain weave [8].

1.2. Ultraviolet

1.2.1. Electromagnetic waves

In modern physics, light or electromagnetic wave is theoretically defined in two complementary forms: a wave in an electromagnetic field and a flow of massless particles called photons [9-10].

Electromagnetic waves are a type of energy that propagates very quickly in space (vacuum) [11]. Numerous physical events we experience on a daily basis, such as sunlight rising, microwaves cooking our meals, and also operating radios and televisions due to the creation of an electromagnetic field, are situations that make us feel the presence of electromagnetic waves [12]. X-rays, ultraviolet rays, microwaves and radio waves can be counted among the main electromagnetic waves [13].

Radio waves, television waves and microwaves are types of electromagnetic waves. They are separated from each other only by their wavelengths. In the electromagnetic spectrum, waves range from very long radio waves the size of buildings to shorter gamma waves the size of the nucleus of an atom.

1.2.3. Ultraviolet light

Ultraviolet (UV) waves have shorter wavelengths than visible light. These wavelengths cannot be seen by the human eye. However, it has been noticed that some species of wasps can see these waves. Scientists have divided the ultraviolet part of the spectrum into three; near UV, far UV and very far UV.

This distinction is made according to the energy of UV radiation. It is expressed in terms of wavelength energy of UV light. Near UV light is close to visible light, very far UV light is close to X-rays, and far UV is in between. The sun emits rays of all wavelengths in the electromagnetic spectrum. Some UV waves coming from the sun pass through the earth's atmosphere, but they are retained by some gases such as the ozone layer. Some days more UV radiation reaches the earth. Scientists have developed the UV index to help protect people from the harmful effects of UV radiation [14].

Ultraviolet rays also consist of groups with different wavelengths. This classification can also be applied by physicists as near UV (320-380 nm), mid-UV (200-320 nm) and vacuum UV (10-200 nm) [14]. UV-A Ray wavelength is between 320-400 nm.

Among UV rays, which rays have the longest wavelength and least energy. Sun-derived UV-A rays are not retained by the atmosphere and can pass through glass. It can penetrate into the human inner skin known as the dermis. Therefore, it causes premature aging, wrinkles on the skin, and the progression of skin cancer. It is generally used in lighting systems in industry [15].

UV-B rays have a wavelength between 280-320 nm and located in the middle of the UV band in terms of both energy and wavelength. It is approximately 1000 times stronger than UV-A [15]. Biologically harmful UV-B radiation reaches the earth's surface depending on the concentration of stratospheric ozone. It is not just stratospheric ozone that absorbs UV-B and prevents it from reaching the earth's surface. Most of the UV rays are absorbed by clouds. Atmospheric pollution can affect UV exposure locally and globally. The most important effect of the UV-B radiation is that it weakens people's

immune system. Another important effect is that it causes temporary blindness in humans, damage to the cornea, and cataracts in older ages. Another harmful effect of UV-B rays on humans is skin cancer. If exposed to long-term UV-B rays, deterioration of skin cells may occur, tumor formation may occur at the age of 40, and advanced cancer may occur at the age of 50 . It is used in lighting systems and solarium lamps in industry [15-16].

UV-C ray: These are the rays with the shortest wavelength and the highest energy in the C band of UV, with a wavelength between 200-280 nm. It causes cancer when it comes into contact with skin or eyes. Protector you should not be exposed to UV-C radiation in any way without taking precautions [17-18]. UV-C rays originating from the sun are filtered by the ozone layer or retained by gases in the atmosphere. Therefore, it is produced using electrical energy only as a result of electronic industrial processes. Since it loses its energy as soon as it touches any surface, it has been used especially in surface modifications recently [19-20].

In this article, a predictive model was derived with fuzzy logic programming in order to investigate the effects of woven fabric construction on the ultraviolet protection factor.

2. Material and Method

The fuzzy logic tables created in this study were described using the MATLAB program and the resulting data were examined. The Mamdani model, which has two inputs and one output, was established with the fuzzy logic module of the MATLAB program. In this model, the method of obtaining results with the center of gravity method is taken as basis[21].

In the study, the type of membership functions used in the input sets is the Generalized Bell Membership Function (GBellMF) method, thus the trapezoidal shape, which is a geometric shape, is obtained. In this way, approximate values are obtained within the framework of fuzzy logic rules. The reason for using the GBellMF method is that trapezoidal fuzzy numbers have a special shape compared to triangular fuzzy numbers are more understandable with verbal variables [21]. The fuzzy logic rule is presented in Figure 1.

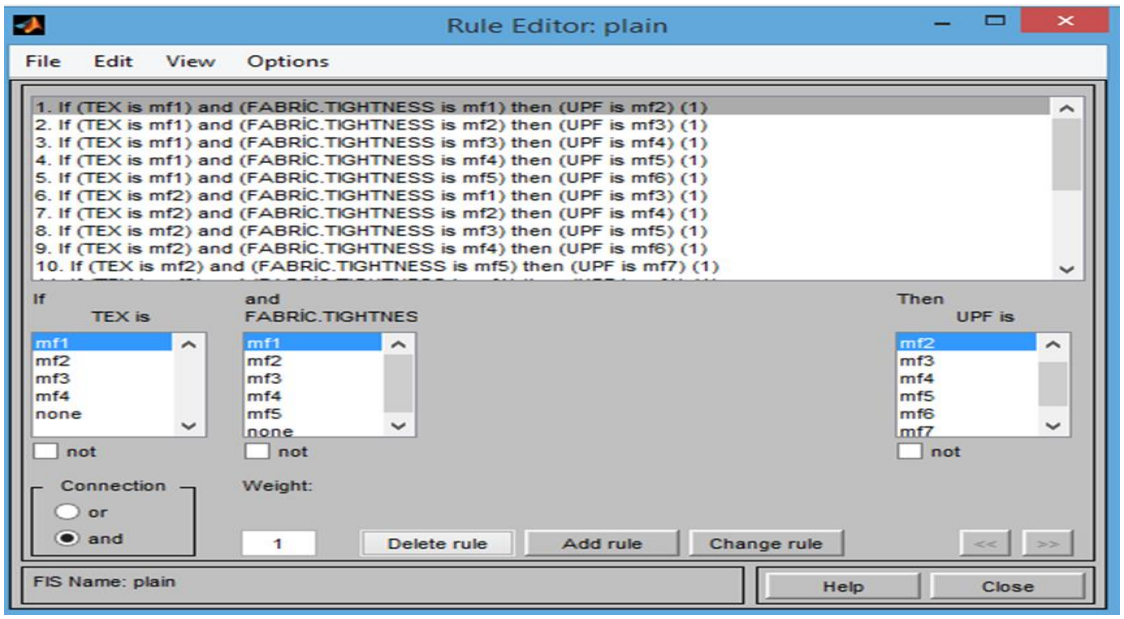

Figure 1. The Fuzzy Logic Rule

Plain, twill and satin weaves woven fabric constructions made of 100% cotton Open End (OE) yarns were used to analyze the effect of woven fabric constructions on the UPF. Weaving samples varied according to yarn fineness, weave type and fabric tightness. Three woven fabric samples were used to analyze the effect of woven fabric constructions on the UPF and define a prediction model for UPF, similar to the previous step, with variation of structural parameters. When the results of UPF measurements of woven fabrics with different structures were analyzed, it was revealed that samples with different woven constructions keeping constant the fabric tightness and yarn fineness offered different level of UV protection.

The combination of various structural features (weave type, fabric tightness, etc.), thickness, weight, porosity of fabrics have a great impact on the transmission of UV radiation through fabrics. Loosely textured thin fabrics provide less protection than tighter textured fabrics. The constructional parameters of the fabrics are presented in Table 1.

Table 1. Constructional Parameters of Woven Samples

Yarn fineness, tex	Type of weave	Cover factor %	Fabric Tightness %
10	Plain	60	55
10	Twill	70	55
10	Satin	80	55
20	Plain	62	65
20	Twill	73	65
20	Satin	81	65
30	Plain	63	75
30	Twill	75	75
30	Satin	82	75
40	Plain	65	80
40	Twill	76	80
40	Satin	84	80
50	Plain	68	85
50	Twill	79	85
50	Satin	87	85

Jasco V-570 spectrometer characteristics are presented in Table 2. Their behaviour under the UV radiation exposure was evaluated.

Table 2. The Characteristics of Jasco V-570 Spectrometer

Wavelength rang	190 – 2500 nm
Measurement	0.3 nm
Type of the lamp	Tungsten – Deuterium
Type of the detector	PbS Photocell – PMT

3. Results

Fuzzy logic prediction model was used for UPF of woven fabrics. To assist woven fabric makers by developing woven fabrics with optimum UPF, the prediction model for UPF has been developed through fuzzy logic programming on the basis of woven fabric constructions parameters. The method of modeling presented in this article clearly presents the dependence between UPF and the parameters characterizing the structure of the textile product.

3.1. Satin fabric constructions fuzzy prediction

For satin fabric, our entry membership functions, the yarn fineness, was chosen to be five, and the fabric tightness was chosen to be five feet. Our output function, UPF, is determined in the sixteen foot range. It was created with a hundred and twenty rule base in order to understand the effect of the relationship between the determined membership functions on the result. The relationship between the yarn fineness and fabric tightness of the satin fabric constructions and UPF is presented in Figure 2.

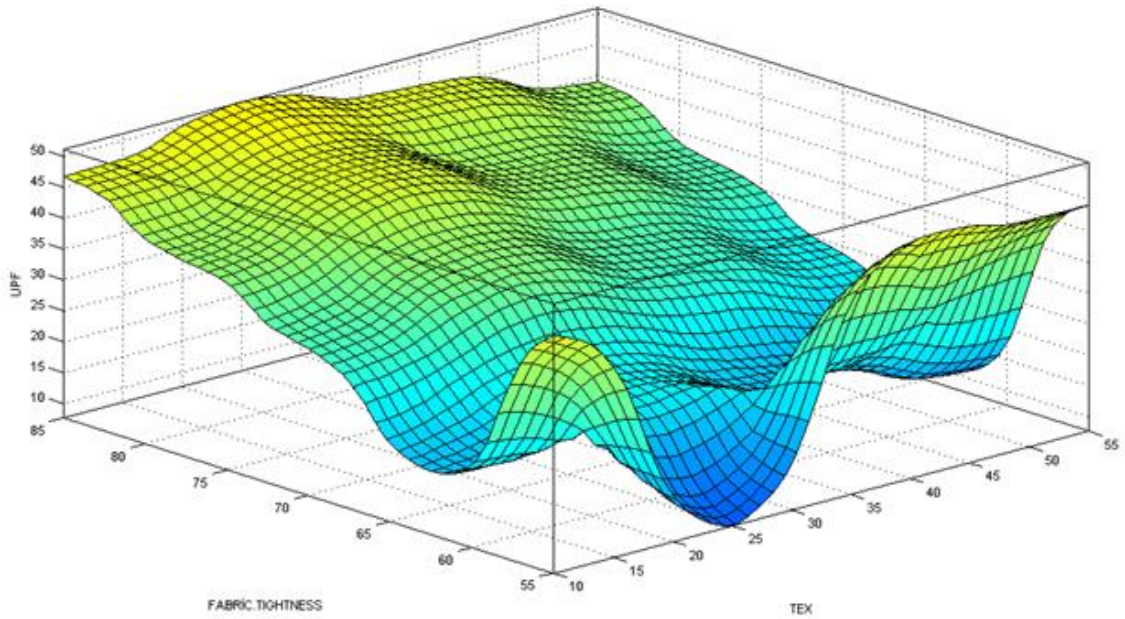

Figure 2. The Relationship Between Yarn Fineness and Fabric Tightness of Satin Fabric Structure and UPF

The junctions are far apart, causing the threads to float and cover the junctions. Fabrics woven with satin weave are therefore soft and shiny. If the fabric tightness is kept high, heavy fabrics can be obtained. Satin weave; it has higher warp and weft density than twill or plain weaves. As a result, the fabric pores are smaller and have less free space for UV radiation to pass through. Satin fabrics, on the other hand, are not stable due to their pores, have little thread passage and tend to group together, further reducing the free space.

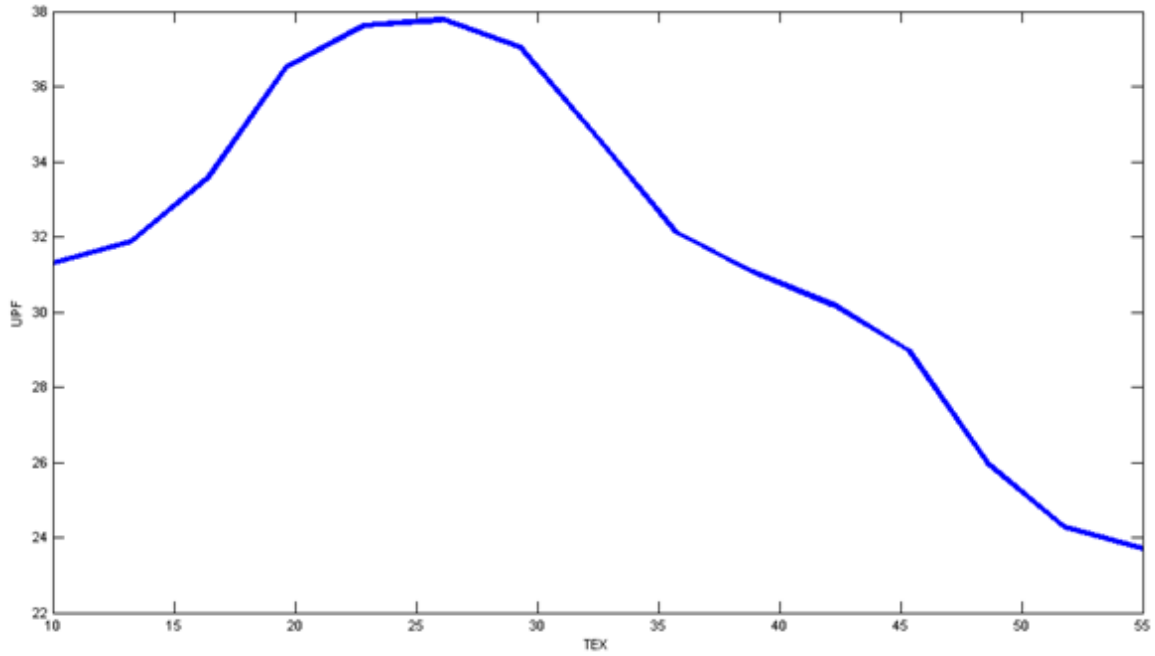

Figure 3. Variation Between Yarn Fineness and UPF of Satin Fabric Structure

Variation between yarn fineness and UPF of satin fabric constructions is presented in Figure 3. If we compare the UPF values of woven samples in terms of yarn fineness, we can observe that the UPF values first increase with yarn fineness (10 to 25 tex) and then decrease again, which means that the UV protection depends not only on the open area but also on the fabric thickness or volume porosity. Good UV protection in satin fabrics depends on the yarn fineness and the density of the fabric. Effect of yarn fineness on UPF in fabrics: 15 tex – 26 tex (good protection), 25 tex – 29 tex (very good protection), 45 tex – 55 tex (low protection).

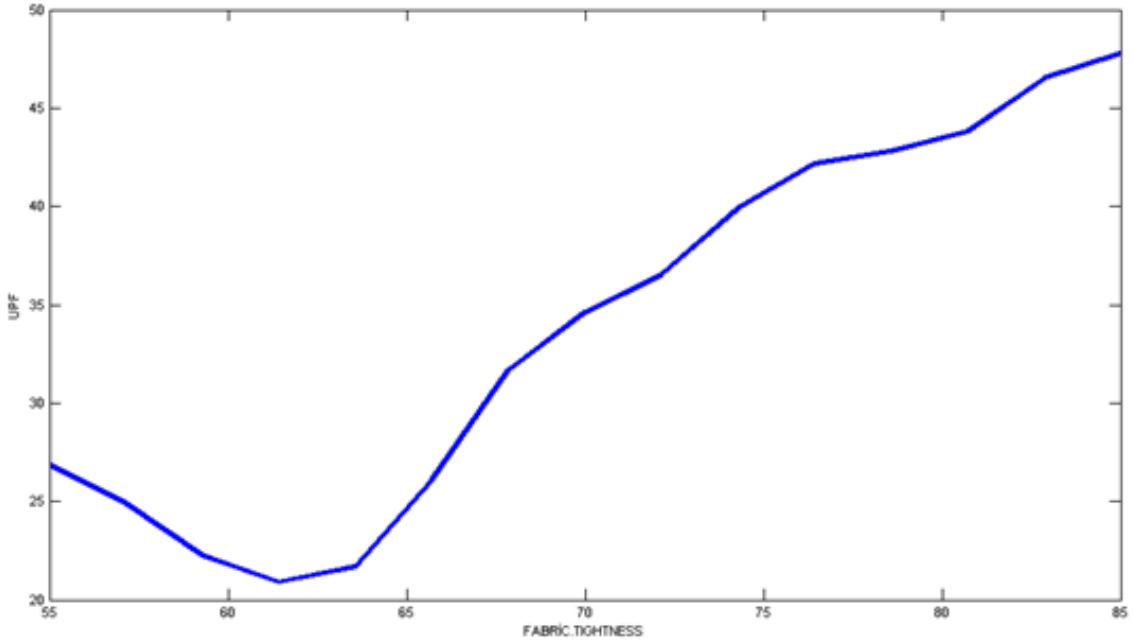

Figure 4. Variation Between Fabric Tightness and UPF of Satin Fabric Structure

Variation between fabric tightness and UPF of satin fabric constructions is shown in Figure 4. In any case, higher fabric tightness means higher UV protection, but there is a limit value at which each woven fabric provides good UV protection. Effect of fabric

tightness on UPF: 60%- 65% (low protection), 65% - 70% (good protection), 70% - 85% (very good protection).

3.2. Twill fabric constructions fuzzy prediction

For twill fabric, our entry membership functions, the yarn fineness, are chosen to be five, and the fabric tightness is five feet. Our output function, UPF, is determined in the twelve feet range. It was created with a hundred and twenty rule base in order to understand the effect of the relationship between the determined membership functions on the result. The relationship between the yarn fineness and fabric tightness of the satin fabric constructions and UPF is shown in Figure 5.

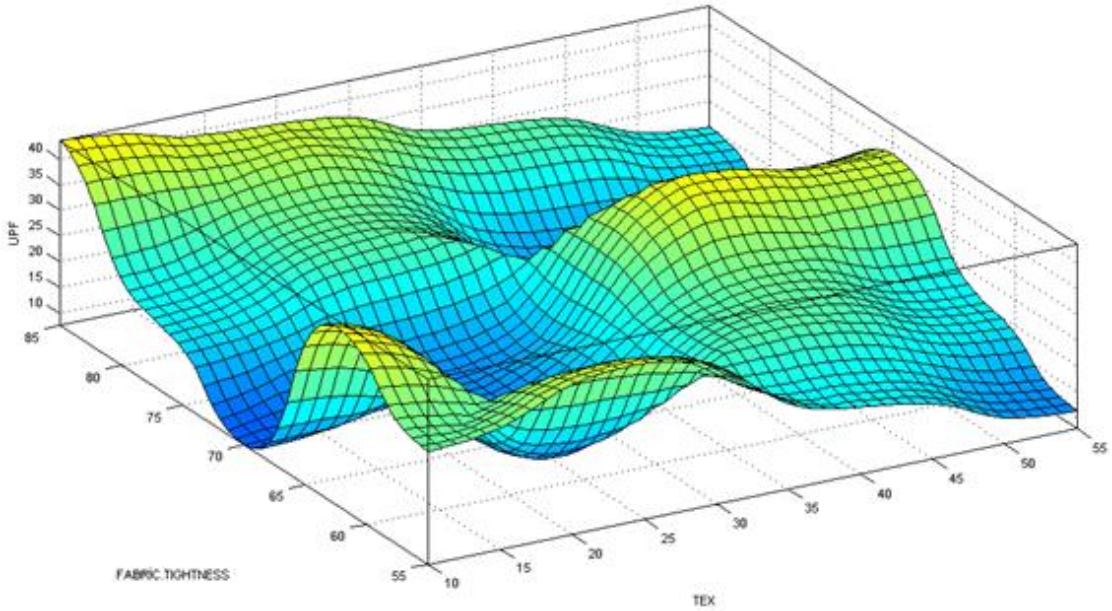

Figure 5. The Relationship Between Yarn Fineness and Fabric Tightness of Twill Fabric Structure and UPF

If warp skips are effective on one side of the fabric, weft skips are equally effective on the other side. Additionally, events may be equal to each other. In twill weave, there are many thread jumps from link to link. Twill fabrics have good UV protection when tightly woven. Higher warp/weft density per weave means higher fabric tightness and therefore higher UV protection.

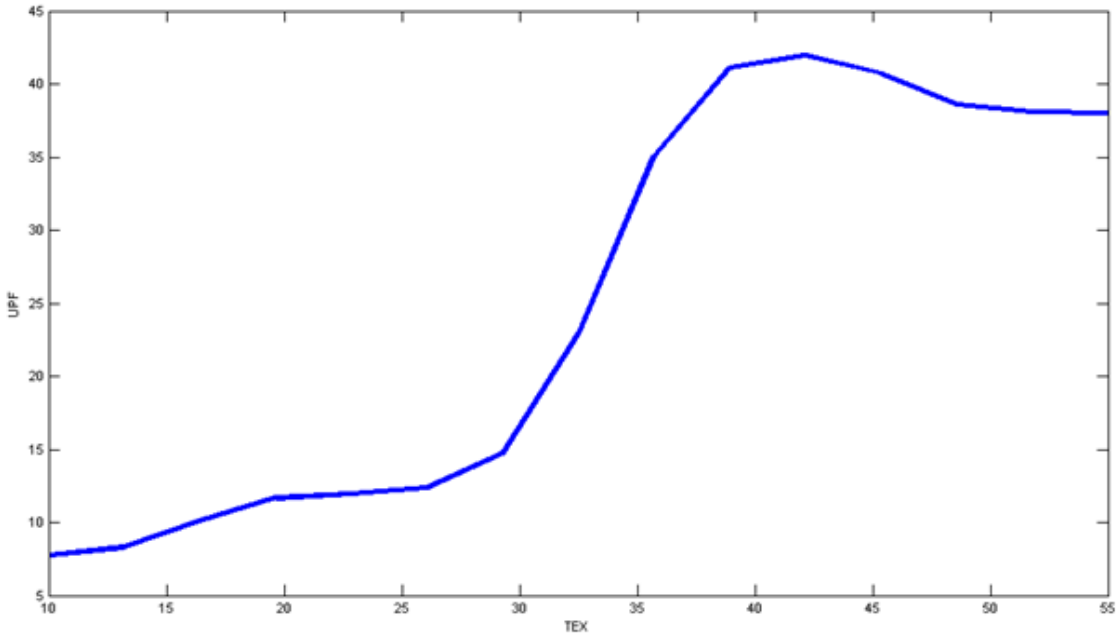

Figure 6. Variation Between Yarn Fineness and UPF of Twill Fabric Structure

Variation between Yarn fineness and UPF of twill fabric constructions is presented in Figure 6. Good UV protection in twill fabrics depends on the yarn fineness. The effect of yarn fineness on UPF in the fabrics: 10 tex – 30 tex (low protection), 35 tex – 40 tex (good protection), 40 tex – 55 tex (very good protection).

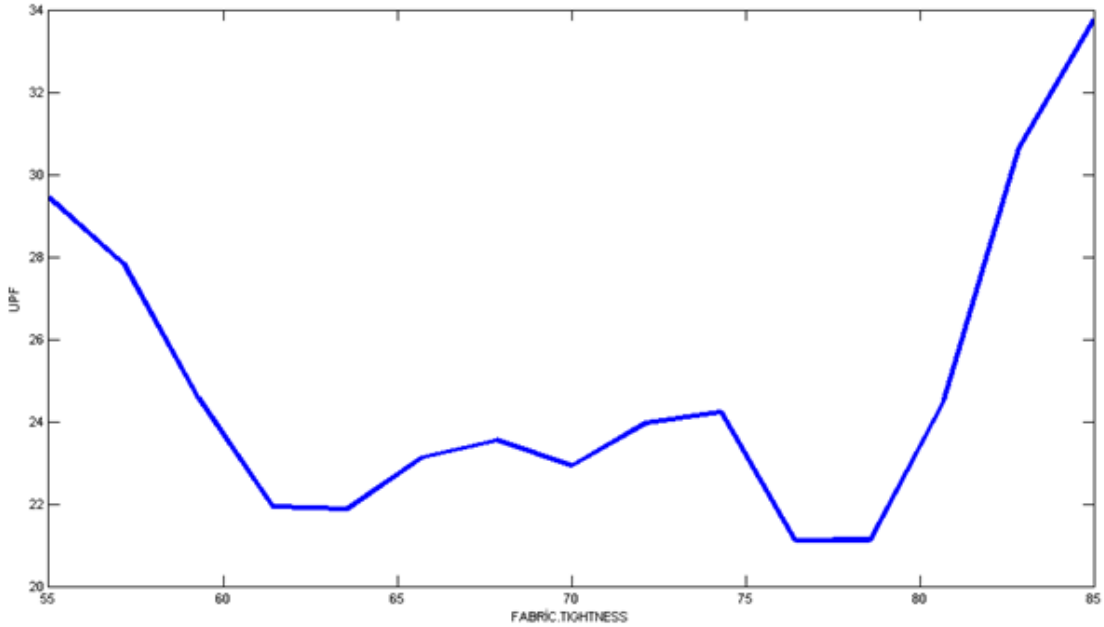

Figure 7. Variation Between Fabric Tightness and UPF of Twill Fabric Structure

Variation between fabric tightness and UPF of satin fabric constructions is shown in Figure 7. In any case, higher fabric tightness means higher UV protection, but there is a limit value at which each woven fabric provides good UV protection. Effect of fabric tightness on UPF: 55% - 60% (good protection), 62% - 78% (low protection), 80% - 85% (very good protection).

3.3. Plain fabric constructions fuzzy prediction

For plain fabric, our input membership functions, the yarn fineness, were chosen to be five, and the fabric tightness was chosen to be five feet. Our output function, UPF, is determined in the seven-foot range. It was created with a hundred and twenty rule base in order to understand the effect of the relationship between the determined membership functions on the result. The relationship between the yarn fineness and fabric tightness of the satin fabric constructions and UPF is shown in Figure 8.

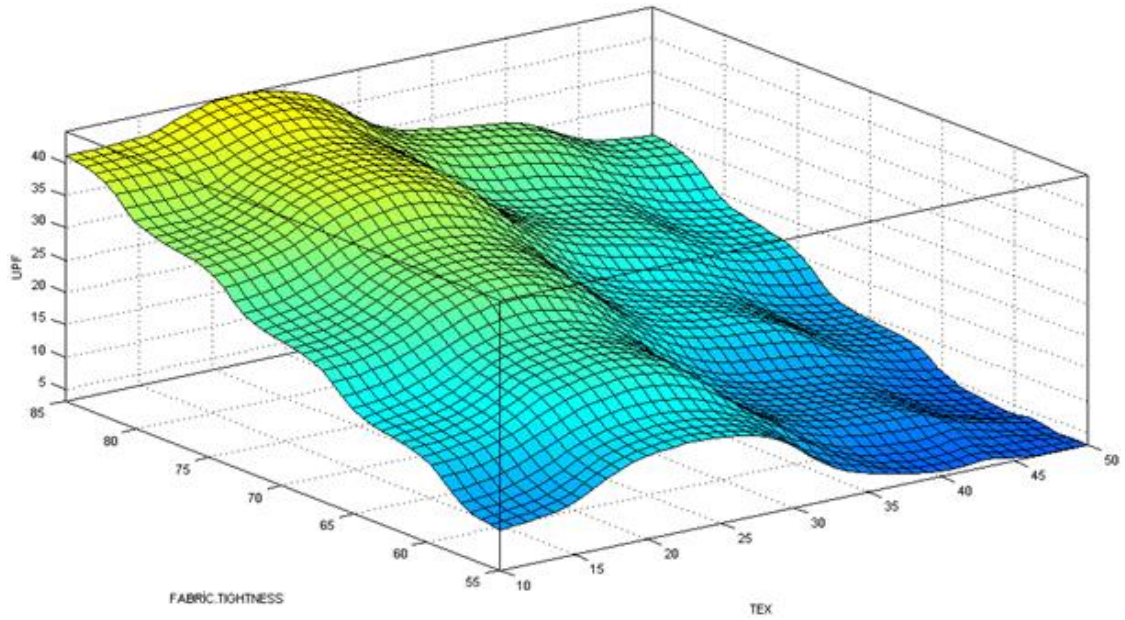

Figure 8. The Relationship Between Yarn Fineness and Fabric Tightness of Plain Fabric Structure and UPF

Plain braid is the simplest of braids. The smallest unit consists of two warps and two wefts. A plain weave fabric is the same on both sides. In a plain woven fabric with the same warp and weft density and the same warp and weft thread linear density, it is seen that the weft and warp threads are curled equally. In fabrics woven with plain weave, each thread gives maximum support to the adjacent thread. For this reason, the texture of these fabrics is stronger than other fabrics. It has a very stable and uniform form as a result of the macro pores and greater thread passage in plain fabrics. As a result, plain fabrics do not offer low UV protection.

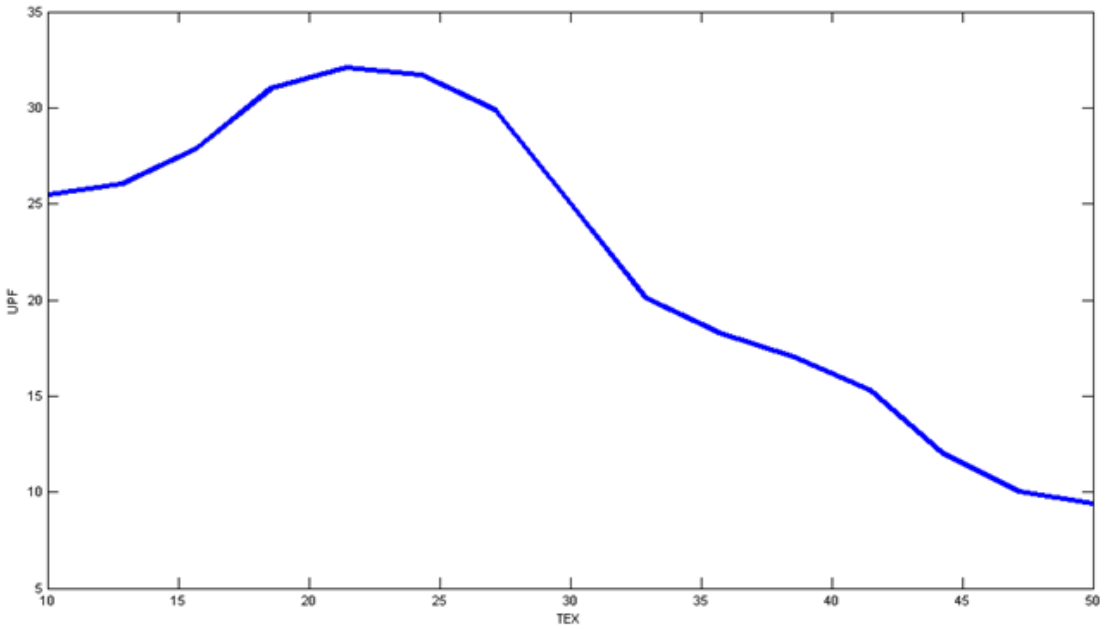

Figure 9. Variation Between Yarn Fineness and UPF of Plain Structure

Variation between yarn fineness and UPF of satin plain structure is presented in Figure 9. Good UV protection for plain fabrics depends on the yarn fineness and the fabric tightness of the fabric. The effect of yarn fineness on UPF in fabrics: 10 tex – 18 tex (good protection), 20 tex – 28 tex (very good protection), 30 tex- 55 tex (low protection).

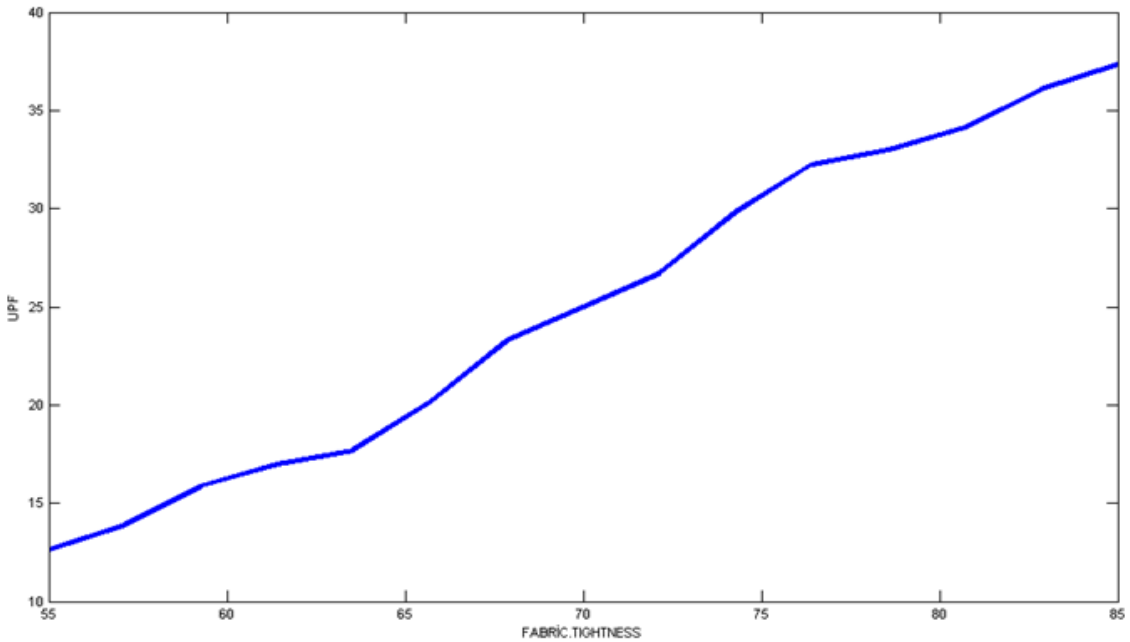

Figure 10. Variation Between Fabric Tightness and UPF of Plain Fabric Structure

Variation between fabric tightness and UPF of plain fabric constructions is presented in Figure 10. In any case, higher fabric tightness means higher UV protection, but there is a limit value at which each woven fabric provides good UV protection. Fabric tightness effect on UPF: 55% - 70% (low protection), 70%- 80% (good protection), 80% - 85% (very good protection).

Table 3. Comparison of Experimental and Fuzzy Values of Fabric Structures of UPF

TEX	FABRIC TIGHTNESS	SATIN UPF		TWILL UPF		PLAIN UPF	
		Fuzzy	Experiment	Fuzzy	Experiment	Fuzzy	Experiment
10	55	46	43	29,6	31	9,44	9,9
15	60	19,8	18,3	34,8	31,6	17,3	18,6
20	65	25,8	27	13,5	14,1	25,5	23
25	70	37,9	35	12	12,9	31,4	29,2
30	75	42,9	45	27,5	25	30,9	31,1
35	80	41,1	38	18,4	19	27,3	29
40	85	46,1	49	18,4	17	27,3	26
45	85	44,8	41	27,4	29	26,8	25,2
50	85	40,5	43	21,8	20,2	25	27
55	85	39,2	36	20,2	21,4	20	21,8

Comparison of experimental and fuzzy values of fabric structures is presented in Table 3. There is a 9% similarity between the experimental and fuzzy values of UPF. When the average values in Table 3. are compared; from the comparison of the average values it is obvious that there is a direct relationship between the yarn fineness and fabric tightness values of these fabrics with 3 different structures and the UPF value, on the basis of the structural features of the fabrics, regarding UV transmission. From the UPF results obtained for different woven fabrics, a higher UPF value was reached for satin fabrics according to the yarn fineness and fabric tightness values.

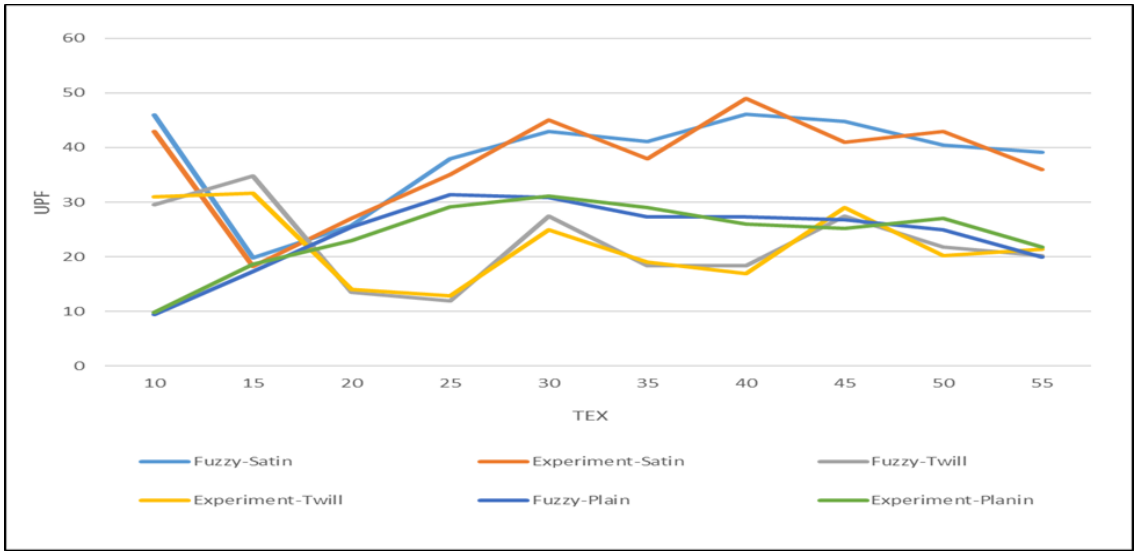

Figure 11. Comparison of Experimental and Fuzzy Values of Satin, Twill, Plain Woven Fabric Structures

Comparison of experimental and fuzzy values of UPF for satin, twill, plain woven fabric structures is presented in Figure 11. There are various factors that affect the UV protection properties of woven fabric.

4. Conclusion

In this study, it was seen that the production of clothes that can protect people from exposure to UV radiation can be achieved, especially in regions where sunlight is received more due to climatic conditions.

It is seen that the data obtained from the study conducted as fuzzy logic estimation contains positive results that can be applied in businesses. It is hoped that these data can provide initial information when considering further research studies on these topics. In the light of the data obtained from this study, the following conclusions can be drawn.

Fabrics such as yarn structure (fiber type, twist), fabric constructions are primary (weave type, warp/weft density, fabric tightness) and secondary (cover factor, porosity, thickness) fabric geometry parameters, knowing the UPF value of the garment will be more useful for the person wearing the garment made of UV protected fabrics. As a result, in terms of UPF value, satin fabrics can be considered as a widely used protective fabric constructions compared to other twill and plain fabrics, since the possibility of light transmission is low.

In order to protect the human skin from harmful UV rays, it is necessary to pay attention to fabric constructions. The high protection of satin woven fabric has revealed the necessity of further researching this woven constructions and ensuring its more widespread use.

Authorship contribution statement

M. Kodaloğlu: Conceptualization, Methodology, Data Curation, Original Draft Writing

F. Akarslan Kodaloğlu: Visualization, Supervision/Observation/Advice.

Declaration of competing interest

The authors declare that they have no known competing financial interests or personal relationships that could have appeared to influence the work reported in this paper.

Acknowledgment

As the authors of this study, we declare that we do not express any support or gratitude.

Ethics Committee Approval and/or Informed Consent Information

As the authors of this study, we declare that we do not have any ethics committee approval and/or informed consent statement.

References

[1] D.P. Dubrovski, M. Brezocnik, "Prediction of the Ultraviolet Protection of Cotton Woven Fabrics Dyed with Reactive Dyestuffs", *Fibres & Textiles in Eastern Europe*, Vol.17, No.1, 55-59, 2009.

[2] P.D. Dubrovski, D. Golob, "Effects of Woven Fabric Construction and Color on Ultraviolet Protection", *Textile Research Journal*, 79(4), 351-359, 2009.

[3] S.B. Stankovic, D. Popovic, G.B. Poparic. "Ultraviolet Protection Factor of Gray-state Plain Cotton Knitted Fabrics", *Textile Research Journal*, Vol.79, No.11, 1034-1042, 2009.

[4] P.H. Gies, C.R. Roy, S. Toomey, "Protection against solar ultraviolet radiation", *Mutation Research – Fundamental and Molecular Mechanisms of Mutagenesis*, Vol.422, No.1, 15-22, 1998.
[5] P.H. Gies, C.R. Roy, G. Holmes, "Ultraviolet Radiation Protection by Clothing: Comparison of In vivo and In vitro Measurements", *Radiation Protection Dosimetry*, 91(1-3), 247-250, 2000.
[6] K. Dimitrovski, F. Sluga, "Evaluation of the Structure of Monofilament PET Woven Fabrics and their UV Protection Properties", *Textile Research Journal on line first*, December 4, Vol.0, No.0, 1-11, 2009.
[7] K. Dimitrovski, F. Sluga, R. Urbas, "Evaluation of the Structure of Monofilament PET Woven Fabrics and their UV Protection Properties", *Textile Research Journal*, 80(11), 1027–1037, 2010.
[8] H. Gabrijelčič, R. Urbas, F. Sluga, "Influence of Fabric Constructional Parameters and Thread Colour on UV Radiation Protection", *Fibres &Textiles in Eastern Europe*, Vol.17, No.1, 46-54, 2009.
[9] D.P. Dubrovski, D. Golob, "Effects of Woven Fabric Construction and Colour on Ultraviolet Protection", *Textile Research Journal*, Vol.79, No.4, 351-359, 2009.
[10] G. Hustvedt, P.C. Crews, "The Ultraviolet 3. Protection Factor of Naturally-pigmented Cotton", *The Journal of Cotton Science*, Vol. 9, No. 47, pp. 47-55, 2005.
[11] J. Alvarez, B.L. Symonowicz, "Examination of the Absorption Properties of Various Fibres in Relation to UV Radiation", *AUTEX Res. J*. 3(2), 72-77, 2003.
[12] D. Gupta, A. Jain, S. Panwar, "Anti UV and Antimicrobial Properties of Some Natural Dyes on Cotton", *Indian Journal of Fibre and Textile Research*, 30(2), 190–195, 2005.
[13] P. Bajaj, V.K. Kothari, S.B. Ghosh, "Some Innovations in UV Protective Clothing", *Indian J. of Fibres and Textile Research*, 35(4),315-329, 2000.
[14] D. Saravanan, "UV protection textile materials", *AUTEX Res. J.*, 7(1), 53-62, 2007.
[15] C.A. Wilson, A.V. Parisi, "Protection from Solar Erythemal Ultraviolet Radiation – Simulated Wear and Laboratory Testing", *Textile Research Journal*, 76(3), 216-225, 2006.
[16] T. Gambichler, A. Avermaete, A. Bader, "Ultraviolet protection by summer textiles, Ultraviolet transmission measurements verified by determination of the minimal erythemal dose with solarsimulated radiation", *British Journal of Dermatology*, 144, 484-489, 2001.
[17] I. Algaba, A. Riva, P.C. "Crews, Influence of fiber type and fabric porosity on the UPF of summer fabrics", *AATCC Review*, 4(2), 26-31, 2004.
[18] I. Algaba, A. Riva, "Modelization of the Influence of the Wearing Conditions of the Garments on the Ultraviolet Protection Factor", *Textile Research Journal*, Vol.77, No.11, 826-836, 2007.
[19] M. Varga, J.M. Botet, E.S.V. Puntes, "Nano-cotton Fabrics with High Ultraviolet Protection", *Textile Research Journal on line first*, October 13, Vol.0, No.0, 1-9, 2009.
[20] C.A. Willson, N.K. Bevin, R.M. Laing, "Solar Protection Effect of Selected Fabric and Use Characteristics on Ultraviolet Transmission", *Textile Research Journal*, Vol.78, No.2, 95-104, 2008a.
[21] M. Kodaloğlu , F. Akarslan Kodaloğlu, "Evaluation of Thermal Comfort In Terms of Occupational Safety In Weaving Facilities By Fuzzy Logic", *International Journal of 3D Printing Technologies and Digital Industry*, c. 6, sayı. 2, ss. 273-279, Ağu. 2022.

Süleyman Demirel Üniversitesi Fen Edebiyat Fakültesi Fen Dergisi https://dergipark.org.tr/sdufeffd
Süleyman Demirel University Faculty of Arts and Sciences Journal of Science e-ISSN: 1306-7575
Research Article, 2024, 19(1): 53-62, DOI: 10.29233/sdufeffd.1413620

Synthesis, Structural Analysis, Antimicrobial Activity and The Molecular Electrostatic Potential Surface (MEP) of 2/3/4-Chloro Benzamide-Spiro[Benzo[B]Thiophene-Dioxolane] Derivatives

Naki Çolak[1a*], Fatma Şahin[1b], Gülnihal Erten[1c], Sinan Mithat Muhammet[2]

[1]Department of Chemistry, Faculty of Sciences and Arts, Hitit University, Çorum, TÜRKİYE
[a] https://orcid.org/0000-0001-7181-9556
*corresponding author: nakicolak@hitit.edu.tr
[b] https://orcid.org/0009-0002-7552-0844
[c] https://orcid.org/0000-0002-5441-2292
[2]Department of Materials and Materials Processing Technologies, Vocational School of Technical Sciences, Gazi University, Ankara, TÜRKİYE
https://orcid.org/0000-0001-6250-9476

(Received: 02.01.2024, Accepted: 03.04.2024, Published: 27.05.2024)

Abstract: In this research, 2-amino-4,7-dihydro-5H-spiro[benzo[b]thiophene-6,2'-[1,3]dioxolane]-3-carbonitrile (ST) was synthesized using the Gewald method, starting with 1,4-dioxaspiro[4,5]decan-8-one ketone. The structures of compounds were characterized through FT-IR, ^{1}H-NMR, and ^{13}C-NMR spectra. The antimicrobial properties of the compounds were examined by the disk diffusion process. The compounds (N1-3) did not exhibit effectiveness against the *E. Coli (ATCC)* and *S. Aureus (ATCC)* bacteria. The molecular electrostatic potential surface (MEP) of all compounds was calculated via DFT calculations based on the optimized geometries at the B3LYP/6-31G (d,p) level of theory. Negative potential regions were located over the oxygen and nitrogen atoms, whereas positive potential regions were identified over the oxygen and sulfur atoms. Conceptually, computations of the molecular structures of the compounds were carried out using molecular modeling software, specifically GaussView 5.0 and the GAUSSIAN 09 package programs. Additionally, computations were performed for the HOMO and LUMO molecular orbitals of isolated molecules in the gas phase. Molecular electrostatic potential (MEP) surfaces were used to visualize potential interactions between receptors and ligands over the steady-state geometries of the molecules and to highlight the electrophilic and nucleophilic regions of the molecules.

Key words: Amino Thiophene, Spiro Compounds, Benzamide Derivatives, Molecular Electrostatic Potential Surface

1. Introduction

Amides, which constitute a notable subgroup in the field of organic chemistry and were originally thought to exist exclusively in living organisms, gained new importance in synthetic chemistry with the synthesis of urea by the German chemist Friedrich Wöhler in 1828 [1]. Subsequent research during that period led to numerous significant discoveries related to amides. The ability to synthesize amide compounds under controlled laboratory conditions and to gain a detailed understanding of their structures also provided opportunities to elucidate the fundamental processes within biological systems.

Amides are typically compounds containing one or more amino groups attached to a carbonyl group. The synthesis of amide compounds, such as those derived from

structurally diverse amino or carboxylic acid derivatives, as used in this study, often requires specific conditions depending on the desired structure and intended applications of the amides [2,3]. The chemical structure of amides not only plays a crucial role during their synthesis but also holds significant importance in the biological context.

The structural diversity of amides makes them important in various fields, including biochemistry [4], pharmaceutical chemistry [5, 6], polymer science [7, 8], and materials science [9]. Amide groups, particularly those found in essential compounds like amino acids, play a critical role in biological systems and are frequently employed in the design of drug molecules to enhance efficacy or achieve specific targets. In a study conducted in 2020, it has been demonstrated that [1+1] condensed furan and thipohene-based cycloheterophane amide derivatives are effective against *S. aureus, B. cereus, E. coli, Listeria monocytogenes, Salmonella typhimurium* bacterial strains, and *C. albicans* yeast culture [10]. Bondock et al synthesized heterocyclic amide derivatives and determined that these compounds exhibited high efficacy, in vitro assays. Additionally, some derivatives exhibited antifungal activity [11]. A study of comparing the ligand and metal complexes of benzo[b]thiophene-2-carbohydrazide, reported that antimicrobial activity was observed with the ligand, but an increase in antimicrobial activity was noted with them metal complex [12]. Different types of amides can exhibit various therapeutic effects, including antibacterial [13], antiviral [14], anticancer [15], antiparkinson [16], and analgesic [17] properties.

In this study, the amine compound used in the synthesis of amide derivatives is 2-amino-4,7-dihydro-5H-spiro[benzo[b]thiophene-6,2'-[1,3]dioxolane]-3-carbonitrile (ST). This compound is structurally a thiophene ring. Thiophene compounds have played significant roles in many studies due to their high chemical reactivity. It is known that some mushrooms and a perennial plant species contain the thiophene rings. These biologically active compounds frequently appear in pharmacological studies with different properties such as antioxidant [18], antibacterial [19], antitumor [20] etc. Due to the effects originating from thiophene, the 2-aminothiophene compound has been preferred to include in our target compounds.

In the front molecular orbital analysis, certain reactivity descriptors were utilized, investigated through the DFT approach and B3LYP/6-31G (d,p) level of theory. These descriptors provide important information for determining the chemical reactivity, stability, and behavior of the molecular structure. The ionization potential **(IP)** for the tendency to lose electrons, the electron affinity **(EA)** for the tendency to gain electrons, and the electronegativity **(χ)** values for the ability to attract electrons are examined in a molecule. The resistance a molecule exhibits in reactions is quantified by chemical hardness **(η)**, and sensitivity is determined by chemical softness **(S)**. Chemical potential gauges a molecule's capacity to either lose or gain electrons. A higher global electrophilicity ındex **(ω)** value signifies a more pronounced electrophilic character, while molecular electrostatic potential **(MEP)** specifies electron density around a molecule's nuclei.

2. Material and Method

Melting points of all samples were measured using the open capillary method with a Gallenkamp apparatus and were reported without any corrections. Fourier Transform Infrared (FT-IR) spectra, including the Attenuated Total Reflectance (ATR) technique, were obtained from a Thermo Nicolet 6700 Spectrometer in the Chemistry Department of Hitit University. Nuclear magnetic resonance spectra were obtained at Giresun University using a Bruker AVANCE III spectrometer, 400 MHz for ^{1}H-NMR and 100

MHz for ^{13}C/APT-NMR, in $CDCl_3$ (with TMS as the internal standard). The mass analyses of the compounds were determined using Liquid Chromatography-Mass Spectrometry (LC-MS/MS) method with an AB Sciex 3200 Q Trap Mass Spectrometer located at Hitit University Scientific Technical Application and Research Center. The chemicals obtained from Sigma-Aldrich were of high purity, and therefore, no purification process was deemed necessary. The course of reactions was observed by Thin-Layer Chromatography (TLC) on silica gel aluminum sheets with a UV indicator at 254 nm. Antimicrobial activity assays were performed at Amasya University Central Research and Application Laboratory.

2.1. Synthesis Procedures

2.1.1. 2-amino-4,7-dihydro-5H-spiro[benzo[b]thiophene-6,2'-[1,3]dioxolane]-3-carbonitrile (ST)

The title compound coded as **ST** was synthesized according to the relevant literature studies [21-23] from 1,4-dioxaspiro[4.5]decan-8-one (0.01 mmol), malononitrile, sulfur (0.01 mmol), and morpholine (0.01 mmol), and used for the synthesis of the chloro benzamide-thiophene compounds **(Scheme 1)**.

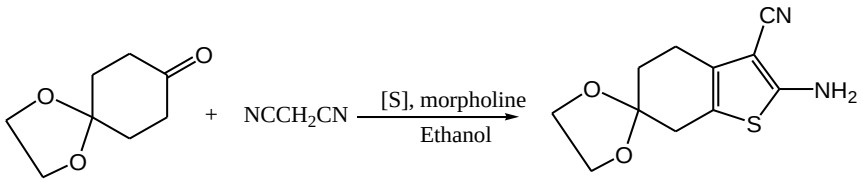

Scheme 1. Synthesis of **ST**

2.1.2. 2/3/4-chloro-N-(3-cyano-4,7-dihydro-5H-spiro[benzo[b]thiophene-6,2'-[1,3]dioxolan]-2-yl)benzamide] derivatives (N1-3)

The reaction mixture containing **ST** (1.0 mmol), toluene (1.0 mmol), and pyridine (1.0 mmol) was stirred for approximately 30 minutes at room temperature in a dry nitrogen atmosphere. Subsequently, 2-chlorobenzoyl chloride, 3-chlorobenzoyl chloride or 4-chlorobenzoyl chloride (1.0 mmol) were slowly introduced drop by drop to the reaction flask. The obtained mixture was stirred at 110°C for 6-8 h. It was allowed to cool to room temperature, and then water (20 ml) was added. The product **(N1-3)** was extracted into the organic phase with ethyl acetate (2x20 mL) and then obtained in solid form after the removal of the solvent **(Scheme 2)**.

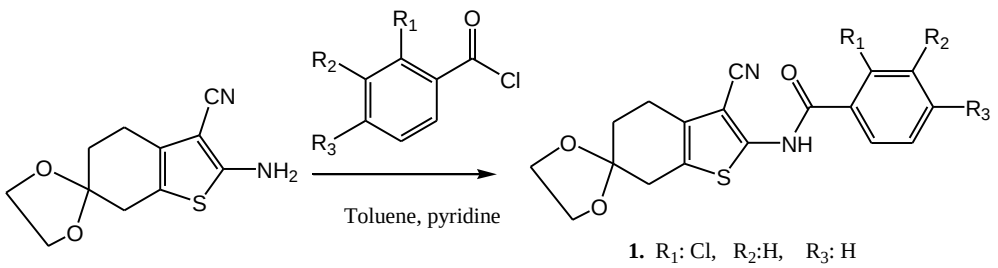

Scheme 2. Synthetic prodecure of ST-benzamide derivatives **(N1-3)**

2-chloro benzamide derivative of ST (N1) As started in headline 2.1.2, it was prepared on the basis of items ST and 2-chlorobenzoyl chloride. FT-IR ATR, cm^{-1}: 3272, 3214 NH, 2984-2867 aliphatic C-H, 2224 CN, 1670 CO. ^{1}H-NMR spectral data (ppm, $CDCl_3$) : 9.60 (s, 1H, NH), 7.94 (d, 1H, Ar-H) 7.52 (d and m, 3H, Ar-H), 4.06 (s, 4H, OCH_2), 2.91 (s, 2H, CH_2), 2.85 (t, 2H, CH_2), 1.96 (t, 2H, CH_2). ^{13}C-NMR APT (ppm, $CDCl_3$): 162.19, 147.17, 133.10, 131.64, 130.77, 130.34, 127.60, 126.29, 114.05, 108.00, 64.80, 34.52, 31.00, 22.77.

3-chloro benzamide derivative of ST (N2) As started in headline 2.1.2, it was prepared on the basis of items ST and 3-chlorobenzoyl chloride. FT-IR ATR cm^{-1}: 3247, 3207 NH, 2944-2880 aliphatic C-H, 2225 CN, 1669 CO. ^{1}H-NMR spectral data (ppm, $CDCl_3$): 9.43 (s, 1H, NH), 7.96 (s, 1H, Ar-H) 7.83 (d, 1H, Ar-H), 7.58 (d, 1H, Ar-H) 7.46 (t, 1H, Ar-H) 4.06 (s, 4H, OCH_2), 2.89 (s, 2H, CH_2), 2.81 (t, 2H, CH_2), 1.98 (t, 2H, CH_2). ^{13}C-NMR APT (ppm, $CDCl_3$): 162.94, 147.55, 134.99, 133.43, 132.70, 130.43, 130.00, 128.12, 125.85, 114.20, 108,00, 64.79, 34.10, 30.85, 22.67.

4-chloro benzamide derivative of ST (N3) As started in headline 2.1.2, it was prepared on the basis of items ST and 4-chlorobenzoyl chloride. FT-IR ATR cm^{-1}: 3265, 3202 NH, 2989-2890 aliphatic C-H, 2222 CN, 1665 CO. ^{1}H-NMR spectral data (ppm, $CDCl_3$): 9.27 (s, 1H, NH), 7.90 (d, 2H, Ar-H) 7.51 (d, 2H, Ar-H), 4.06 (s, 4H, OCH_2), 2.90 (s, 2H, CH_2), 2.82 (t, 2H, CH_2), 1.99 (t, 2H, CH_2). ^{13}C-NMR APT (ppm, $CDCl_3$): 163.05, 147.92, 139.27, 130.23, 129.28, 129.15, 126.11, 114.46, 107.99, 64.63, 34.38, 30.98, 22.53.

2.2. Theoretical Calculations

All compounds underwent quantum chemical calculations using the Gaussian 09 program package, employing density functional theory (DFT) [24]. The full optimization of the molecular geometries of all compounds was performed using the Becke-3-Lee-Yang-Parr (B3LYP) functional and 6-31 G (d,p) basis set. [25, 26].

2.2.1. Frontier Molecular Orbital Analysis

The highest occupied molecular orbital is known as HOMO, and the lowest unoccupied molecular orbital is known as LUMO. HOMO orbitals, being occupied, have an electron-donating tendency, while LUMO orbitals, being unoccupied, have an electron-accepting tendency. These concepts facilitate the understanding of chemical reactivity and play a crucial role in explaining the mechanisms of chemical reactions. Ionization potential is directly related to HOMO energy, while electron affinity to LUMO energy. Fig. 1 and Table 1 illustrate the computed E_{HOMO} and E_{LUMO} energy values, $\Delta E_{HOMO-LUMO}$ band gaps, and other descriptors for all compounds. As indicated by Figure 1 and Table 1, the energy band gaps ($\Delta E_{HOMO-LUMO}$) of 1, 2 and 3 were found to be 2.5269, 2.4969 and 2.5377 eV at B3LYP/6-31G (d,p) level of theory. The electrophilicity index (ω) is helpful in predicting the formation of chemical bonds in biomolecules, thus aiding in understanding of the mechanisms of chemical reactions.

2.2.2. Molecular Electrostatic Potential Surface

Molecular electrostatic potential surface (MEP) is a concept that illustrates the electron density and electrical interactions surrounding a molecule. In simpler terms, MEP demonstrates how a molecule distributes electron density in space and how this distribution affects the electrical potential on the molecular surface. In our study, MEP potentials of all molecules were modeled using DFT calculations. For geometry optimization in DFT calculations, the B3LYP / 6-31G (d,p) level of theory was employed. The potential values of the molecules in the MEP diagrams provided in Figure 2 are

observed to decrease from blue to red. As seen in Figure 2, the negative potential regions are located over the oxygen and nitrogen atoms, whereas positive potential regions are found over the oxygen and sulfur atoms.

Additionally, chemical reactivity descriptors such as chemical potential (μ), chemical hardness (η) and chemical softness (S) were also calculated in this study and shown in **Table 1**. The corresponding values are calculated using the following formulas [27-30].

$$I = -E_{HOMO} \qquad A = -E_{LUMO} \qquad \eta = \frac{1}{2}(E_{LUMO} - E_{HOMO})$$

$$S = \frac{1}{2\eta} \qquad \chi = \frac{1}{2}(I + A) \qquad \omega = \frac{\mu^2}{2\eta}$$

$$\mu = -\frac{1}{2}(I + A) = \frac{1}{2}(E_{HOMO} + E_{LUMO})$$

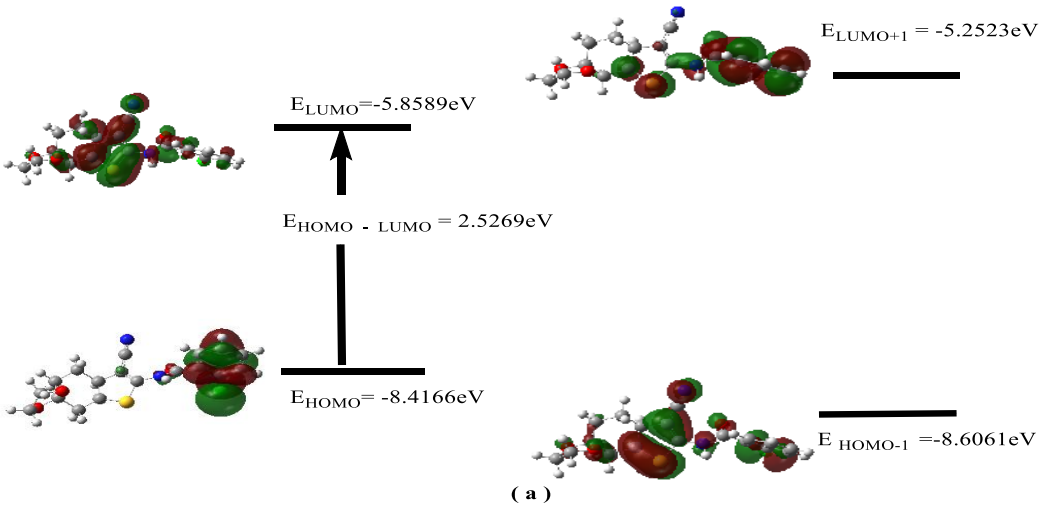

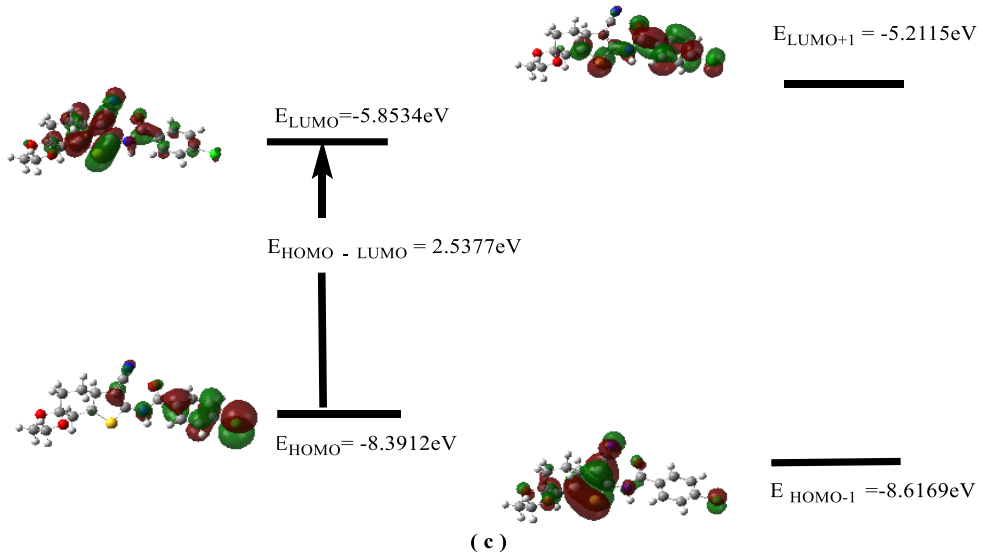

Figure 1. HOMO-LUMO energies of all compounds.

Table 1. Chemical reactivity descriptor result of all compounds

Molecular Properties (eV)	**1**		**2**		**3**	
	a.u.	**ev**	**a.u.**	**ev**	**a.u.**	**ev**
E_{HOMO}	-0.3083	-8.4166	-0.3084	-8.3885	-0.3085	-8.3912
E_{LUMO}	-0.2154	-5.8589	-0.2165	-5.8888	-0.2152	-5.8534
$\Delta E_{HOMO-LUMO}$	0.0929	2.5269	0.0918	2.4969	0.0933	2.5377
E_{HOMO-1}	-0.3164	-8.6061	-0.3167	-8.6142	-0.3168	-8.6169
E_{LUMO+1}	-0.1931	-5.2523	-0.2007	-5.4590	-0.1916	-5.2115
Ionization Potential **(IP)**	0.3083	8.4166	0.3084	8.3885	0.3085	8.3912
Electron Affinity **(EA)**	0.2154	5.8589	0.2165	5.8888	0.2152	5.8534
Chemical Hardness **(η)**	0.0465	1.2788	0.04595	1.2498	0.0466	1.2689
Electronegativity **(χ)**	0.2618	7.1377	0.2625	7.1387	0.2618	7.1223
Chemical Potential **(μ)**	-0.2618	-7.1377	-0.2625	-7.1387	-0.2618	-7.1223
Softness **(S) ev^{-1}**	10.75	0.3909	10.88	0.4000	10.73	0.3940
Electrophilicity index **(ω)**	0.737	19.919	0.749	20.388	0.735	19.988

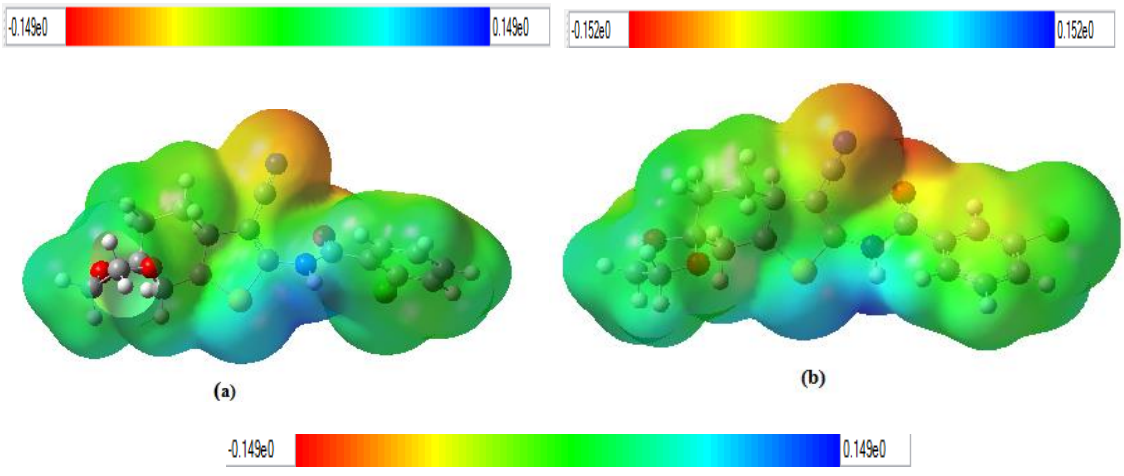

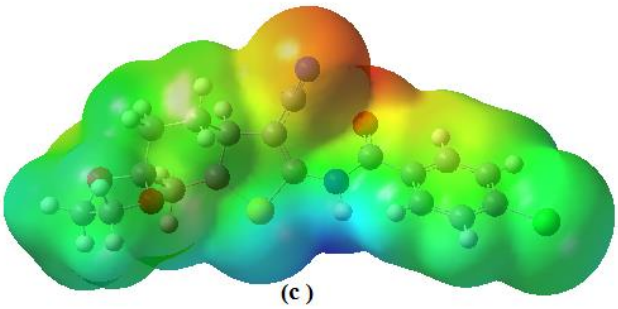

Figure 2. Molecular electrostatic potential surface (MEP) results of all compounds

2.3. Antimicrobial Activity with Disk Diffusion Test

The vulnerability of bacteria to antibiotics was determined on MH (Mueller Hinton) agar using Kirby-Bauer disk diffusion technique, in accordance with the guidelines outlined in CLSI January-2011 (Clinical and Laboratory Standards Institute) documents M02 and M07. MH (Mueller Hinton) agar was used for sterile, disposable, 15 cm diameter petri plates with a medium at a height of 4 mm. A few bacterial colonies that grew as pure colonies on culture plates were collected using a sterile extract and inoculated into MH broth, incubated at 37°C for 1-2 hours. After turbidity was developed, a typical turbidity was established by calibrating it to McFarland 0.5 (108 microorganisms/ml). Extensive sowing was performed from this suspension on MH agar medium using a sterile swab. Dilutions of the substances to be investigated were prepared with DMSO at concentrations of 2-1-0.5 and 0.25 mg/ml, respectively, and paper discs impregnated with 20µl of these dilutions were placed in the medium. 2 mg/ml streptomycin antibiotic was used for positive control. Petri dishes were incubated at 35-37ºC for 18–24 h and then inhibition zone diameters were measured. The results are shown in Table 2, in which inhibition zones are provided in millimeters and expressed as mean ±SE.

Table 2. The results of disk diffusion test

Bacterial İsolates	Mg/mL	Inhibition zone diameters (mm)			
E.Coli ATCC 25922		1	2	3	*Control Streptomycin*
	2	-	-	-	17
	1	-	-	-	
	0.5	-	-	-	
	0.25	-	-	-	
S.Aureus ATCC 25923	2	-	-	-	19
	1	-	-	-	
	0.5	-	-	-	
	0.25	-	-	-	

3. Results

This study has been occurred in two stages. In the first stage, we synthesized 2-amino-4,7-dihydro-5H-spiro[benzo[b]thiophene-6,2'-[1,3]dioxolane]-3-carbonitrile as the starting 1,4-dioxaspiro[4.5]decan-8-one. In the second stage, we prepared amid

compounds **(N1-3)** derivatives. Amit peaks were confirmed by FT-IR, which showed peaks at 3272, 3214 for compound 1, 3247, 3207 for compound 2, and 3265, 3202 for compound 3. Aliphatic C-H peaks were observed between 2989 and 2867 for compounds **(N1-3)**. CN peaks were observed at 2224 cm^{-1}, 2225 cm^{-1} and 2222 cm^{-1} and amide carbonyl peaks were observed 1670 cm^{-1}, 1669 cm^{-1}, 1665 cm^{-1} respectively for compounds **N1**, **N2** and **N3**.

The ^{1}H-NMR spectra of amide compounds have been carried out in $CDCl_3$ at room temperature. The peaks at 9.60, 9.43, and 9.27 ppm were attributed to NH protons. Aromatic protons were observed at 7.94-7.52 ppm for compound **N1**, 7.96-7.46 ppm for compound **N2** and 7.90-7.51 ppm for compound **N3**. Peaks of the amine compound were observed where expected and with expected cleavages. C peaks, observed in the ^{13}C-NMR APT spectra, confirmed the expected structure.

4. Conclusion

E. coli, which is an element of intestinal flora, and *S. aureus Streptomycin* in human skin have been found to have no effect according to the antibiotic reference. In determining and relating the areas of these compounds, it can be said that at least they will not disrupt the intestinal flora or harm the human skin. Additionally, frontier molecular orbital energies, chemical parameters and molecular electrostatic potentials (MEPs) were investigated with DFT approach 6-31G (d,p) level of theory. The *3-chloro benzamide derivative of ST,* **N2**, which has a low ionization potential (8.3885 eV), exhibits high activity.

Authorship contribution statement

N. Çolak: Project Administration, Conceptualization, Methodology; **F. Şahin**: Investigation, Visualization ; **G. Erten**: Original Draft Writing, Review and Editing; **S. M. Muhammet**: Original Draft Writing, Data Curation, Formal Analysis.

Declaration of competing interest

The authors declare that they have no known competing financial interests or personal relationships that could have appeared to influence the work reported in this paper.

Acknowledgment

This study was funded by Hitit University Scientific Research Projects Coordination Office under Project No FEF 19001.23.003.

Ethics Committee Approval and/or Informed Consent Information

As the authors of this study, we declare that we do not have any ethics committee approval and/or informed consent statement.

References

[1] O. Raubenheimer, "Friedrich Wöhler and the centenary of synthesis", The Journal of the American Pharmaceutical Association, 17, 973-980, 1928. https://doi.org/10.1002/jps.3080171008.

[2] R. A. Kyle and M. A. Shampo, "Justus von Liebig—leading teacher of organic chemistry", Mayo Clinic Proceedings, 76, 921-922, 2001. https://doi.org/10.4065/76.9.921.

[3] R. J. Ouellette and J. D. Rawn, "Amines and amides", in Organic chemistry study guide, Editors: R. J. Ouellette and J. D. Rawn, Elsevier, 2015, pp. 465-494. https://doi.org/10.1016/B978-0-12-801889-7.00023-6.

[4] R. Tripathi, J. P. Yadav, P. Pathak, M. H. Almatarneh and A. Verma, "Polymer–drug linking through amide bonds: the chemistry and applications in drug delivery", in Polymer-Drug Conjugates: Linker Chemistry, Protocols, and Applications. United States: Elsevier Science & Technology, 2023. https://doi.org/10.1016/B978-0-323-91663-9.00007-2.

[5] A. Sathya, T. Prabhu, S. Ramalingam, "Structural, biological, and pharmaceutical importance of antibiotic agent chloramphenicol", Heliyon, 6, e03433, 2020. https://doi.org/10.1016/j.heliyon.2020.e03433.

[6] S. Ghaffari, N. Roshanravan, H. Tutunchi, A. Ostadrahimi, M. Pouraghaei and B. Kafil, "Oleoylethanolamide, a bioactive lipid amide, as a promising treatment strategy for coronavirus/COVID-19", Archives of Medical Research, 51, 464-467, 2020. https://doi.org/10.1016/j.arcmed.2020.04.006.

[7] J. Li, F. Yu, Y. Chen and D. Oupický, "Polymeric drugs: Advances in the development of pharmacologically active polymers", Journal of Controlled Release, 219, 369-382, 2015. https://doi.org/10.1016/j.jconrel.2015.09.043.

[8] S. Abdolmaleki and M. Ghadermazi, "Novel pyridinedicarboxamide derivatives and a polymeric copper(II) complex: Synthesis, structural characterization, electrochemical behavior, catalytic and cytotoxic studies", Inorganica Chimica Acta, 461, 221-232, 2017. https://doi.org/10.1016/j.ica.2017.02.023.

[9] A. Kar, M. A. Rather, M. Mandal and N. Karak, "Elastomeric biodegradable poly(ester amide urethane) as a tough and robust material", Progress in Organic Coatings, 182, 107684, 2023. https://doi.org/10.1016/j.porgcoat.2023.107684.

[10] B. Erkuş, H. Özcan and Ö. Zaim, "Synthesis and antimicrobial activity of four new [1+1] condensed furan and thiophene-based cycloheterophane amides", Journal of Heterocyclic Chemistry, 57 (4), 1956-1962, 2020. http://doi.org/10.1002/jhet.3922.

[11] S. Bondock, W. Fadaly and M. A. Metwally, "Synthesis and antimicrobial activity of new thiazole, thiophene and pyrazole derivatives containing benzothiazole moiety", European Journal of Medicinal Chemistry, 45 (9), 3692-3701, 2010. https://doi.org/10,1016/j.ejmech.2010.05.0218..

[12] N. G. Yernale, B. S. Mathada, S. Shivprasad, S. Hiremath, P. Karunakar and A. Venkatesulu, " Spectroscopic, theoretical and computational investigations of novel benzo [b] thiophene based ligand and its M(II) complexes: As hih portentous antimicrobial and antioxidant agents", Spectrochimica Acta Part A: Molecular and Biomolecular Spectroscopy, 302, 123114, 2023. https://doi.org/10.1016/j.saa.2023.123114.

[13] C. Rangel-Núñez, C. Ramírez-Trujillo, K. Hakkou, A. Suárez-Cruz, I. Molina-Pinilla and M. Bueno-Martínez, "Regiospecific vs. non regiospecific click azide-alkyne polymerization: In vitro study of water-soluble antibacterial poly(amide aminotriazoles" Materials Science and Engineering: C, 125, 2021. 112113. https://doi.org/10.1016/j.msec.2021.112113.

[14] E. Plebanek, E. Lescrinier, G. Andrei, R. Snoeck, P. Herdewijn and S. De Jonghe, "Emimycin and its nucleoside derivatives: Synthesis and antiviral activity", European Journal of Medicinal Chemistry, 144, 93-103, 2018. https://doi.org/10.1016/j.ejmech.2017.12.018.

[15] C. P. Kaushik, J. Sangwan, R. Luxmi, D. Kumar, D. Kumar, A. Das, A. Kumar and D. Singh, "Design, synthesis, anticancer and antioxidant activities of amide linked 1,4-disubstituted 1,2,3-triazoles", Journal of Molecular Structure (Part A), 1226, 129255, 2021. https://doi.org/10.1016/j.molstruc.2020.129255.

[16] A. Marzo, L. Dal Bo, N. Ceppi Monti, F. Crivelli, S. Ismaili, C. Caccia, C. Cattaneo and R. G. Fariello, "Pharmacokinetics and pharmacodynamics of safinamide, a neuroprotectant with antiparkinsonian and anticonvulsant activity", Pharmacological Research, 50, 77-85, 2004. https://doi.org/10.1016/j.phrs.2003.12.004.

[17] Y. Li, Y. Shang, X. Li, Y. Zhang, J. Xie, L. Chen, F. Gao and X. L. Zhou, "Design, synthesis, and biological evaluation of low-toxic lappaconitine derivatives as potential analgesics", European Journal of Medicinal Chemistry, 243, 114776, 2022. https://doi.org/10.1016/j.ejmech.2022.114776.

[18] G. A. Gevoryan, N. Z. Hakobyan, S. S. Hovakimyan, A. G. Melkonyan and G. A. Panosyan, "Synthesis and biological activity of β-aminoketones, secondary aminopropanols and oximes of 2-aminothiophen series", Russian Journal of General Chemistry, 89, 2328-2332, 2019. https://doi.org/10.1134/S1070363219110264.

[19] W. Kemnitzer, N. Sirisoma, C. May, B. Tseng, J. Drewe and S. X. Cai, "Discovery of 4-anilino-N-methylthieno[3,2-d]pyrimidines and 4-anilino-N-methylthieno[2,3-d]pyrimidines as potent apoptosis inducers", Bioorganic&Medicinal Chemistry Letters, 19(3), 3536-3540, 2009. https://doi.org/10.1016/j.bmcl.2009.04.145.

[20] R. Narlawar, J. R. Lane, M. Doddareddy, J. Lin, J. Brusse and A. P. Ijzerman, "Hybrid ortho/allosteric ligands for the adenosine A1 receptor", Journal of Medicinal Chemistry, 53(8), 3028-3037, 2010. https://doi.org/10.1021/jm901252a.

[21] N. Uludağ, G. Serdaroğlu, P. Sugumar, P. Rajkumar, N. Çolak and E. Ercağ, "Synthesis of thiophene derivatives: Substituent effect, antioxidant activity, cyclic voltammetry, molecular docking, DFT, and

TD-DFT calculations", Journal of Molecular Structure, 1257, 132607, 2022. https://doi.org/10.1016/j.molstruc.2022.132607.

[22] G. Serdaroğlu, N. Uludağ, E. Üstün and N. Çolak, "A novel series of tetrahydrothieno[2,3-c]pyridin-2-yl derivatives: fluorescence spectroscopy and BSA binding, ADMET properties, molecular docking, and DFT studies", New Journal of Chemistry, 47 (25), 11945-11963, 2023. https://doi.org/10.1039/D3NJ01648J.

[23] G. Serdaroğlu, N. Uludağ, N. Çolak and P. Rajkumar, "Nitrobenzamido substitution on thiophene-3-carboxylate; Electrochemical investigation, antioxidant activity, molecular docking, DFT calculations", Journal of Molecular Structure, 1271, 134030, 2023. https://doi.org/10.1016/j.molstruc.2022.134030.

[24] M. J. Frisch, G. W. Trucks, H. B. Schlegel, G.E. Scuseria, M.A. Robb, J. R. Cheeseman, ..., Gaussian 09, Revision C.01. Wallingford CT: Gaussian Inc., 2009.

[25] C. Lee, W. Yang and R. G. Parr, "Development of the Colle-Salvetti correlation-energy formula into a functional of the electron density", Physical Review B, 37, 785-789, 1988. https://doi.org/10.1103/PhysRevB.37.785.

[26] A. D. Becke, "Density-functional exchange-energy approximation with correct asymptotic behavior", Physical Review A, 38, 3098-3100, 1988. https://doi.org/10.1103/PhysRevA.38.3098

[27] T. Koopmans, "Über die Zuordnung von Wellenfunktionen und Eigenwerten zu den Einzelnen Elektronen Eines Atoms", Physica, 1, 104-113, 1934. https://doi.org/10.1016/S0031-8914(34)90011-2.

[28] R. G. Pearson, "Chemical hardness and density functional theory", Journal of Chemical Sciences, 117, 369-377, 2005. https://doi.org/10.1007/BF02708340

[29] R. G. Parr and R. G. Pearson, "Absolute Hardness: Companion Parameter to Absolute Electronegativity", Journal of the American Chemical Society, 105, 7512-7516, 1983. https://doi.org/10.1021/ja00364a005.

[30] R. K. Roy, K. Choho, F. De Proft and P. Geerlings, "Reactivity and stability of aromatic carbonyl compounds using density functional theory-based local and global reactivity descriptors", Journal of Physical Organic Chemistry, 12, 503-509, 1999. https://doi.org/10.1002/(SICI)1099-1395(199906)12:6<503::AID-POC149>3.0.CO;2-2.

Süleyman Demirel Üniversitesi Fen Edebiyat Fakültesi Fen Dergisi https://dergipark.org.tr/sdufeffd
Süleyman Demirel University Faculty of Arts and Sciences Journal of Science e-ISSN: 1306-7575
Research Article, 2024, 19(1): 63-74, DOI: 10.29233/sdufeffd.1371161

The Effect of Particle Size of Polyvinyl Alcohol/Bentonite Clay Mixture on the Radiation Shielding: A Monte Carlo Study

Tuğba Manici[1,2,*], Gökhan Algün[3], Namık Akçay[3], Bayram Demir[3]

[1]Radiotheraphy Program, Istanbul Sisli Vocational School, İstanbul, TURKEY
[2]Nuclear Physics, Institue of Graduate Studies in Science, Istanbul University, 34320, İstanbul, TURKEY
https://orcid.org/0000-0001-9616-6889
*corresponding author: tugba.manici@sisli.edu.tr
[3]Physics, Faculty of Science, Istanbul University, İstanbul, TURKEY
https://orcid.org/0000-0002-4607-3382
[3]Physics, Faculty of Science, Istanbul University, İstanbul, TURKEY
https://orcid.org/0000-0003-1660-213X
[3]Physics, Faculty of Science, Istanbul University, İstanbul, TURKEY
https://orcid.org/0000-0001-6815-6384

(Received: 06.10.2023, Accepted: 04.04.2024, Published: 27.05.2024)

Abstract: Due to the harmful effects of ionizing radiation, shielding has become a crucial topic for radiation protection. Finding effective, non-toxic and low-cost shielding materials is imperative in ensuring the safety of individuals exposed to ionizing radiation. Whether a material is effective in shielding against radiation depends on the linear attenuation coefficient. In this study, linear attenuation coefficients were calculated using the MCNPX code for energy values of 81 keV (Ba-133), 140 keV (Tc-99m), 662 keV (Cs-137), 1173 keV, and 1332 keV (Co-60) by incorporating Bentonite Clay (BC) nanoparticles and micro-sized particles as additives into a Polyvinyl Alcohol (PVA) matrix. BC particles with a density of 50% were added to the PVA matrix using LAT and U cards. Simulations were performed with a mono-energetic source emitting 10^7 particles and a narrow beam geometry, and the counts of particles with diameters of 50 nanometers and 50 micrometers were calculated using the F4 tally. When the results obtained from the simulation were compared, it was observed that as the diameters of the added particles decreased, their effectiveness in radiation shielding increased for each energy value. Among them, the 50 nm BC particles added at a rate of 50% in PVA showed the highest effect at 1332 keV, with a 9.5% increase compared to 50 μm BC particles.

Key words: PVA, Bentonite Clay, Nanoparticles, Linear Attenuation Coefficient, MCNPX

1. Introduction

In recent years, the widespread use of radiation in various fields such as industry and medicine, coupled with the understanding of the potential biological effects resulting from exposure, underscores the importance of radiation protection. The realization that lead, commonly used in radiation shielding, can have toxic effects over time as a result of its interaction with radiation has led to a search for natural alternatives to lead. The pursuit of a new material that can provide effective radiation shielding while being easily obtainable, lighter, and more cost-effective than lead has kept research in this field current [1]. Additionally, studies have shown that nanoparticles are highly effective in radiation protection [2,3].

Due to the diversity of research topics, the use of mathematical approaches in radiation and materials science is increasingly on the rise. Among the various mathematical methods, Monte Carlo simulation stands out as one of the most preferred tools because

of its reliability and consistent approach, particularly when dealing with complex issues that may be difficult, expensive, or physically impossible to investigate experimentally. Dong et al. conducted research on the effects of nano-sized and micro-sized WO_3 particles added to E44 for gamma radiation shielding and found that nano-sized particles provided better radiation protection compared to micro-sized particles [4]. In another study, the mass attenuation coefficient of WO_3 added in nano and micro-sized particles within concrete was investigated using the MCNPX code, and it was observed that nano-sized particles provided the highest mass attenuation coefficient [5]. In a study conducted by Alavian at al., LDPE matrices were supplemented with W in four different sizes and at four different densities. Using the MCNP code, they investigated radiation shielding parameters and concluded that particle size had an inverse relationship with radiation shielding, and the ratio of the additive was a highly influential parameter [6]. In another study, Bi_2O_3 and WO_3 particles were examined within epoxy in nano and micro-sized using MCNP6, and similar results were obtained as in other studies [7].

Natural bentonite clays have also been investigated for their effectiveness in radiation shielding, in addition to heavy materials. Natural bentonite is derived from volcanic ash deposits formed as a result of volcanic eruptions and is naturally present at the nanometer scale. Furthermore, due to its high abundance and low cost, it is considered a good choice for this purpose [8,9,10]. In 2019, Hager et al. conducted experimental research on natural bentonite clays found in El Mutalla Mountain in Egypt, which naturally exist at the nanometer scale, under three different pressure values of 50, 100, and 150 bars, against 662 keV, 1173 keV, and 1332 keV gamma radiation. According to the Dynamic Light Scattering (DLS) measurement results of the obtained natural bentonite clay sample, the smallest size observed was 122 nm, representing 75% of the entire particle structure ranging from 122.4 to 220 nm. The study revealed that as the compression pressure of the bentonite clay increased, both density and linear attenuation coefficient also increased, with the highest linear and mass attenuation coefficients obtained under 150 bar pressure [8]. Elsafi at al. experimentally investigated the linear attenuation coefficients for four different bentonite clay samples at energies of 59 keV, 662 keV, 1173 keV, and 1332 keV gamma radiation. They concluded that natural bentonite clay provided the best shielding coefficient among the four different clays they studied, particularly at lower gamma energies [11].

Polyvinyl alcohol is an artificial polymer that has been used worldwide since the first half of the twentieth century, and it is produced from polyvinyl acetate through hydrolysis. It has been applied in various industries, including the industrial, medical, and food sectors, for the production of many end products such as resins, surgical threads, and food packaging materials that often come into contact with food [12,13]. The non-toxic and non-corrosive nature of PVA polymer, its water solubility, high optical transparency, and thermal stability make it a suitable matrix for optoelectronic and various other applications [14-16]. It has been demonstrated that a polymeric matrix containing suitable fillers exhibits favorable properties depending on the high surface area-to-volume ratio of the filler materials within the polymer matrix. An increase in the absorption/attenuation capabilities of a radiation shield is expected, while a decrease in the total weight is anticipated. Additionally, materials of this kind are expected to have higher compatibility and lower toxicity compared to lead [17,18].

In this study, the effects of changes in particle size on radiation shielding have been investigated. Polymeric matrix with a chemical formula of C_2H_4O and a density of 1.19 g/cm^3, PVA [19] was used. Bentonite clays with particle sizes of 50 nm and 50 μm were added to the PVA matrix at a density ratio of 50% using LAT and U cards. Monte Carlo Simulation with the MCNP code was employed to simulate and examine the radiation

shielding parameters at energies of 81 keV (Ba-133), 140 keV (Tc-99m), 662 keV (Cs-137), 1173 keV, and 1332 keV (Co-60) which are the most commonly used gamma energies in medical applications. Due to the awareness of the harmful effects of ionizing radiation used in medical applications, protecting and finding a better useful shielding materials from such radiation is crucial to prevent exposure outside of the procedures.

2. Material and Method

2.1 Theoretical Approach

The linear attenuation coefficient is calculated according to the Lambert-Beer law, which defines the attenuation of a mono-energetic beam as follows:

$$I = I_0 e^{-\mu x} \quad (1)$$

Here, I represents the gamma radiation intensity after passing through the target material, Io is the gamma radiation intensity from the source, x is the thickness of the absorbing medium, and μ is the linear attenuation coefficient [20] Unit of the μ is cm^{-1}.

The effectiveness of gamma radiation shielding is described in terms of the Half-Value Layer (HVL) and Tenth-Value Layer (TVL) of the attenuating material. The unit for HVL and TVL is cm. HVL is defined as the thickness of the absorber material that reduces the intensity of gamma radiation to half of its value:

$$HVL = \frac{Ln2}{\mu} \quad (2)$$

TVL, which depends on the absorber material and photon energy of radiation, is defined as the thickness of the absorber material that reduces the intensity of gamma radiation to one-tenth of its initial value [21]:

$$TVL = \frac{Ln10}{\mu} \quad (3)$$

MFP, which is defined as the average distance between consecutive interactions, is mathematically the inverse of the linear attenuation coefficient. The relationship with photon energy explains why the number of interactions increases as the distance between interactions decreases. The MFP (in cm) for the shielding material is calculated using the following equation [22]:

$$MFP = 1/\mu. \quad (4)$$

2.2. Monte Carlo Code

MCNPX (Monte Carlo N-Particle eXtended) is a code developed at the Los Alamos National Laboratory to simulate the behavior of particles such as neutrons, photons, electrons, and other particle types. The MCNPX code is based on the Monte Carlo method, which involves simulating the behavior of particles by tracking their interactions and movements through a defined geometry [23]. The code uses probability distributions and statistical methods to model physical processes that particles undergo, such as scattering, absorption, and nuclear reactions [5,24]. During this study, the simulation was run in photon mode only.

The simulation was carried out using LAT, U, SDEF, AXS, POS, PAR, ERG, and CELL cards. To determine the linear attenuation coefficient of the PVA/BC mixture against photons, mono-energetic beams were simulated. The selection of mono-energetic beams were from gamma-emitting radioactive sources, including 81 keV (Ba-133), 140 keV ($Tc\text{-}99^{m}$), 662 keV (Cs-137), 1173 keV, and 1332 keV (Co-60).

For the simulation with a narrow beam geometry, a spherical source with a 3 mm radius, lead collimators, and a target were set up as shown in Figure 1. The photon source is located within a cylindrical lead collimator with a radius of 3 mm and a length of 40 cm. The detector is positioned 43 cm away from the source on the same axis and has dimensions of 3x3x4 cm^3. The detector collimator is made of lead, with a diameter of 4.5 cm and a length of 10 cm. The modeled nano and micro-sized shielding materials were placed 40 cm away from the source, and they had dimensions of $4 \times 4 \times 0.2$ cm^3. Equation 5 was used for density calculations of the materials:

$$\frac{100}{\frac{m}{\rho_m} + \frac{f}{\rho_f}} \tag{5}$$

Here, m represents the percentage of the matrix, ρ_m is the density of the matrix material, f represents the percentage of the filler material, and ρ_f is the density of the filler material. The density of the new material consisting of a 50% PVA - 50% BC mixture is 1.6844 g/cm^3.

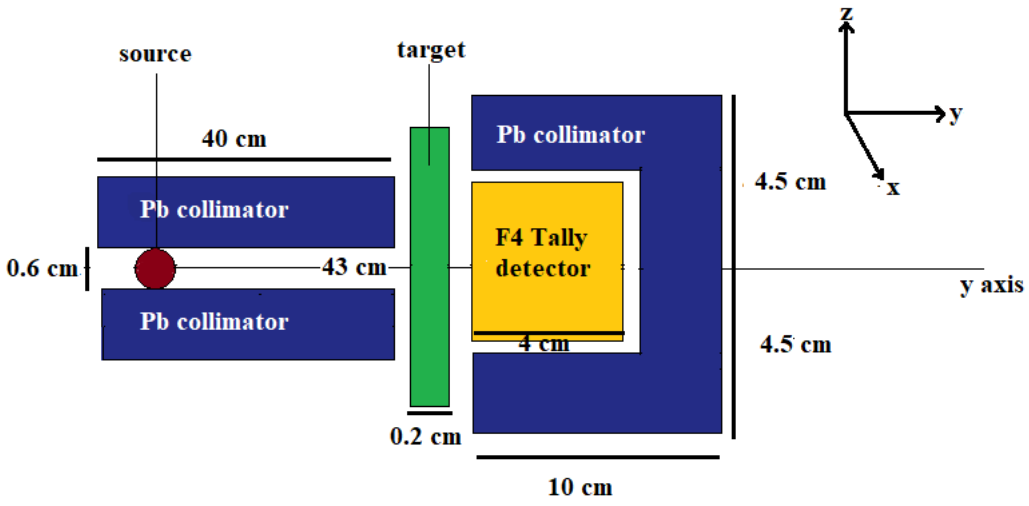

Figure 1. Schematic View of Simulation Geometry

2.2.1. Design of Nano and Micro Particles in the Matrix

In this study, nano and micro particles were placed in the PVA matrix using lattice cards. The filler materials consisting of nano and micro-sized bentonite clays were defined within the PVA matrix as spheres located at the centers of cubes. Each micro and nano particle in the study was designed to have sizes of 50 micrometers and 50 nanometers, respectively. In Figure 2, an arrangement example for a 50% weight fraction is shown.

For the PVA matrix with 50% fraction of BC micro and nano particles, the size of each lattice cell was L, which is 1.4205×10^{-02} cm and 1.4205×10^{-05} cm, respectively. The F4 tally was used in the simulation to calculate the photon flux in the detector cell.

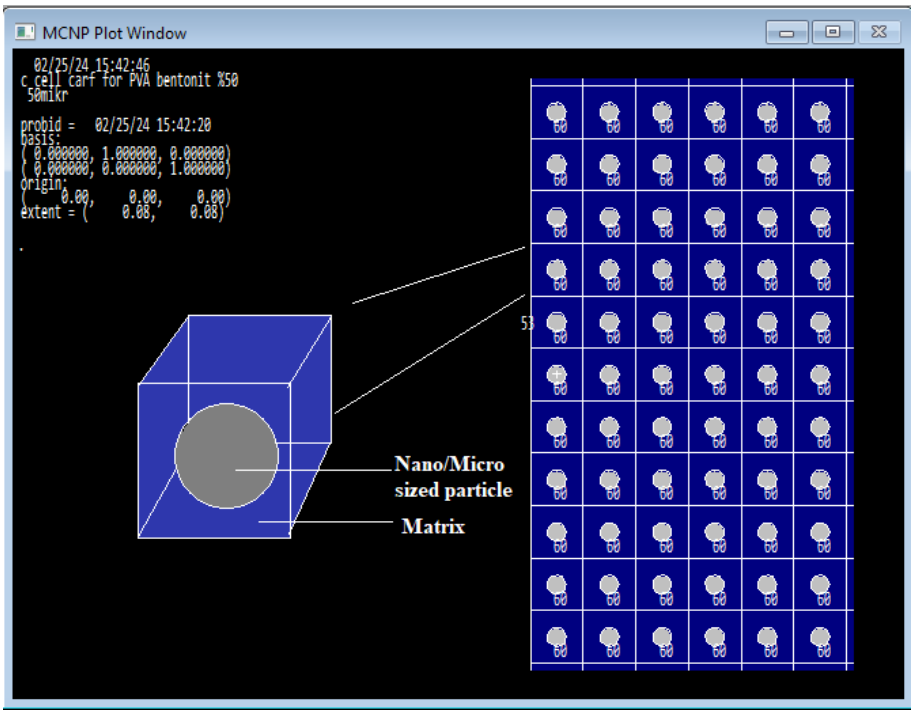

Figure 2. MCNP Screenshot of Nano/Micro BC Particles in PVA Matrix

As seen in Figure 3, the equidistant spacing between particles with a homogeneous distribution within the matrix is defined as "a." For the PVA matrix with a %50 density ratio of 50 nm diameter added particles, the distance "a" between two particles is $9.2054x10^{-06}$ cm. For particles with a diameter of 50 μm added to the matrix, the distance "a" between two particles is $9.2054x10^{-03}$ cm.

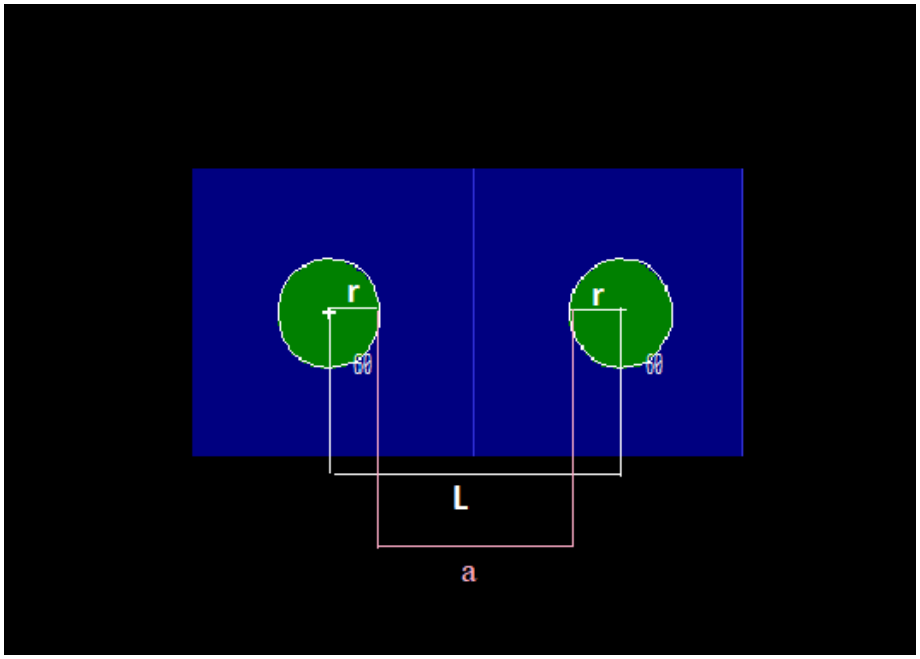

Figure 3. Inter-particle Distance Representation

The F4 tally evaluates the number of photons entering a cell in MeV/cm^2. The relative statistical errors of the MC results are less than %1 [25]. Table 1 contains the elemental weight fractions of bentonite clay and PVA used in the simulation. These data were used for material definitions in the simulation [19,26].

Table 1. Elemental Mass Fractions Used in MCNPX

	Bentonite Clay	**PVA**
Density	2.881 g/cm^3	1.19 g/cm^3
H	0.007977	0.091520
C	-	0.545296
O	0.525272	0.363184
Na	0.012504	-
Mg	0.018654	-
Al	0.088209	-
Si	0.308240	-
P	0.000130	-
K	0.004445	-
Ca	0.010133	-
Ti	0.000832	-
Mn	0.000998	-
Fe	0.022607	-

3. Results

3.1. MCNPX and XCOM Validation

In order to test the reliability of the results obtained with the geometry designed using the Monte Carlo code, the linear attenuation coefficients of pure PVA (C_2H_4O) polymer were calculated using the MCNPX code at different energy values. The linear attenuation coefficients obtained at 81 keV, 140 keV, 662 keV, 1173 keV, and 1332 keV energies were compared with the National Institute of Standards and Technology (NIST) data [27]. As shown in Table 2 , there is a close agreement between the Monte Carlo results and the NIST data. The maximum approximate difference between Monte Carlo and NIST values is about %0.49. Therefore, the created Monte Carlo model has been validated for further simulations in the study.

Table 2. MCNPX AND XCOM Values of Linear Attenuation Coefficients of PVA (d=1.19 g/cm^3) and % Difference Between the Results

Energy (keV)	**μ-XCOM(1/cm)**	**μ-MCNPX (1/cm)**	**% DIFFERENCE**
81	0.2099	0.2094	0.2382
140	0.1787	0.1783	0.2238
662	0.1001	0.0996	0.4995
1173	0.0762	0.0761	0.1312
1332	0.0714	0.0712	0.2801

3.2. Comparison between MCNPX and Other Studies

The study conducted by Elsafi and colleagues involved four types of clay: Red, ball, kaolin, and bentonite, obtained from stone quarries in the Aswan, Abuznima, and Fayoum governorates of Egypt. These samples were sieved to a size of 100 μm, mixed thoroughly with water, divided into slices, and then dried in the sun to obtain them. Subsequently, they obtained linear attenuation coefficients for 662 keV, 1173 keV, and 1332 keV gamma sources. Table 3 shows the linear attenuation coefficients for these four different types of clay and, additionally, the linear attenuation coefficients for ordinary concrete as found in the study by Cape Town for bentonite clay and in Bashter's study [28] for ordinary concrete. Figure 4 presents a comparison of the data from Table 3.

Table 3. Comparison of Linear Attenuation Coefficients of Pure Bentonite Clay with Previously Published Data

ENERGY (KEV)	LAC (1/cm)					
	RED CLAY	BALL CLAY	KAOLIN CLAY	BENTONITE CLAY	ORDINARY CONCRETE	THIS STUDY (BC)
	[11]	[11]	[11]	[11]	[28]	MCNPX
81	-	-	-	-	-	0.5762
140	-	-	-	-	-	0.4199
662	0.1608	0.1524	0.1525	0.1608	0,1513	0.2222
1173	0.1224	0.1161	0.1161	0.1221	0.1366	0.1695
1332	0.1101	0.1087	0.1088	0.1146	0.1279	0.1587

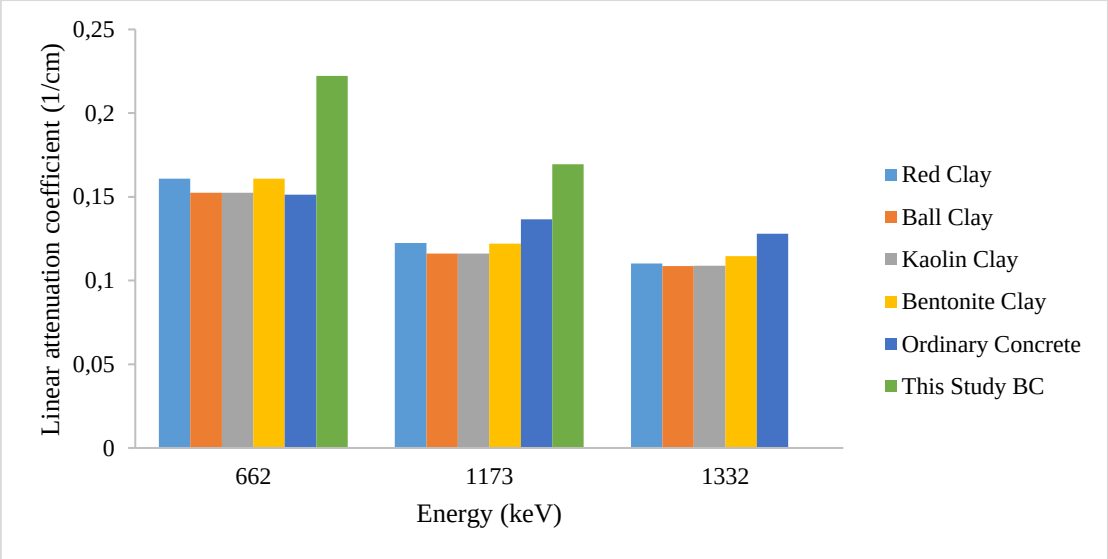

Figure 4. Comparison of Linear Attenuation Coefficients of Pure Bentonite Clay with Previously Published Data

3.3. The Effect of Particle Size on Linear Attenuation Coefficients

Table 4 presents the calculated linear attenuation coefficients for samples of bentonite clay added to PVA with a 50% weight ratio at 81, 140, 662, 1173, and 1332 keV gamma energies, along with the percentage difference between nano and micro-sized particles. When looking at Figure 5, which contains separate comparisons for each energy value, it can be observed that for the same proportion of added BC, the linear attenuation coefficient increases as the particle size decreases. The increased linear attenuation coefficients due to a decrease in particle size exhibit the same increasing trend for each energy. The highest linear attenuation coefficient was obtained for nano-sized BC added at 81 keV energy, with a value of 0.230 cm^{-1}. When considering the exchange between nano and micro particles at the same energy values, the highest difference occurs at 1332 keV with a percentage difference of %8.974. In Table 5, the linear attenuation coefficients and percentage differences are presented for pure PVA and PVA with nano-sized BC added at the same energies. Here, the addition of nano-sized BC results in an increase in the linear attenuation coefficient for each energy value, with the highest difference observed at 662 keV with a percentage difference of %15.384.

Figure 6 compares the linear attenuation coefficients of pure PVA, PVA with 50 nm-BC added at a 50% ratio, and PVA with 50 μm-BC added at a 50% ratio. It can be observed that nano-sized BC added provides the highest effect among these materials in terms of linear attenuation coefficients.

Table 4. Comparison of Linear Attenuation Coefficients and Percentage Difference Values of BC's Micro and Nano Samples at Different Photon Energies (keV)

ENERGY (keV)	μ-LAC (%50 PVA+50 μm BC)	μ-LAC (%50 PVA+50 nm BC)	% DIFFERENCE
81	0.221	0.230	3.913
140	0.180	0.191	5.759
662	0.114	0.117	2.564
1173	0.075	0.078	3.846
1332	0.071	0.078	8.974

Table 5. Comparison of Linear Attenuation Coefficients and Percentage Difference Values of BC's Nano Samples and Pure PVA at Different Photon Energies (keV).

ENERGY (keV)	μ-LAC (PURE PVA)	μ-LAC (%50 PVA+50 nm BC)	% DIFFERENCE
81	0.209	0.230	9.130
140	0.178	0.191	6.806
662	0.099	0.117	15.384
1173	0.075	0.078	3.846
1332	0.071	0.078	8.974

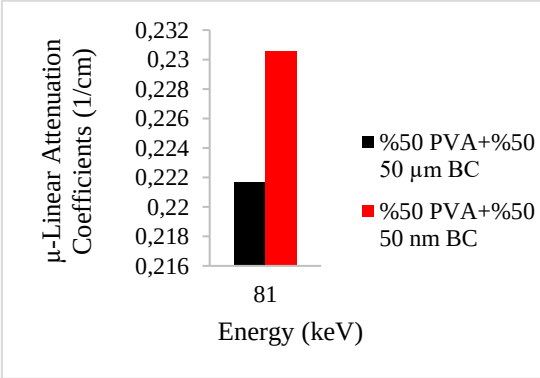

(a)

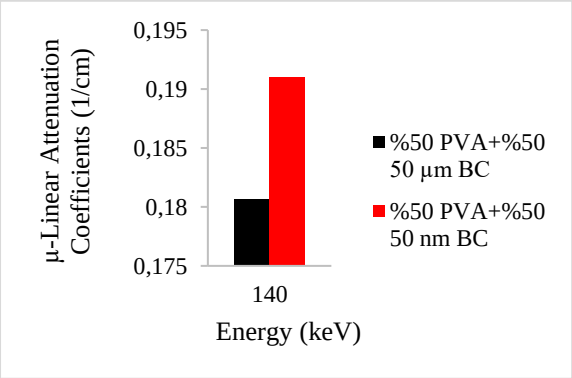

(b)

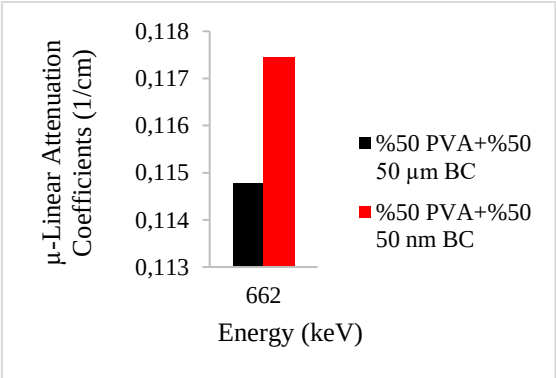

(c)

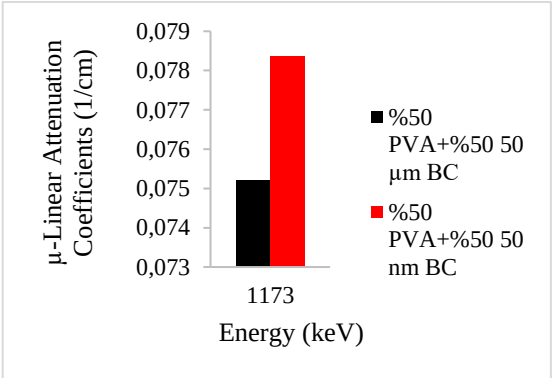

(d)

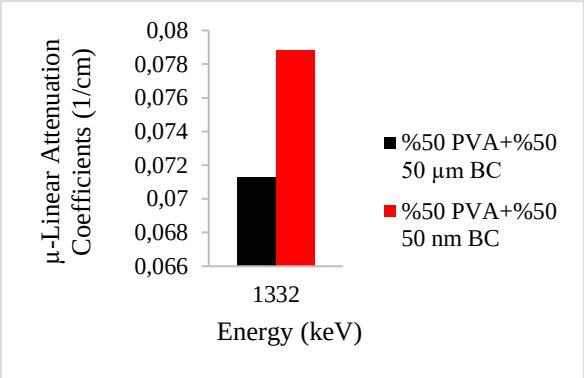

(e)

Figure 5. Comparison of Linear Attenuation Coefficient of Micro and Nano Samples for Photon Shielding at Different Energy Levels (keV)

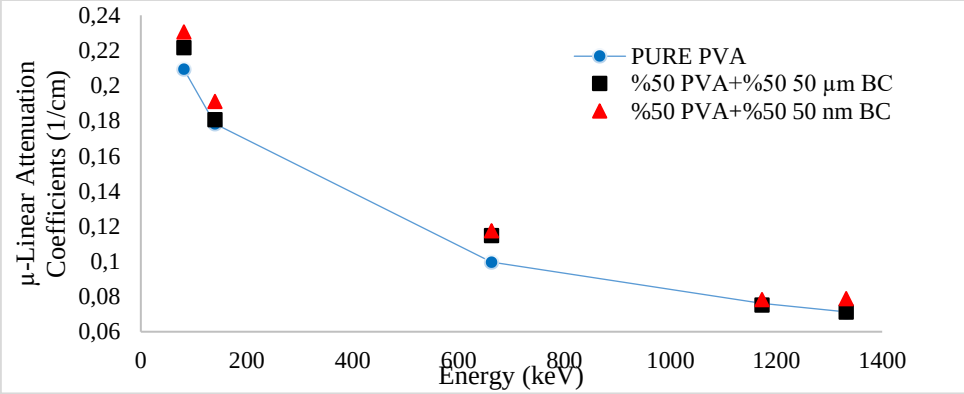

Figure 6. Linear Attenuation Coefficients of New Materials Created by Adding Pure PVA and 50% Nano and Micro Sized BC Particles into the PVA Matrix

3.4. MFP, HVL, and TVL Values

The MFP, HVL and TVL values for the 50 nm-BC and 50 μm-BC materials added to PVA in this study are presented in Figure 8.

The MFP value increases with energy because lower-energy photons can lose their energy over short distances, while higher-energy photons require larger distances to lose their energy. As shown in Figure 7 (a), the highest MFP value is achieved with micro-sized BC at 1332 keV energy. HVL is an essential parameter for radiation shielding materials, and the effectiveness of a shielding material against radiation is inversely proportional to its HVL. Figure 7 (b) displays HVL values for PVA with nano and micro-sized BC. Here, micro-sized BC exhibits the highest HVL value at 1332 keV. Figure 7 (c) illustrates the TVL values. Similar to HVL, micro-sized BC added to PVA provides the highest TVL value at 1332 keV.

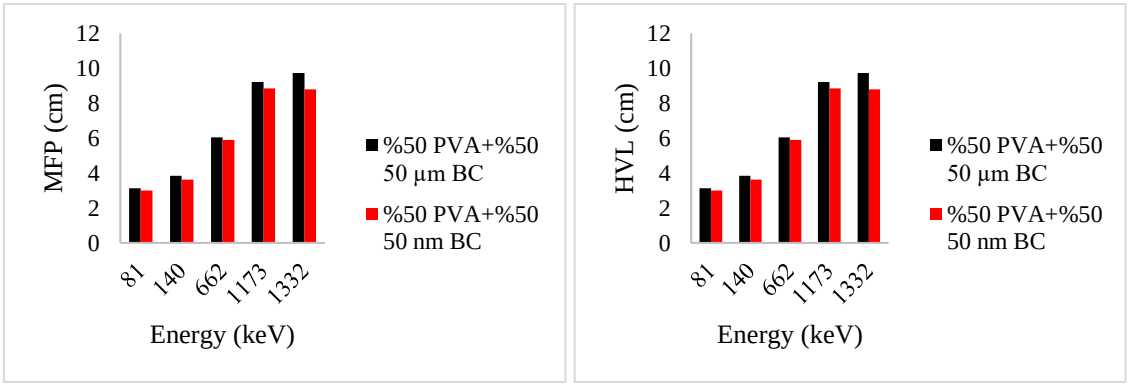

(a) **(b)**

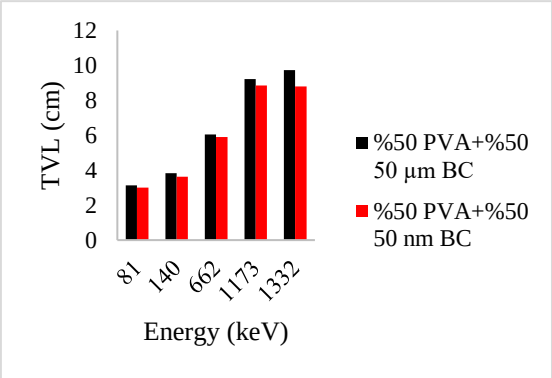

(c)

Figure 7: Energy-Dependent Changes of MFP (a), HVL (b) And TVL (c) for PVA/Bentonite Clay Forms Created with Nano/Micro Additives

4. Discussion and Conclusion

The Bentonite Clay simulated during this study was obtained from Cape Town [27] and effects of this BC on radiation protection has not been investigated before, and no previous study has examined the change in linear attenuation coefficient with particle size. To validate this simulation, linear attenuation coefficient values for pure PVA were calculated and compared with the theoretical results from XCOM NIST, demonstrating the accuracy of the simulation with a 0.43% error margin. During this study, BC was added to PVA to create a homogeneous distribution with a weight fraction of %50 and particle sizes of 50 nm and 50 µm to investigate the effect of particle size and LAC, HVL, MFP, and TVL values were investigated using MCNPX for mono-energetic gamma sources at 81 keV, 140 keV, 662 keV, 1173 keV, and 1332 keV. In [11], gamma energies of 662, 1173, and 1332 keV were investigated, while in this study, the energy range was extended to include 81 keV and 140 keV where photoelectric effect is dominant as a interaction type of matter with photons. Table 3 presents linear attenuation coefficients of four different clays obtained in [11] with LACs for ordinary concrete from [27], and LACs for the BC used in this study are also included. At 662 keV gamma energy, [11] reported that the LACs of Bentonite Clay and Red Clay are equal, and both clays have higher LAC values compared to the other two clays. When compared to ordinary concrete, all clays provide approximately %5.9 better protection at this energy. However, BC used in this study, shows a %27 higher LAC value compared to ordinary concrete. At 1173 keV gamma energy, [11] reported that red clay has the highest LAC value among the clays, but ordinary concrete has a %10.3 higher LAC value compared to red clay. When compared to ordinary concrete, the BC used in this study is approximately %19 more effective. At 1332 keV gamma energy, [11] reported that bentonite clay has the highest LAC value among the clays, while ordinary concrete has a %10.3 higher LAC value compared to bentonite clay. According to the results of this study, it is approximately 19% more effective than ordinary concrete. Table 3 and Figure 4 show that the BC from Cape Town has the highest impact among the energies studied. The fact that bentonite clay samples sometimes show protection performance similar to or even higher than common radiation shields demonstrates their potential in shielding applications. The results show that the highest linear attenuation coefficient is obtained in terms of particle size, in the nano size, and this continues for each energy value. It is because of the materials at the nanometer scale have a significantly larger surface area compared to micro-sized particles with the same mass or volume. This increased surface area provides more opportunities for interactions with radiation, enhancing both scattering and absorption chances, making it highly suitable for gamma ray protection. Due to the results of LAC, the highest HVL value is provided by micro-sized BC at 1332 keV. Since high energy already requires the protective shield to be thicker than low

energies, the shield made with nm-BC is thinner than the shield prepared with μm-BC, as shown in Figure 6. Similar results can be seen for TVL and MFP values in Figure 7 (b)-(c).

As a conclusion, due to its superior performance compared to commonly used concrete for shielding, this clay sample is considered suitable for use as a radiation shielding material by incorporating it into different scenarios. Additionally, using it in nanometer size enhances its effectiveness in protection against gamma radiation. Considering its abundance, applicability, and cost-effectiveness, this material can be utilized in various fields where radiation shielding is required.

Authorship contribution statement

T.Manici: Conceptualization, Methodology, MCNP Simulation, Data Curation, Original Draft Writing; **B.Demir**: Conceptualization, Methodology, Visualization, Supervision, Observation, Advice; **N.Akçay, G.Algün**: Visualization, Supervision, Observation, Advice.

Declaration of competing interest

The authors declare that they have no known competing financial interests or personal relationships that could have appeared to influence the work reported in this paper.

Ethics Committee Approval and/or Informed Consent Information

As the authors of this study, we declare that we do not have any ethics committee approval and/or informed consent statement.

References

[1] M. Asgari, H. Afarideh, H. Ghafoorifard, E. A. Amirabadi, ‘‘Comparison of nano/micro lead, bismuth and tungsten on the gamma shielding properties of the flexible composites against photon in wide energy range (40 keV–662 keV)’’, *Nuclear Engineering and Technology*, 53, 4142-4149, 2021.

[2] S. Nambiar, J. T. W. Yeow, ‘‘Polymer-Composite Materials for Radiation Protection’’, *ACS Applied Materials & Interfaces*, 4, 5717−5726, 2012.

[3] C. Song, J. Zheng, QP. Zhang, YT. Li, YJ. Li, Y. Zhou, ‘‘Numerical simulation and experimental study of PbWO4/EPDM and Bi2WO6/EPDM for the shielding of γ-rays’’, *Chinese Physics C*, 40(8), 089001, 2016.

[4] Y. Dong, SQ. Chang, HX. Zhang, C. Ren, B. Kang, MZ. Dai, YD. Dai, ‘‘Effects of WO3 Particle Size in WO3/Epoxy Resin Radiation Shielding Material’’ *Chinese Physics Letters,* 29(10), 108102, 2012.

[5] H.O. Tekin, V.P. Singh, T. Manici, ‘‘Effects of micro-sized and nano-sized WO3 on mass attenauation coefficients of concrete by using MCNPX code’’, *Applied Radiation and Isotopes*, 121, 122-125, 2017.

[6] H. Alavian, H. Tavakoli-Anbaran, ‘‘Study on gamma shielding polymer composites reinforced with different sizes and proportions of tungsten particles using MCNP code’’, *Progress in Nuclear Energy*, 115, 91–98, 2019.

[7] Y. Karabul, O. İçelli, ‘‘The assessment of usage of epoxy based micro and nano-structured composites enriched with Bi2O3 and WO3 particles for radiation shielding’’, *Results in Physics*, 26, 104423, 2021.

[8] I. Z. Hager, Y. S. Rammah, H. A. Othman, E. M. Ibrahim, S. F. Hassan, F. H. Sallam, ‘‘Nano-structured natural bentonite clay coated by polyvinyl alcohol polymer for gamma ray attenuation’’, *Journal of Theoretical and Applied Physics*. 13, 141–153, 2019.

[9] M. M. Bani-Ahmad, N. Z. N. Azman, J. N. Z. Jasmine, H. M. Almarri, M. Alshipli, M. R. Ramzun, ‘‘Radiation attenuation ability of bentonite clay enriched with eggshell as recyclable waste for a physical rradiation barrier’’, *Radiation Physics and Chemistry*, 201, 110484, 2022.

[10] R. S. Özakar, M. Kara, A. Maman, ‘‘Preparation, characterization, and radiation absorption study of bentonite clay included soft chewable lozenge formulations’’, *Journal of Pharmaceutical Technology* 1(3), 54-59, 2020

[11] M. Elsafi, Y. Koraim, M. Almurayshid, F. I. Almasoud, M. I. Sayyed, I. H. Saleh, ‘‘Investigation of Photon Radiation Attenuation Capability of Different Clay Materials’’, *Materials*. 14, 6702, 2021.

[12] F. Sallam, E. Ibrahim, S. Hassan, A. Omar, ‘‘Shielding properties enhancement of bentonite clay nano particles coated by polyvinyl alcohol polymer’’, *Research Square*, 2021.
[13] T. S. Gaaz, A. B. Sulong, M. N. Akhtar, A. A. Kadhum, A. B. Mohamad, A. A. Al-Amiery, ‘‘Properties and Applications of Polyvinyl Alcohol, Halloysite Nanotubes and Their Nanocomposites’’, *Molecules*. 20, 22833–22847, 2015.
[14] M. Aslam, M. A. Kalyar, Z. A. Raza, ‘‘Polyvinyl Alcohol: A Review of Research Status and Use of Polyvinyl Alcohol Based Nanocomposites’’, *Polymer Engineering and Science*, 58, 2119-2132, 2018.
[15] G. B. Pour, L. F. Aval, M. Mirzaee, ‘‘Flexible graphene supercapacitor based on the PVA electrolyte and BaTiO3/PEDOT:PSS composite separator’’, *Journal of Materials Science:Materials in Electronics*, 29, 17432–17437, 2018.
[16] L. F. Aval, M. Ghoranneviss, G. B. Pour, ‘‘High performance supercapacitors based on the carbon nanotubes, graphene and graphite nanoparticles electrodes’’, *Heliyon*, 4, e00862, 2018.
[17] L. Chang, Y. Zhang, Y. Liu, J. Fang, W. Luan, X. Yang, W. Zhang, ‘‘Preparation and characterization of tungsten/epoxy composites for γ-rays radiation shielding’’, *Nuclear Instruments and Methods in Physics Research Section B*, 356–357, 88-93, 2015.
[18] S. Malekie, N. Hajiloo, ‘‘Comparative Study of Micro and Nano Size WO3/E44 Epoxy Composite as Gamma Radiation Shielding Using MCNP and Experiment’’, *Chinese Physics Letters*, 34, 108102, 2017.
[19] F. Kazemi, S. Malekie, M. A. Hosseini, ‘‘A Monte Carlo Study on the Shielding Properties of a Novel Polyvinyl Alcohol (PVA)/WO3 Composite, Against Gamma Rays, Using the MCNPX Code’’, *Journal Of Biomedical Physics & Engineering*, 9(4), 465-472, 2019.
[20] S. El-Fiki, S. U. El Kameesy, D. E. El. Nashar, M. A. Abou- Leila, M. K. El-Mansy, M. Ahmed, ‘‘Influence of Bismuth Contents on Mechanical and Gamma Ray Attenuation Properties of Silicone Rubber Composite’’, *International Journal of Advanced Research*, 3, 1035-1039, 2015.
[21] H. O. Tekin, V. P. Singh, U. Kara, T. Manici, E. E. Altunsoy, ‘‘Investigation of Nanoparticle Effect on Radiation Shielding Property Using Monte Carlo Method’’, *CBU Journal of Science*, 12 (2), 195-199, 2016.
[22] R. Bagheri, A. K. Moghaddam, H. Yousefnia, ‘‘Gamma Ray Shielding Study of Barium–Bismuth–Borosilicate Glasses as Transparent Shielding Materials using MCNP-4C Code, XCOM Program, and Available Experimental Data’’, *Nuclear Engineering and Technology*, 9, 216-223, 2017.
[23] MCNPX 240, Monte Carlo N-Particle Transport Code System for Multiparticle and High Energy Applications (Sep 2004). Bibliographic information available from INIS: http://inis.iaea.org/search/search.aspx?orig_q=RN:39098954 Available on-line: http://www.nea.fr/abs/html/ccc-0715.html
[24] K. Verdipoor, A. Alemi, A. Mesbahi, ‘‘Photon mass attenuation coefficients of a silicon resin loaded with WO3, PbO, and Bi2O3 Micro and Nano-particles for radiation shielding’’, *Radiation Physics and Chemistry*, 147, 85–90, 2018.
[25] J. K. Shultis, R. E. Faw, ‘‘An MCNP Primer’’, *Dept. of Mechanical and Nuclear Engineering Kansas State University Manhattan*, KS 66506.
[26] M. Vhahangwele, G. W. Mugera, N. Tholiso, ‘‘Defluoridation of drinking water using Al3+-modified bentonite clay: optimization of fluoride adsorption conditions’’, Toxicological & Environmental Chemistry, 96(9), 1294-1309, 2014.
[27] M.J. Berger, J.H Hubbell, S.M. Seltzer, J. Chang, J.S. Coursey, R. Sukumar, D.S. Zucker, K. Olsen, XCOM: Photon Cross Section Database. National Institute of Standards and Technology (NIST). Published 2010. Available online: http://physics.nist. gov/xcom.
[28] I. I. Bashter, ‘‘Calculatıon of Radıatıon Attenuatıon Coefficıents For Shıeldıng Concretes’’, *Annals of Nuclear Energy*, 24 (17), 1389-1401, 1997.

Süleyman Demirel Üniversitesi Fen Edebiyat Fakültesi Fen Dergisi https://dergipark.org.tr/sdufeffd
Süleyman Demirel University Faculty of Arts and Sciences Journal of Science e-ISSN: 1306-7575
Research Article, 2024, 19(1): 75-85, DOI: 10.29233/sdufeffd.1364481

Investigating Thermal Neutron and Gamma Ray Shielding Properties of Al Matrix Gd_2O_3- and W-Doped Composites Using Monte Carlo Simulations

Yasin GAYLAN[1] and Ahmet BOZKURT[2]

[1]*Department of Medical Imaging Techniques, Zonguldak Bülent Ecevit University, 67100 Zonguldak, Turkey*
https://orcid.org/0000-0003-1354-7593
[2] *Department Of Computational Science And Engineering, Istanbul Tecnical University, 34469 Istanbul, Turkey*
https://orcid.org/0000-0002-3163-0131

(Received: 21.09.2023, Accepted: 16.04.2024, Published: 27.05.2024)

Abstract: This study aimed to calculate the thermal neutron (0.0253 eV) total macroscopic cross-section and gamma-ray (1.25 MeV) linear absorption coefficient for (100-x)Al-xGd_2O_3 (x=5 to 50) and 100-(x+y)Al-xGd_2O_3+yW (x,y=5 to 50) composites using MCNP6.2 simulation code. The simulation consists of a mono-energy point neutron and gamma-ray source, target material, and detector. The F4 tally from the MCNP6.2 library was used as the detector. The results show the highest thermal neutron total macroscopic cross-section for the 50%Al-50%Gd_2O_3 composite and the highest linear absorption coefficient for the 50%Al-%5Gd_2O_3-45%W composite. The results of this study provide a good understanding of the thermal neutron and gamma ray the shielding capabilities of Al matrix Gd_2O_3 and W doped composites.

Keywords: Al-Gd_2O_3-W composites, Neutron shielding, Gama shielding, Monte Carlo simulations

1. Introduction

Neutrons are used or emitted in nuclear power plants (during power generation and in fuel waste), particle accelerators, neutron imaging devices, elemental analysis and some biological applications [1–6]. Since neutrons have a net electric charge of zero, they do not enter into Coulomb interactions and interact with matter only at short distances (less than 1 fm) where the strong nuclear force is effective. For this reason, they can easily penetrate matter. Neutrons, depending on their energy, have a higher Relative Biological Effect and Radiation Weight Factor [7,8] compared to other types of ionizing radiation (p, α, γ, β-, β+). This makes neutron shielding a very important task when protecting workers and equipment in areas where neutron flux is present [9]. Neutron shields should be designed according to the restrictions and requirements of a specific usage [10–13]. Depending on their location/usage, neutron shielding properties, such as strength, portability, or heat resistance, become important [14].

Due to the high neutron absorption cross-section of the ^{10}B isotope, boron-containing materials have been widely studied to shield neutrons emitted during the storage and transport of spent fuel in dry storage casks or wet storage pools. Since B_4C cannot be formed into sheets due to its brittleness, it is produced as an aluminum-boron carbide (Al-B_4C) composite as a high-performance neutron shielding [15–18]. Studies show that the hardness as well as the neutron cross section of the Al-B_4C composite increases as the B_4C ratio increases and the machinability of the composite decreases. [19–23]. Therefore, literature studies suggest Al-30%B_4C composite as the ideal Al-B_4C composite ratio. [24,25]. In addition, the corrosion rate of neutron shielding increases

with increasing B_4C content in the composite as helium bubbles are generated due to the 10B(n, α) reaction. [26].

Therefore, rare earth elements with high neutron absorption cross-section, such as cadmium (Cd, 2520 barn), gadolinium (Gd, 49700 barn), samarium (Sm, 5922 barn), or europium (Eu, 4530 barn), have been utilized to enhance the absorption cross-section and ductility of Al-B_4C composites [27–29]. Among these elements, Gd has the highest thermal neutron absorption cross-section, so it has been widely studied to develop neutron shielding. Additionally, since Gd undergoes the (n, γ) reaction, it does not cause corrosion processes caused by the (n, α) reaction.

Xu et al. developed Al-(15%B_4C+1%Gd) composite as an alternative to Al-30%B_4C composite for shielding against thermal neutrons (0.0253 eV) [30]. They reported that reducing the B_4C ratio from 30% to 15% in the B_4C-Al composite and replacing it with 1%Gd increased its thermal neutron macroscopic cross-section from 24.9 cm^{-1} to 27.4 cm^{-1} and the elongation from 4% to 9%. Jiang et al. produced 6061Al-(1%Gd+15%B_4C) composite using vacuum hot pressing and hot rolling methods to enhance the ductility of spent fuel storage [31]. They reported that the mechanical properties of the composites were improved by the homogeneous distribution of Gd in the matrix. Moreover, the relationship between its fracture energy and the neutron total macroscopic cross-section exhibited a better performance than the B_4C/Al composites reported in the literature [22–24,32,33].

Since pure Gd is easily oxidized and very costly, Gd_2O_3 is an alternative. Zhang et al. obtained the neutron macroscopic cross-section of 6061Al-10%Gd_2O_3 and 6061Al-30%B_4C composites as Σ = 5.1 cm^{-1} and Σ=5.5 cm^{-1} respectively, in their study with neutrons of 0.2 eV energy. While the tensile strength values of both composites were equal (240 Mpa), the tensile strain increased from 4% in 6061Al-30%B_4C composite to 16% in 6061Al -10%Gd_2O_3 [34]. Cong et al. produced (100-x)%Al-x%Gd_2O_3 (x = 7, 15, 25, and 35) composites via powder metallurgy method with a cold isostatic press. The produced composites exhibited higher total macroscopic cross-section values for neutrons of 0.0253 eV energy than the Al-30%B_4C composite. Additionally, the thermal efficiency of the composite improved with increasing sintering time [35].

In order to absorb secondary gamma rays from the neutron absorption reaction, the neutron shielding is doped with elements with high gamma-ray linear attenuation coefficient. In comparison to lead (Pb) and bismuth (Bi) in neutron shielding [36], tungsten (W) stands out for gamma-ray absorption. In addition to its physical and mechanical properties, W is non-toxic, like Pb [37,38]. It also exhibits a higher thermal neutron absorption cross section (18.3 barn) than Pb (0.171 barn) [39].

Cong et al. examined Al-25%Gd_2O_3-x%W (x = 7, 15, 25 and 35) [40] composites as an alternative to Al-30%B_4C composite. They showed that Al-25%Gd_2O_3-25%W composite has a hardness value (88 HV) close to Al-30%B_4C composite, while thermal neutron and gamma-ray shielding properties are much better.

Researchers aiming to develop next-generation neutron shielding should address the following key questions when evaluating the Al-Gd_2O_3-W composite: whether its thermal neutron cross-section, gamma ray shielding properties (LAC, HVL, and TVL), and mechanical properties are

suitable.The composite with an optimal mixture ratio for these three properties is preferred as a suitable neutron shield. This study seeks to answer the first two questions to provide design concepts for Al-Gd_2O_3-W composites. In the simulation study, thermal neutron total macroscopic cross-section and LAC, HVL , TVL of 1.25 MeV gamma-rays were calculated for (100-x)Al-xGd_2O_3 (x=5 to 50) and 100-(x+y)Al-xGd_2O_3+yW (x,y=5 to 50) composites using the MCNP6.2 simulation code. This study is expected to guide the exploration of Al matrix Gd_2O_3- and W-doped composites, characterized by high strength and plasticity, by considering the thermal neutron cross-section and gamma-ray LAC, HVL and TVL values of Al-Gd_2O_3-W composition.

2. Materials and method

2.1 Monte Carlo simulations

This study used the Monte Carlo method to calculate the thermal neutron total macroscopic cross-section and gamma-ray shielding properties (LAC, HVL, and TVL). The radiation transport package MCNP6.2 simulation code is a Monte Carlo program that can simulate the transportation of neutrons, electrons, and photons through materials [41]. It was developed at Los Alamos National Laboratory for general-purpose radiation interactions. In the literature, MCNP has been used to calculate the radiation protection performance of various materials, such as concretes [42], glasses [43], and metal composites [33]. Simulation calculations for radiation shielding calculations are widely used in the literature [44–47].

As shown in Fig. 1, the simulation geometry consists of a mono-energetic point neutron/gamma-ray source placed in a cylindrical cavity, a target material in the form of a disk, and a cylindrical detector volume to measure the particle flux through the absorbing material. The thermal neutron energy is defined as $2.53*10^{-8}$ MeV, and the gamma-ray energy is defined as 1.25 MeV. The photon significance was set to zero (0) for thermal neutron total macroscopic cross-section calculations to shorten the simulation time. The detector flux was calculated using the F4 tally of MCNP6.2 simulation code, which measures the average flux in a cell per cm^2. To reduce statistical error, the simulations generated 10^8 histories (neutrons and gamma-rays) and the statistical error was below 1%.

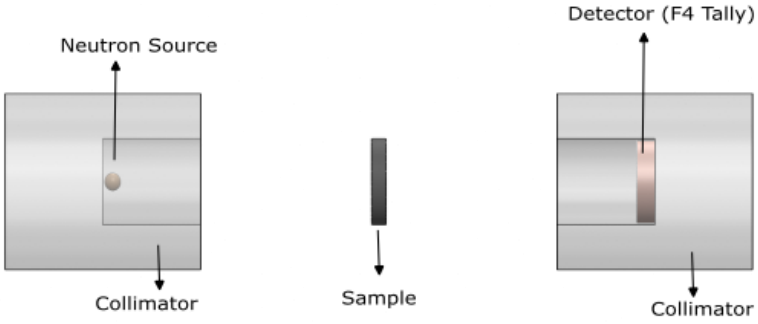

Figure 1. Geometrical setup for the monte carlo simulations

2.2 Calculation of total macroscopic cross-section (Σ_t) for neutrons

As neutrons pass through the matter, scattering or absorption reaction occurs, depending on their energy and the nucleus that makes up the matter. The neutron can perform nuclear fission, neutron capture, inelastic scattering, and elastic scattering reactions with the nucleus with which it interacts. The sum of the probability of neutron interacting with matter through the mentioned absorption σ_a and scattering σ_s reactions is defined as the total microscopic cross-section σ_t.

$$\sigma_t = \sigma_a + \sigma_s \quad (1)$$

When neutrons pass through a medium, the probability of scattering and absorption does not depend only on the microscopic scattering and absorption cross-section. The density of nuclei in the medium also affects the probability of the neutron passing through the medium and interacting. The microscopic cross-section and the density of nuclei in the medium are expressed by a physical quantity called the total macroscopic cross-section and is denoted by Σ_t [48];

$$\Sigma_t = N\sigma_t \quad (2)$$

N is the number of nuclei per unit volume, and the unit of Σ_t is cm^{-1}.

The total macroscopic cross-section of a material consisting of different nuclei is calculated as follows:

$$\Sigma_t = N_a\sigma_a + N_b\sigma_b + N_c\sigma_c + \cdots \quad (3)$$

The Σ_t value of a material is calculated using the Beer-Lambert law as follows [49];

$$I_x = I_0 e^{-\Sigma_t x} \quad (4)$$

Where x (in cm) is the thickness of the material, I_0 and I are the unattenuated and attenuated neutrons, and Σ_t (in cm^{-1}) is the total macroscopic cross-section.

2.3. Theoretical basis of gamma-ray shielding

When a gamma-ray beam passes through an absorbing medium, the intensity of the beam will be attenuated according to the Beer-Lambert law, so the linear absorption constant (μ) of the incident beam is calculated as follows;

$$I = I_0 e^{-\mu x} \quad (5)$$

Where x (in cm) is the thickness of the material, I_0 and I are the unattenuated and attenuated gamma-ray beam intensities, and μ (in cm^{-1}) are the linear attenuation coefficients.

Half Value Layer (HVL) is the thickness of a shield or an absorber that reduces the radiation level by a factor of 2 that is to half the initial level and is calculated by the following equation:

$$HVL = \frac{ln2}{\mu} = \frac{0,693}{\mu} \quad (6)$$

Similarly, the Tenth Value Layer (TVL) is defined as the thickness of a shield required for attenuating a radiation beam to 10% of its radiation level and is computed by,

$$TVL = \frac{ln10}{\mu} = \frac{2,3026}{\mu} \quad (7)$$

3. Results and Discussion

The thermal neutron total macroscopic cross-section values of (100-x)%Al-x%Gd_2O_3 (x=5 to 50) and 100(x+y)%Al-x%Gd_2O_3-y%W (x-y=5 to 50) composites are presented in Figure 2. As can be seen, the thermal neutron total macroscopic cross section increases with increasing Gd_2O_3 content in the composite. The thermal neutron total macroscopic cross-section value for the 95%Al-5%Gd_2O_3 composite is the lowest (22.7 cm^{-1}) among the Al-Gd_2O_3 series, while the value for the 50%Al-50%Gd_2O_3 composite is the highest (308.5 cm^{-1}). Compared to the reference Al-B_4C composite in the literature, the thermal neutron total macroscopic cross-section value of 26.68 cm^{-1} for the 70%Al-30%B_4C composite is lower than all Al-Gd_2O_3 composites in the series except the 95%Al-5%Gd_2O_3 composite.

In the Al-Gd_2O_3-W ternary composite, all composites except (95-x)%Al-5%Gd_2O_3-x%W (x=5, 10 and 15) composites have higher thermal neutron total macroscopic cross section values compared to the 70%Al-30%B_4C composite.

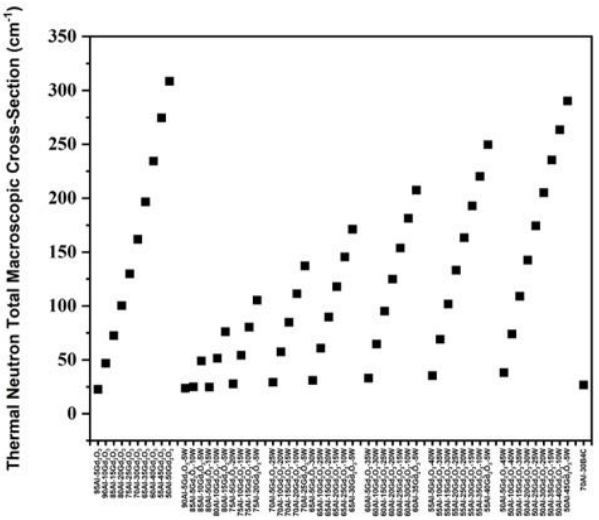

Figure 2. Thermal neutron total macroscopic cross-section of Al-Gd_2O_3/Al-Gd_2O_3-W composite combinations

The gamma-ray LAC, HVL, and TVL values of the (100-x)%Al-x%Gd_2O_3 (x=5 to 50) and 100-(x+y)%Al-x%Gd_2O_3-y%W (x-y=5 to 50) composites are depicted in Figure 3(a-c). As shown in Figure 3(a), the LAC of a composite increases when its Gd_2O_3 ratio increases. Among the Al-Gd_2O_3 series, 95%Al-5%Gd_2O_3 composite has the lowest gamma ray LAC value (0.154 cm^{-1}) and and the composite with the highest LAC value (0.213 cm^{-1}) is 50%Al-50%Gd_2O_3. In the case of the 100-(x+y)%Al-x%Gd_2O_3-y%W (x-y=5 to 50) composite, the LAC of a composite in the series decreases when its Gd_2O_3 ratio increases. The lowest LAC (0.161 cm^{-1}) is for the 90%Al-5%Gd_2O_3-5W composite, while the highest LAC (0.256 cm^{-1}) is for the 50%Al-5%Gd_2O_3-45%W composite. The LAC values of all Al-Gd_2O_3-W composites were calculated to be higher than that of the 70%Al-30%B_4C (0.144 cm^{-1}) composite. The LAC value of lead, accepted as a reference in gamma-ray absorption, was calculated as 0.656 cm^{-1}.

As shown in Figure 3(b-c), the highest HVL (3.19 cm) and TVL (10.6 cm) values were calculated for 50%Al-5%Gd_2O_3-45%W composite. Due to the high LAC value of tungsten, doping tungsten into the composite increases the gamma-ray shielding capability. In the literature, the HVL of lead used for gamma-ray shielding is calculated as 1.06 cm and the TVL as 3.51 cm.

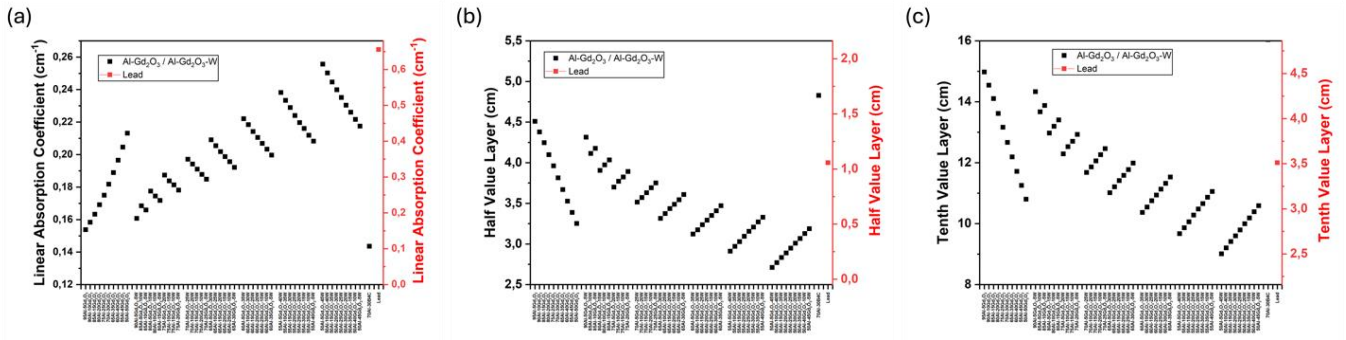

Figure 3. LAC, HVL, and TVL of Al-Gd_2O_3/Al-Gd_2O_3-W composite combinations

4. Conclusions

In this study, thermal neutron total macroscopic cross-section and gamma-ray LAC, HVL and TVL values of composites (100-x)%Al-x%Gd_2O_3 (where x=5 to 50) and 100-(x+y)%Al-x%Gd_2O_3-y%W (x-y=5 to 50) were calculated using the MCNP6.2 simulation code. This study investigated changes in the thermal neutron total macroscopic cross-sections and gamma-ray shielding properties of composites with Al matrix and Gd_2O_3 and W dopants. The results can be summarized as follows: The highest thermal neutron total macroscopic cross-section was calculated for the 50%Al-50%Gd_2O_3 composite. Gd is known to have the highest thermal neutron absorption cross-section. Therefore, doping Gd_2O_3 to the Al matrix significantly increases its thermal neutron total macroscopic cross-section. Similarly, Tungsten, with its high LAC value, increases the gamma-ray shielding properties of the composite when doped into the Al-Gd_2O_3 composite. The highest gamma-ray shielding value was calculated for the 50%Al-%5Gd_2O_3-45%W composite.

The cost of Gd_2O_3 is similar to that of B_4C and less than that of pure Gd. Since Gd has a much higher thermal neutron cross-section than B, adding only 5% Gd_2O_3 to the composite brings the thermal neutron total macroscopic cross-section closer to the value obtained with 30% B_4C doping.

Therefore, Gd_2O_3 is more cost-effective than B_4C. The composite formed with tungsten doping will be shielded in the secondary gamma-ray produced during the neutron absorption reaction.

Author contribution

Yasin GAYLAN: Investigation, Original Draft Writing, Review and Editing,

Ahmet BOZKURT: Review and Editing, Supervision

Conflicts of interest

There are no apparent conflicts.

Acknowledgments

N/A

Ethics Committee Approval and Informed Consent

As the authors of this study, we declare that we do not have any ethics committee approval and/or informed consent statement.

References

[1] E. G. Aydın, E. Tel, A. Kaplan, and A. Aydin, "Equilibrium and pre-equilibrium calculations of neutron production in medium-heavy targets irradiated by protons up to 100 MeV," Annals of Nuclear Energy, 35(12), 2306–2312, 2008.

[2] M. M. Castellanos, A. McAuley, and J. E. Curtis, "Investigating Structure and Dynamics of Proteins in Amorphous Phases Using Neutron Scattering," Computational and Structural Biotechnology Journal, 15, 117–130, 2017.

[3] A. Lombardi, D. Sediako, A. Machin, C. Ravindran, and R. MacKay, "Transient analysis of residual strain during heat treatment of multi-material engine blocks using in-situ neutron diffraction," Materials Letters, 157, 50–52, 2015.

[4] F. Mireles, J. I. Davila, J. L. Pinedo, E. Reyes, R. J. Speakman, and M. D. Glascock, "Assessing urban soil pollution in the cities of Zacatecas and Guadalupe, Mexico by instrumental neutron activation analysis," Microchemical Journal, 103, 158–164, 2012.

[5] T. Örs, F. Gouraud, R. Guinebretière, M. Huger, V. Michel, and O. Castelnau, "Neutron diffraction measurements of residual stress distribution in large zirconia based refractory bricks produced by electro-fusion and casting," Journal of the European Ceramic Society, 37(5), 2295–2302, 2017.

[6] T. Seymour, P. Frankel, L. Balogh, T. Ungár, S. P. Thompson, D. Jädernäs, J. Romero, L. Hallstadius, M. R. Daymond, G. Ribárik, and M. Preuss, "Evolution of dislocation structure in neutron irradiated Zircaloy-2 studied by synchrotron x-ray diffraction peak profile analysis," Acta Materialia, 126, 102–113, 2017.

[7] P. Schofield, B. Geiger, K. Sim, and A. J. Einstein, "ICRP Tahunan," 1–125, 2012.

[8] ICRP, "Annals of the International Commission on Radiological Protection, ICRP Publication 103," Ann. ICRP, 37(3–4), 332, 2007.

[9] R. C. Baumann and E. B. Smith, "Neutron-induced boron fission as a major source of soft errors in deep submicron SRAM devices," 2000 IEEE International Reliability Physics Symposium Proceedings, 152–157, 2000.

[10] S. Normand, B. Mouanda, S. Haan, and M. Louvel, "Discrimination methods between neutron and gamma rays for boron loaded plastic scintillators," Nuclear Instruments and Methods in Physics Research, Section A: Accelerators, Spectrometers, Detectors and Associated Equipment, 484(1–3), 342–350, 2002.

[11] M. Bastürk, J. Arztmann, W. Jerlich, N. Kardjilov, E. Lehmann, and M. Zawisky, "Analysis of neutron attenuation in boron-alloyed stainless steel with neutron radiography and JEN-3 gauge," Journal of Nuclear Materials, 341(2–3), 189–200, 2005.

[12] A. Nishimura, Y. Izumi, M. Imaizumi, S. Nishijima, T. Hemmi, and T. Shikama, "Neutron and gamma ray irradiation effects on interlaminar shear strength of insulation materials with cyanate ester-epoxy blended resin," Fusion Engineering and Design, 86(6–8), 1558–1561, 2011.

[13] Y. Tanabe, E. Yasuda, S. Kimura, T. Iseki, T. Maruyama, and T. Yano, "Neutron irradiation effects on dimension and mechanical properties of carbon fiber/carbon composite," Carbon, 29(7), 905–908, 1991.

[14] R. Lo Frano, G. Pugliese, and G. Forasassi, "Thermal analysis of a spent fuel cask in different transport conditions," Energy, 36(4), 2285–2293, 2011.

[15] F. Tang, X. Wu, S. Ge, J. Ye, H. Zhu, M. Hagiwara, and J. M. Schoenung, "Dry sliding friction and wear properties of B4C particulate-reinforced Al-5083 matrix composites," Wear, 264(7–8), 555–561, 2008.

[16] M. Alizadeh, "Strengthening mechanisms in particulate Al/B4C composites produced by repeated roll bonding process," Journal of Alloys and Compounds, 509(5), 2243–2247, 2011.

[17] M. Khakbiz and F. Akhlaghi, "Synthesis and structural characterization of Al-B4C nano-composite powders by mechanical alloying," Journal of Alloys and Compounds, 479(1–2), 334–341, 2009.

[18] A. Yazdani and E. Salahinejad, "Evolution of reinforcement distribution in Al-B4C composites during accumulative roll bonding," Materials and Design, 32(6), 3137–3142, 2011.

[19] K. Deng, J. Shi, C. Wang, X. Wang, Y. Wu, K. Nie, and K. Wu, "Composites : Part A Microstructure and strengthening mechanism of bimodal size particle reinforced magnesium matrix composite," Composites Part A, 43(8), 1280–1284, 2012.

[20] G. Luo, J. Wu, S. Xiong, Q. Shen, and C. Wu, "Microstructure and mechanical behavior of AA2024 / B 4 C composites with a network reinforcement architecture," Journal of Alloys and Compounds, 701, 554–561, 2017.

[21] I. Topcu, H. O. Gulsoy, N. Kadioglu, and A. N. Gulluoglu, "Processing and mechanical properties of B4C reinforced Al matrix composites," Journal of Alloys and Compounds, 482(1–2), 516–521, 2009.

[22] H. S. Chen, W. X. Wang, Y. L. Li, P. Zhang, H. H. Nie, and Q. C. Wu, "The design, microstructure and tensile properties of B4C particulate reinforced 6061Al neutron absorber composites," Journal of Alloys and Compounds, 632, 23–29, 2015.

[23] P. Zhang, Y. Li, W. Wang, Z. Gao, and B. Wang, "The design, fabrication and properties of B4C/Al neutron absorbers," Journal of Nuclear Materials, 437(1–3), 350–358, 2013.

[24] H. S. Chen, W. X. Wang, Y. L. Li, J. Zhou, H. H. Nie, and Q. C. Wu, "The design, microstructure and mechanical properties of B4C/6061Al neutron absorber composites fabricated by SPS," Materials and Design, 94, 360–367, 2016.

[25] Y. Gaylan, B. Avar, M. Panigrahi, B. Aygün, and A. Karabulut, "Effect of the B4C content on microstructure, microhardness, corrosion, and neutron shielding properties of Al–B4C composites," Ceramics International, 49(3), 5479–5488, 2023.

[26] F. Zhang, X. Wang, J. B. Wierschke, and L. Wang, "Helium bubble evolution in ion irradiated Al/B4C metal metrix composite," Scripta Materialia, 109, 28–33, 2015.

[27] R. G. Abrefah, R. B. M. Sogbadji, E. Ampomah-Amoako, S. A. Birikorang, H. C. Odoi, and B. J. B. Nyarko, "Comparison of the effects of cadmium-shielded and boron carbide-shielded irradiation channel of the Ghana Research Reactor-1," Nuclear Engineering and Design, 241(8), 3017–3020, 2011.

[28] S. Wan, W. Wang, H. Chen, J. Zhou, Y. Zhang, R. Liu, and R. Feng, "155/157Gd areal density: A model for design and fabrication of Gd2O3/316L novel neutron shielding composites," Vacuum, 176, 2020.

[29] R. Florez, H. A. Colorado, C. H. C. Giraldo, and A. Alajo, "Preparation and characterization of Portland cement pastes with Sm2O3 microparticle additions for neutron shielding applications," Construction and Building Materials, 191, 498–506, 2018.

[30] Z. G. Xu, L. T. Jiang, Q. Zhang, J. Qiao, D. Gong, and G. H. Wu, "The design of a novel neutron shielding B4C/Al composite containing Gd," Materials and Design, 111, 375–381, 2016.

[31] L. T. Jiang, Z. G. Xu, Y. K. Fei, Q. Zhang, J. Qiao, and G. H. Wu, "The design of novel neutron shielding (Gd+B4C)/6061Al composites and its properties after hot rolling," Composites Part B: Engineering, 168, 183–194, 2019.

[32] Y. Li, W. Wang, J. Zhou, H. Chen, and P. Zhang, "10B areal density: A novel approach for design and fabrication of B4C/6061Al neutron absorbing materials," Journal of Nuclear Materials, 487, 238–246, 2017.

[33] J. J. Park, S. M. Hong, M. K. Lee, C. K. Rhee, and W. H. Rhee, "Enhancement in the microstructure and neutron shielding efficiency of sandwich type of 6061Al-B4C composite material via hot isostatic pressing," Nuclear Engineering and Design, 282, 1–7, 2015.

[34] P. Zhang, J. Li, W. xian Wang, X. yue Tan, L. Xie, and F. yun Guo, "The design, microstructure and mechanical properties of a novel Gd2O3/6061Al neutron shielding composite," Vacuum, 162(January), 92–100, 2019.

[35] S. Cong, Y. Li, G. Ran, W. Zhou, and Q. Feng, "Microstructure and its effect on mechanical and thermal properties of Al-based Gd2O3 MMCs used as shielding materials in spent fuel storage," Ceramics International, 46(9), 12986–12995, 2020.

[36] K. Karimi-Shahri, L. Rafat-Motavalli, and H. Miri-Hakimabad, "Finding a suitable shield for mixed neutron and photon fields based on an Am-Be source," Journal of Radioanalytical and Nuclear Chemistry, 298(1), 33–39, 2013.

[37] H. Turkez, B. Cakmak, and K. Celik, "Evaluation of the Potential In Vivo Genotoxicity of Tungsten (VI) Oxide Nanopowder for Human Health," Key Engineering Materials, 543, 89–92, 2013.

[38] S. M. Hulbert and K. A. Carlson, "Is lead dust within nuclear medicine departments a hazard to pediatric patients?," Journal of Nuclear Medicine Technology, 37(3), 170–172, 2009.

[39] V. F. Sears, "Neutron News Neutron scattering lengths and cross sections," Neutron News, 1992.

[40] S. Cong, G. Ran, Y. Li, and Y. Chen, "Ball-milling properties and sintering behavior of Al-based Gd2O3–W shielding materials used in spent-fuel storage," Powder Technology, 369, 127–136, 2020.

[41] C. J. Werner, J. S. Bull, C. J. Solomon, F. B. Brown, G. W. McKinney, M. E. Rising, D. A. Dixon, R. L. Martz, H. G. Hughes, L. J. Cox, A. J. Zukaitis, J. C. Armstrong, R. A. Forster, and L. Casswell, "MCNP Version 6.2 Release Notes," 2018.

[42] M. I. Sayyed, K. A. Mahmoud, S. Islam, O. L. Tashlykov, E. Lacomme, and K. M. Kaky, "Application of the MCNP 5 code to simulate the shielding features of concrete samples with different aggregates," Radiation Physics and Chemistry, 174(March), 108925, 2020.

[43] R. El-Mallawany, M. I. Sayyed, M. G. Dong, and Y. S. Rammah, "Simulation of radiation shielding properties of glasses contain PbO," Radiation Physics and Chemistry, 151, 239–252, 2018.

[44] R. B. Malidarre, H. O. Tekin, Gunuglu Kadir, and H. Akyıldırım, "Assessment of Gamma Ray Shielding Properties for Skin," International Journal of Computational and Experimental Science and Engineering, 9(1), 6–10, 2023.

[45] B. Oruncak, "Computation of Neutron Coefficients for B2O3 reinforced Composite," International Journal of Computational and Experimental Science and Engineering, 9(2), 50–53, 2023.

[46] Z. Aygun and M. Aygun, "An Analysis on Radiation Protection Abilities of Different Colored Obsidians," International Journal of Computational and Experimental Science and Engineering, 9(2), 170–176, 2023.

[47] A. Coşkun, B. Cetin, İ. Yiğitoğlu, and H. Topakli, "Comparison of the Radiation Absorption Properties of PbO doped ZrB2 Glasses by using GATE-GEANT4 Monte Carlo Code and XCOM Programme," International Journal of Computational andExperimental Science and ENgineering (IJCESEN), 9(3), 274–279, 2023.

[48] J. E. Martin, *Physics for Radiation Protection, Third Edition* (Wiley-VCH, 2013).

[49] A. T. Boothroyd, *Principles of Neutron Scattering from Condensed Matter* (Oxford University Press, 2020).